

# Simulation and Scaling of the Turbulent Vertical Heat Transport and Deep-Cycle Turbulence across the Equatorial Pacific Cold Tongue

D. B. WHITT,<sup>a,b</sup> D. A. CHERIAN,<sup>b</sup> R. M. HOLMES,<sup>c,d,e,f</sup> S. D. BACHMAN,<sup>b</sup> R.-C. LIEN,<sup>g</sup> W. G. LARGE,<sup>b</sup> AND J. N. MOUM<sup>h</sup>

<sup>a</sup> NASA Ames Research Center, Moffett Field, California

<sup>b</sup> National Center for Atmospheric Research, Boulder, Colorado

<sup>c</sup> School of Geosciences, University of Sydney, Sydney, New South Wales, Australia

<sup>d</sup> Climate Change Research Centre, University of New South Wales, Sydney, New South Wales, Australia

<sup>e</sup> School of Mathematics and Statistics, University of New South Wales, Sydney, New South Wales, Australia

<sup>f</sup> ARC Centre of Excellence for Climate Extremes, University of New South Wales, Sydney, New South Wales, Australia

<sup>g</sup> Applied Physics Laboratory, University of Washington, Seattle, Washington

<sup>h</sup> College of Earth, Ocean, and Atmospheric Sciences, Oregon State University, Corvallis, Oregon

(Manuscript received 16 July 2021, in final form 4 February 2022)

**ABSTRACT:** Microstructure observations in the Pacific cold tongue reveal that turbulence often penetrates into the thermocline, producing hundreds of watts per square meter of downward heat transport during nighttime and early morning. However, virtually all observations of this deep-cycle turbulence (DCT) are from 0°, 140°W. Here, a hierarchy of ocean process simulations, including submesoscale-permitting regional models and turbulence-permitting large-eddy simulations (LES) embedded in a regional model, provide insight into mixing and DCT at and beyond 0°, 140°W. A regional hindcast quantifies the spatiotemporal variability of subsurface turbulent heat fluxes throughout the cold tongue from 1999 to 2016. Mean subsurface turbulent fluxes are strongest (~100 W m<sup>-2</sup>) within 2° of the equator, slightly (~10 W m<sup>-2</sup>) stronger in the northern than Southern Hemisphere throughout the cold tongue, and correlated with surface heat fluxes ( $r^2 = 0.7$ ). The seasonal cycle of the subsurface heat flux, which does not covary with the surface heat flux, ranges from 150 W m<sup>-2</sup> near the equator to 30 and 10 W m<sup>-2</sup> at 4°N and 4°S, respectively. Aseasonal variability of the subsurface heat flux is logarithmically distributed, covaries spatially with the time-mean flux, and is highlighted in 34-day LES of boreal autumn at 0° and 3°N, 140°W. Intense DCT occurs frequently above the undercurrent at 0° and intermittently at 3°N. Daily mean heat fluxes scale with the bulk vertical shear and the wind stress, which together explain ~90% of the daily variance across both LES. Observational validation of the scaling at 0°, 140°W is encouraging, but observations beyond 0°, 140°W are needed to facilitate refinement of mixing parameterization in ocean models.

**SIGNIFICANCE STATEMENT:** This work is a fundamental contribution to a broad community effort to improve global long-range weather and climate forecast models used for seasonal to longer-term prediction. Much of the predictability on seasonal time scales is derived from the slow evolution of the upper eastern equatorial Pacific Ocean as it varies between El Niño and La Niña conditions. This study presents state-of-the-art high-resolution regional numerical simulations of ocean turbulence and mixing in the eastern equatorial Pacific. The results inform future planning for field work as well as future efforts to refine the representation of ocean mixing in global forecast models.

**KEYWORDS:** Turbulence; Mixing; Oceanic mixed layer; Large eddy simulations; Parameterization

## 1. Introduction

Over the last several decades, multiple field campaigns have observed strong turbulence above the equatorial undercurrent in the eastern Pacific Ocean (Gregg et al. 1985; Moum and Caldwell 1985; Peters et al. 1988; Lien et al. 1995; Moum et al. 2009, 2013; Warner and Moum 2019; Smyth et al. 2021). Like upper-ocean turbulence elsewhere in the tropics and subtropics, the diurnal cycle is a dominant mode of variability, but turbulence in the eastern equatorial Pacific is unusual in that it penetrates tens of meters below the base of the surface mixed layer and into the thermocline. This turbulence produces exceptionally strong heat fluxes of  $O(100)$  W m<sup>-2</sup> on average and up to

1000 W m<sup>-2</sup> during occasional bursts of intense turbulence in the nighttime and early morning in a stratified layer tens of meters thick (Moum et al. 2013, 2009; Smyth et al. 2021). Hence, this “deep-cycle turbulence” (DCT) drives stronger cooling of the near surface and warming of the thermocline compared to diurnal surface boundary layer turbulence in other areas of the global oceans. DCT thus contributes to sustaining the relatively cool sea surface and net ocean heat uptake in the eastern equatorial Pacific Ocean cold tongue on average (Wang and McPhaden 1999; Moum et al. 2013). DCT also varies with and influences the regional sea surface temperature (SST) dynamics on multiple time scales beyond diurnal, including interannual (Warner and Moum 2019), seasonal (Wang and McPhaden 1999; Moum et al. 2013), and subseasonal (Lien et al. 2008; Moum et al. 2009), although these variations are not as well understood as the diurnal cycle.

Corresponding author: D. B. Whitt, daniel.b.whitt@nasa.gov

DOI: 10.1175/JPO-D-21-0153.1

© 2022 American Meteorological Society. For information regarding reuse of this content and general copyright information, consult the AMS Copyright Policy ([www.ametsoc.org/PUBSReuseLicenses](http://www.ametsoc.org/PUBSReuseLicenses)).

If the available data from  $0^\circ$ ,  $140^\circ\text{W}$  are representative, then turbulent mixing is an important participant in the SST budget and air–sea interaction in the Pacific Ocean cold tongue. However, neither the spatiotemporal variability of ocean mixing nor the physical drivers of variability on time scales beyond diurnal are well observed or understood. In particular, our knowledge of the area and vertical extent of strong turbulent heat fluxes is based almost entirely on extrapolation using parameterizations beyond  $0^\circ$ ,  $140^\circ\text{W}$  (e.g., Pacanowski and Philander 1981; Holmes and Thomas 2015; Holmes et al. 2019a; Pei et al. 2020; Deppenmeier et al. 2021; Cherian et al. 2021). In addition, none of these parameterized modeling studies present results over a sufficient duration to provide a climatological perspective from a model with sufficiently fine horizontal grid spacing [ $<10$  km horizontal (Marchesiello et al. 2011), and  $<5$  m vertical (Jia et al. 2021)] to fully resolve the mesoscale variations in vertical shear, which significantly modulate mixing (Moum et al. 2009; Inoue et al. 2012; Holmes and Thomas 2015; Cherian et al. 2021). Hence, the broader implications of downward turbulent heat transport and specifically DCT in the cold tongue for global ocean, climate, and Earth system dynamics are not well understood (but see Meehl et al. 2001; Richards et al. 2009; Danabasoglu et al. 2006; Newsom and Thompson 2018; Holmes et al. 2019a,b; Zhu and Zhang 2019; Huguenin et al. 2020; Deppenmeier et al. 2021). In addition, climate models suffer from long-standing and significant biases in their simulation of the SST, thermocline, and circulation in the eastern equatorial Pacific (Li and Xie 2014; Li et al. 2015). Since some biases persist with refinements in model horizontal grid resolution and the mean ocean circulation (Small et al. 2014) and are sensitive to the formulation of the mixing scheme (Meehl et al. 2001; Richards et al. 2009; Zhu and Zhang 2019), it seems plausible if not likely that poor performance of parameterizations of ocean mixing physics (Zaron and Moum 2009) is at least partially responsible for equatorial Pacific biases in climate and Earth system models. Hence, we conducted a regional process modeling study of turbulent heat transport and DCT in the equatorial Pacific Ocean cold tongue as a contribution to a broader effort to conduct a prefield process modeling study of Pacific equatorial upwelling and mixing physics.

In this manuscript, we present new state-of-the-art simulations and new metrics to characterize turbulent vertical heat transport in the Pacific Ocean cold tongue. First, we examine the climatological (1999–2016) spatiotemporal variability of the turbulent vertical heat flux, including the time-mean, seasonal cycle, and aseasonal variability (i.e., all deviations from the mean seasonal cycle) of the daily mean flux, in a relatively fine ( $1/20^\circ$  horizontal, 2.5 m vertical) resolution regional hindcast simulation of the eastern equatorial Pacific Ocean with parameterized vertical mixing. The results provide a climatological perspective on the recent finding that global ocean models can simulate DCT (Pei et al. 2020), as well as the finding of and explanation for DCT off the equator in a regional ocean model (Cherian et al. 2021), and complement other climatological studies of mixing in the equatorial Pacific cold tongue focused on different questions, different metrics, and different models with coarser resolution (e.g., Ray et al. 2018; Holmes et al. 2019a; Huguenin et al. 2020; Deppenmeier et al. 2021). The analysis of the regional model also shows that the

daily mean turbulent heat transport is logarithmically distributed, thus relatively rare events associated with aseasonal variability on time scales of days to weeks have a strong influence on and spatially covary with the time-mean transport.

We build understanding of the subseasonal part of aseasonal variability in mixing via large-eddy simulations (LES) that are embedded in a regional ocean model so that the simulated turbulence varies in the context of realistic variations in horizontal currents and temperature and atmospheric forcing over time scales from hours to more than a month. These LES address a key source of uncertainty in our regional model and all prior studies of ocean mixing on time scales from weeks to months using models: our regional models and all prior models are based on uncertain mixing parameterizations. Here, the LES are used to study the variability of explicit (rather than parameterized) turbulent mixing and DCT on time scales from days to a month for the first time. Our LES build on prior shorter simulations of diurnal cycles and shorter variability with idealized boundary conditions and forcing (Skylingstad and Denbo 1994; Wang et al. 1996, 1998; Large and Gent 1999; Wang and Müller 2002; Pham et al. 2013) as well as how the diurnal cycles vary between the four seasons at  $0^\circ$ ,  $140^\circ\text{W}$  (Pham et al. 2017; Sarkar and Pham 2019). Through both the analysis of the regional model and the LES, we confront the simulations of turbulence with observations and critically evaluate the model representations, albeit only at  $0^\circ$ ,  $140^\circ\text{W}$ . Future observations are needed to evaluate and constrain modeled turbulence beyond  $0^\circ$ ,  $140^\circ\text{W}$  in the Pacific cold tongue.

## 2. Methods

### *a. Ocean hindcast of the eastern equatorial Pacific, 1999–2016*

Climatological statistics of vertical mixing throughout the equatorial Pacific cold tongue are derived from an ocean hindcast of the period 1999 through 2016 in the region from  $170^\circ$  to  $95^\circ\text{W}$  and from  $12^\circ\text{S}$  to  $12^\circ\text{N}$  in a submesoscale-permitting  $1/20^\circ$  configuration (Cherian et al. 2021) of the MITgcm (Adcroft et al. 2004; Marshall et al. 1997). As described previously (Cherian et al. 2021), the model is forced at the surface by fluxes derived from bulk flux algorithms and the JRA-55 based surface dataset for driving ocean–sea ice models (JRA55-do) atmospheric reanalysis (Tsujino et al. 2018) and at side boundaries by daily mean horizontal velocity, temperature and salinity from the Mercator Global Ocean reanalysis and Simulation (GLORYS)  $1/12^\circ$  ocean reanalysis. Solar radiation penetrates and warms the water below the surface, and there are no tides. Vertical mixing is represented by the  $K$ -profile parameterization (KPP) (Large et al. 1994), which was compared against and tuned to match LES of partially resolved DCT at  $0^\circ$ ,  $140^\circ\text{W}$  (Large and Gent 1999). This hindcast is very similar to that of Cherian et al. (2021), where some observational validations are presented. The main technical difference between the two hindcasts, in addition to the different and longer simulated time interval, is that the model grid has a slightly coarser vertical resolution (2.5 m versus 1 m

TABLE 1. A glossary table with definitions and sections where key metrics are defined.

Metric	Definition (key defining sections)
$Q_0^{\text{net}}$	Net surface heat flux (section 3a)
$\langle F_Q \rangle^{\text{max}}$	Maximum (over depth) of the daily mean downward turbulent heat flux (sections 3a, 4a)
$F_b$	Downward turbulent buoyancy flux; roughly proportional to $F_Q$ (sections 4a, 4c, appendix)
$\mathbf{F}_m$	Downward turbulent momentum flux (section 4b, appendix)
$\epsilon$	Dissipation rate of turbulent kinetic energy (section 4b, appendix)
SP	Shear production of turbulent kinetic energy $\mathbf{F}_m \cdot \partial \mathbf{u}_h / \partial z$ (section 4d, appendix)
$T$	Convergence of the vertical transport of turbulent kinetic energy (section 4d, appendix)
$z_{\text{max}}$	Depth at which the maximum $\langle F_Q \rangle^{\text{max}}$ or $\langle F_b \rangle^{\text{max}}$ occurs (sections 3a, 4c)
$z_{\text{pen}}$	Depth to which DCT penetrates; shallowest depth $\epsilon \leq 2 \times 10^{-8} \text{ m}^2 \text{ s}^{-3}$ (section 4c)
MLD	Mixed layer depth, first depth 0.015 $\text{kg m}^{-3}$ denser than 0–10-m mean (sections 3a, 4c)
$H_{\text{Rib}}$	Thickness of the surface layer with bulk $\text{Ri}_b = 0.2$ (section 4c)
$\text{Ri}_b$	Bulk Richardson number of a surface layer (section 4c)
$H_{\text{Rig}}$	Thickness of the low $\text{Ri}_g$ layer, $\text{Ri}_g < 0.35$ (section 4c)
$\text{Ri}_g$	Gradient Richardson number, $\text{Ri}_g = \partial b / \partial z /  \partial \mathbf{u}_h / \partial z ^2 = N^2 / S^2$ (section 2c)
$\text{Ri}_f$	Flux Richardson number, $\text{Ri}_f = F_b / \text{SP}$ (section 4d)
$\text{Pr}_t$	Turbulent Prandtl number, $\text{Pr}_t = \text{Ri}_g / \text{Ri}_f$ (section 4d)
$S_b$	Bulk vertical shear from least squares fit to the horizontal velocity from $H_{\text{Rig}}$ to 5-m depth (sections 4e, 4f)

over the top 250 m), because the reduced vertical resolution had a negligible impact on the solutions in short tests and reduced the computational cost. The analysis is conducted on the saved daily mean temperature, salinity, and heat budget diagnostics. See Table 1 for a list of several of the most commonly used metrics to quantify and describe vertical mixing as well as the sections in which they are defined and discussed.

### b. Large-eddy simulation hindcasts of turbulence over 34 days

To better understand and validate the subseasonal spatiotemporal variability in turbulent mixing on and off the equator, we report results from two 34-day LES that are hindcasts of upper-ocean turbulence in a small  $306 \text{ m} \times 306 \text{ m} \times 108 \text{ m}$  deep domain during the period from 2 October to 5 November 1985 at  $0^\circ$  and  $3^\circ\text{N}$  along  $140^\circ\text{W}$  in the equatorial Pacific cold tongue. Unlike the regional ocean hindcast and most other ocean models, the LES explicitly simulates rather than parameterizes the outer scales  $O(1) \text{ m}$  of the turbulence and thus can provide insight into the physics of ocean mixing and DCT. However, the LES has a computational cost that is many orders of magnitude greater than the regional ocean model per unit simulated time and volume, hence the LES must be run for much shorter time intervals and in much smaller domains (Skylingstad and Denbo 1994; Wang et al. 1996, 1998; Wang and Müller 2002; Pham et al. 2013, 2017; Sarkar and Pham 2019). A detailed description of the LES model is given in the appendix. In short, the LES is forced by variable 6-hourly air–sea fluxes (including a diurnal cycle of penetrating shortwave radiation) and larger-scale ( $\geq 15 \text{ km}$ ) oceanic tendencies, such as advection and the pressure gradient force, derived from a regional ocean hindcast simulation of the entire Pacific cold tongue. The LES forcing is from the parent ocean model ROMS, not MITgcm, because ROMS solutions (based on earlier work of Holmes and Thomas 2015) were available earlier with all the necessary outputs. However, the domain, the horizontal resolution  $1/20^\circ$ , the

vertical mixing scheme KPP, the 3-hourly surface forcing (including diurnal cycle of penetrating solar radiation) from JRA55-do are all the same in ROMS and MITgcm, and the mesoscale fields and parameterized mixing dynamics of interest are qualitatively similar [see the appendix for details and compare the results reported in Holmes and Thomas (2015) and Cherian et al. (2021)].

The inclusion of larger-scale oceanic tendencies of temperature and momentum from ROMS are an important novelty in these LES and crucial for sustaining realistic temperature and horizontal velocity profiles over time scales longer than a few days (Qiao and Weisberg 1997). These tendencies also provide a source of subseasonal variability on time scales from days to a month (Holmes and Thomas 2015; Cherian et al. 2021). Hence, an important point of reference is the one previous LES study of the eastern equatorial Pacific that incorporated large-scale tendencies (Wang et al. 1998). In addition to finer grid resolution, comparisons with an off-equatorial domain, and longer (34 versus 6 days) simulations than in Wang et al. (1998), the ocean tendencies used here also differ from those in Wang et al. (1998) in that they are derived from a realistic regional ocean model rather than idealized mathematical formulas. Thus, the large-scale oceanic conditions and related large-scale tendencies (as well as the air–sea fluxes) evolve on time scales from 6 h to 1 month during the simulations, in conjunction with the passage of a tropical instability wave and other mesoscale ocean variability. In addition, there is approximate dynamical consistency between the initial conditions, surface fluxes and interior tendencies, as well as between the LES at  $0^\circ$  and  $3^\circ\text{N}$  across this range of time scales. Hence, despite some broken feedbacks between the limited LES domain and the larger-scale ocean and atmosphere, the differences between the LES and the ocean model mean profiles of temperature and zonal momentum are always less than  $0.5^\circ\text{C}$  and  $0.25 \text{ m s}^{-1}$ . That is, the turbulence simulated by LES, the surface fluxes, and the interior tendencies remain approximately consistent as if the LES was part of

a two-way coupled regional system rather than an isolated domain throughout the 34-day simulations.

LES outputs include instantaneous statistics, such as the horizontally averaged turbulent vertical fluxes of heat and momentum among others, which are saved irregularly about every 2–5 simulated minutes and additionally binned into daily mean statistics for some analyses (to obtain the data and source code, see data availability statement). Note that all times are in UTC, and the local solar time is about 9 h behind UTC, so solar noon occurs at about 2100 UTC. All daily mean LES statistics, such as daily mean flux profiles, are calculated from 2100 UTC so that the 34 daily means begin and end at about solar noon, beginning on 2100 UTC 2 October 1985 and ending at 2100 UTC 5 November 1985.

### c. Evaluation of the LES zonal velocity and temperature by comparison with observations

Comparisons with observations suggest that the LES yield plausibly realistic zonal velocity and temperature simulations with a few exceptions. Mean vertical profiles of temperature and zonal velocity are generally within observed ranges at 0°, 140°W where mooring observations from the Tropical Atmosphere Ocean (TAO) array (McPhaden et al. 2010) are available (Figs. 1 and 2). At 0°, 140°W, there is a clear depth range between about 10 and 75 m where the gradient Richardson number of the horizontally averaged profile, that is the vertical gradient of buoyancy over the squared vertical gradient of horizontal velocity

$$Ri_g = \frac{N^2}{S^2} = \frac{\partial b / \partial z}{|\partial \mathbf{u}_h / \partial z|^2} \approx 1/4, \quad (1)$$

is in a state of marginal instability as observed by Smyth and Moum (2013) (see Fig. 3). The LES results are presented at 3°N for comparison in Figs. 1–3, although mooring observations are not available at 3°N for validation. The observed annual mean climatology of zonal currents and temperature (Johnson et al. 2002) is plotted for comparison with the LES at 3°N, 140°W, but the observed annual climatology is insufficient to validate October mean profiles in the LES at 3°N because there is significant seasonal, interannual, and subseasonal variability. Perhaps the most notable difference between the two latitudes is that the shear is weaker on average at 3°N than at 0°, and  $Ri_g > 1/4$  most of the time at 3°N. Hence, marginal instability  $Ri_g \approx 0.25$  is intermittent (about 25% of the time) from 20- to 70-m depth at 3°N rather than persistent as at 0°.

The diurnal cycle in temperature and zonal velocity is plausible but on the weaker side of the observed diurnal cycles at 0°, 140°W, for example, as shown at 25 m in Fig. 2. Consistent with observations, the modeled diurnal cycle is stronger at shallower depths (e.g., shallower than 15 m), weak but with a notable peak in the frequency spectra at intermediate depths (e.g., between 15 and 45 m), and difficult to discern from other nearby frequencies in the spectra at deeper depths (not shown). A detailed investigation of the mechanisms controlling the amplitude of the diurnal cycle of the horizontally averaged current and temperature profiles (and all other

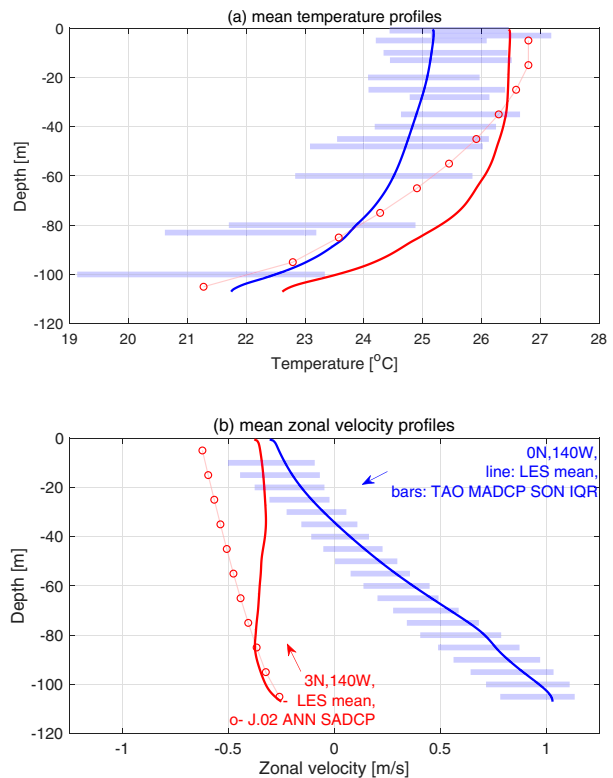


FIG. 1. A comparison between the simulated (LES; solid lines) and (a) observed mean temperature and (b) zonal velocity profiles at 0° (blue) and 3°N (red) along 140°W. At 0°, 140°W, the observations (horizontal bars) span the interquartile ranges of all monthly means (September–November only) from the TAO mooring (1988–2018). At 3°N, 140°W, a ship-based annual climatology is plotted (Johnson et al. 2002), but these are more for reference than for validation since there is significant seasonal and interannual variability.

variables) is left for future work (for prior studies of the diurnal cycle and DCT at 0°, 140°W in LES, see, e.g., Wang et al. 1998; Pham et al. 2013, 2017). This study instead focuses on variability in daily averaged quantities.

The simulated temperature and velocity variance at time scales from days to weeks is generally realistic at 0°, 140°W. For example, the power spectra of temperature and zonal velocity at 25-m depth (Fig. 2) show that variance at periods from a few days to a month is reasonably realistic, but variability at internal wave time scales ranging from a few days to a few hours is consistently weak in the LES relative to the TAO mooring observations (as shown at 25 m). The weakness of internal wave activity at these frequencies is expected (qualitatively) in the LES since the parent ROMS model does not have tides or grid resolution at horizontal scales from 5.5 to 0.3 km (and only 8-m vertical resolution in the upper ocean), where much internal wave activity occurs and from which it cascades down to smaller scales (Gregg et al. 2003). That is, the embedded LES represents only a limited subset of interactions between internal waves, shear instabilities, and

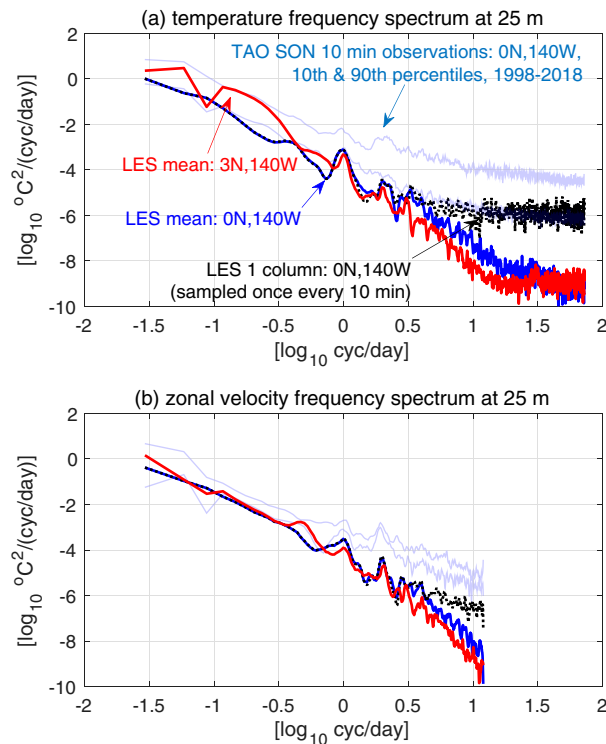


FIG. 2. Simulated (LES) and observed frequency spectra of (a) temperature and (b) zonal velocity at 25-m depth at  $0^\circ$  (blue) and  $3^\circ\text{N}$  (red) along  $140^\circ\text{W}$ . Observed spectra are calculated from the moored temperature sensor (10 min instantaneous sampling) and current meter (1-h average sampling) from the months September–November on the TAO mooring at  $0^\circ$ ,  $140^\circ\text{W}$  for comparison (1988–2018). The observed spectra are calculated in overlapping time windows that are the same length as the LES simulations (with 17% of points overlapped in each window). The 10% and 90% quantile at each frequency (across all of the spectra windows) is plotted in light blue. The black dotted and blue lines are derived from LES: the sampling is instantaneous (averaged over a single time step) every 10 min in (a) or every 1 h in (b) and averaged spatially over a single grid cell/virtual mooring (black dotted) or the entire horizontal extent of the domain (blue). The spectrum from the virtual mooring (black) flattens similarly to the observations from the TAO mooring at frequencies higher than 3 cycles per day due to aliasing in (a).

turbulence. First, the LES represents the response of small-scale shear instabilities, internal waves, and turbulence at horizontal wavelengths smaller than 300 m to large-scale internal waves (among other processes) at horizontal wavelengths  $\geq 15\text{ km}$  that are resolved by the parent model. Second, the LES represents some interactions between internal waves, shear instabilities, and turbulence at scales from about 1 to 300 m that are generated locally in the domain. In particular, the periodic horizontal boundary conditions allow internal waves to persist in the model domain and propagate vertically through the stratification. However, going beyond the comparison between the simulated (black dotted) and observed (light blue) temperature spectra in Fig. 2a to a detailed

investigation of the internal waves and instabilities in the LES and observations (Lien et al. 1996; Smyth et al. 2011; Moum et al. 2011) is left for future work (for some analysis of these topics in other LES, see Pham et al. 2013, 2017).

Finally, the turbulence simulated by the LES is difficult to validate directly since direct observations of the turbulence are so limited in space and time. That said, the simulated turbulence is qualitatively and quantitatively similar to the turbulence observed by Lien et al. (1995) from 4 November to 12 December 1991 (as discussed in more detail below). And, previous studies in simpler model configurations show that the model simulates idealized test cases and turbulent flows with statistics that are consistent with basic conservation constraints (Watkins and Whitt 2020).

### 3. Spatial patterns, seasonal cycle, and aseasonal variability in the regional hindcast

Our analysis of the regional ocean model begins with the definition of the metrics to be used throughout the results (section 3a), then provides a description of the climatological time-mean spatial patterns (section 3b), seasonal cycles (section 3c), and aseasonal variability (section 3d) of ocean mixing in the model as well as comparisons to observations at  $0^\circ$ ,  $140^\circ\text{W}$ .

#### a. Metrics of ocean mixing

We quantify and compare the downward heat flux due to ocean mixing  $F_Q(z)$ , which tends to cool the upper ocean on average, with the net downward surface heat flux  $Q_0^{\text{net}} = F_Q(z=0) + P_Q(z=0)$  (including turbulent fluxes  $F$  and penetrative fluxes  $P$  due to solar radiation), which tends to warm the upper ocean on average (Fig. 4). With regard to ocean mixing, we focus on the maximum over depth  $z$  of the daily mean downward turbulent heat flux  $\langle F_Q \rangle^{\text{max}} = \max_z \langle F_Q(z) \rangle$ , where  $\langle \rangle$  denotes a daily mean (and a horizontal average is implicit, over a single grid cell in the MITgcm and the entire domain in LES). Since the depth  $z_{\text{max}}$  at which  $\langle F_Q \rangle^{\text{max}}$  occurs varies in time and space, we also quantify  $z_{\text{max}}$  and compare it with the mixed layer depth (MLD, defined by the first depth  $0.015 \text{ kg m}^{-3}$  denser than the top 10 m) for reference (Fig. 5).

The maximum daily mean turbulent heat flux  $\langle F_Q \rangle^{\text{max}}$ , the daily net surface heat flux  $\langle Q_0^{\text{net}} \rangle$ , and their difference  $\langle Q_0^{\text{net}} \rangle - \langle F_Q \rangle^{\text{max}}$  provide useful measures of the significance of ocean mixing relative to the net surface heat flux in the upper-ocean heat and SST dynamics throughout the cold tongue. This is a simplified view because other terms also contribute to the heat budget above  $\langle F_Q \rangle^{\text{max}}$  in addition to  $\langle F_Q \rangle^{\text{max}}$  and  $\langle Q_0^{\text{net}} \rangle$ , including penetration of radiative heat fluxes  $\langle P_Q \rangle^{\text{max}}$  below the depth  $z_{\text{max}}$  and advection (e.g., Moum et al. 2013). In addition, the precise role of ocean mixing in the heat budget depends on the depth to which the budget is integrated. Vertical mixing is generally significant if the heat budget is integrated vertically over a layer that is closely correlated with SST (Ray et al. 2018). Having stated the caveats, there are two main reasons we focus on  $\langle F_Q \rangle^{\text{max}}$ . First, it is intrinsically interesting because it essentially quantifies and bounds the maximum impact that mixing could have on the upper-ocean heat budget. Second, we aim to use  $\langle F_Q \rangle^{\text{max}}$  to

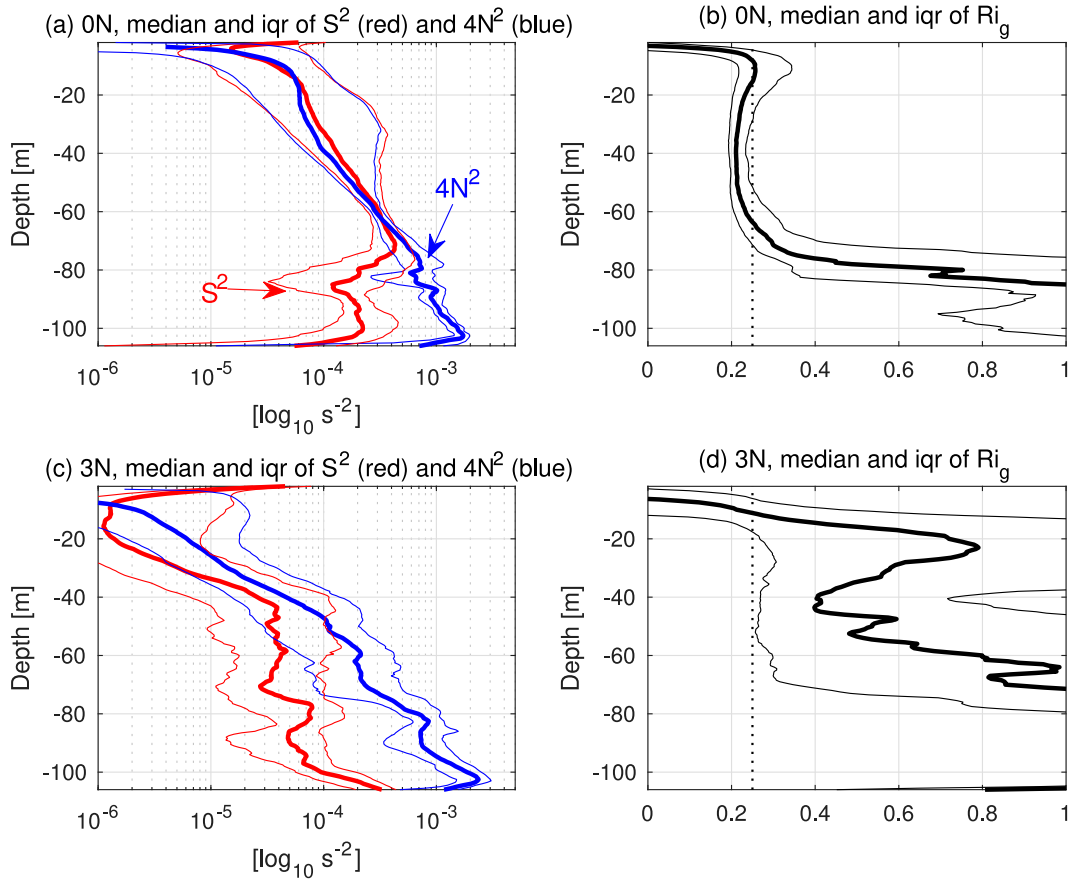


FIG. 3. Profiles of the median (thick lines) and interquartile range (iqr; thin lines) of the squared vertical shear of horizontal velocity  $S^2$ , the vertical buoyancy gradient  $N^2$ , and the gradient Richardson number  $Ri_g = N^2/S^2$  (all of the horizontally averaged profiles). Shown are (a),(b) results from the LES at  $0^\circ\text{N}$  and (c),(d) results from the LES at  $3^\circ\text{N}$ . The dotted vertical line in (b) and (d) indicates  $Ri_g = 0.25$  for reference.

model the whole vertical profile  $\langle F_Q \rangle(z)$  in the upper ocean (see section 4g). The a priori motivation to focus on  $\langle F_Q \rangle^{\max}$  in modeling  $\langle F_Q \rangle(z)$  is based on a hypothesis that  $\langle F_Q \rangle(z)$  can be approximately reconstructed as an interpolation of three points: the surface flux  $\langle F_Q \rangle(z = 0)$ , a positive subsurface  $\langle F_Q \rangle^{\max}$  if it exists, and a point of nearly zero flux at some depth deeper than  $z_{\max}$ . In this manuscript, we quantify and parameterize  $\langle F_Q \rangle^{\max}$  and then demonstrate that  $\langle F_Q \rangle^{\max}$  can be used to predict  $\langle F_Q \rangle(z)$ , leaving an exposition of the relationships between  $\langle F_Q \rangle^{\max}$  and the upper-ocean heat budget formalism to future work (but see Ray et al. 2018).

Although DCT is characterized by strong  $\langle F_Q \rangle^{\max}$  and may contribute significantly to the climatological  $\langle F_Q \rangle^{\max}$ , we choose not to distinguish DCT from other causes of  $\langle F_Q \rangle^{\max}$  via a formal quantitative metric in this manuscript. This is because we want to characterize  $\langle F_Q \rangle^{\max}$  across the cold tongue without assumption about the driving mechanisms, and DCT is not ubiquitous across the cold tongue (Cherian et al. 2021). In addition, even though DCT tends to be associated with strong  $\langle F_Q \rangle^{\max}$ , it is not known if strong  $\langle F_Q \rangle^{\max}$  is always indicative of DCT or why and to what degree  $\langle F_Q \rangle^{\max}$  varies from day to day in DCT or otherwise. However, we

refer to the turbulence driving the mixing descriptively as DCT where and when we feel the subjective criteria (based on prior studies) are met. In particular, prior studies have identified DCT as strong diurnally modulated turbulence in a marginally unstable stratified shear layer ( $Ri_g \approx 1/4$ ) just below the deepest nighttime MLD [for a recent review, see Cherian et al. (2021)].

#### b. Time-mean spatial patterns

We begin by characterizing the time-mean  $\langle F_Q \rangle^{\max}$ , which contributes to sustaining relatively cool time-mean SSTs and net ocean heat uptake  $\langle Q_0^{\text{net}} \rangle$  in the cold tongue by transporting heat downward from the mixed layer to the thermocline (Ray et al. 2018; Holmes et al. 2019a). Consistent with that interpretation, the comparisons between  $\langle Q_0^{\text{net}} \rangle$  and  $\langle F_Q \rangle^{\max}$  demonstrate that the time-mean surface flux and ocean mixing have similar spatial patterns ( $r^2 = 0.7$ ; Figs. 4e,f). Both  $\langle Q_0^{\text{net}} \rangle$  and  $\langle F_Q \rangle^{\max}$  are broadly elevated throughout the cold tongue relative to other areas and take similar area-average values between  $6^\circ\text{S}$  and  $6^\circ\text{N}$  from  $95^\circ$  to  $170^\circ\text{W}$  ( $77 \text{ W m}^{-2}$  for  $\langle F_Q \rangle^{\max}$  and  $59 \text{ W m}^{-2}$  for  $\langle Q_0^{\text{net}} \rangle$ ). In addition, both  $\langle Q_0^{\text{net}} \rangle$  and  $\langle F_Q \rangle^{\max}$  are enhanced by more than a factor of 2 near the

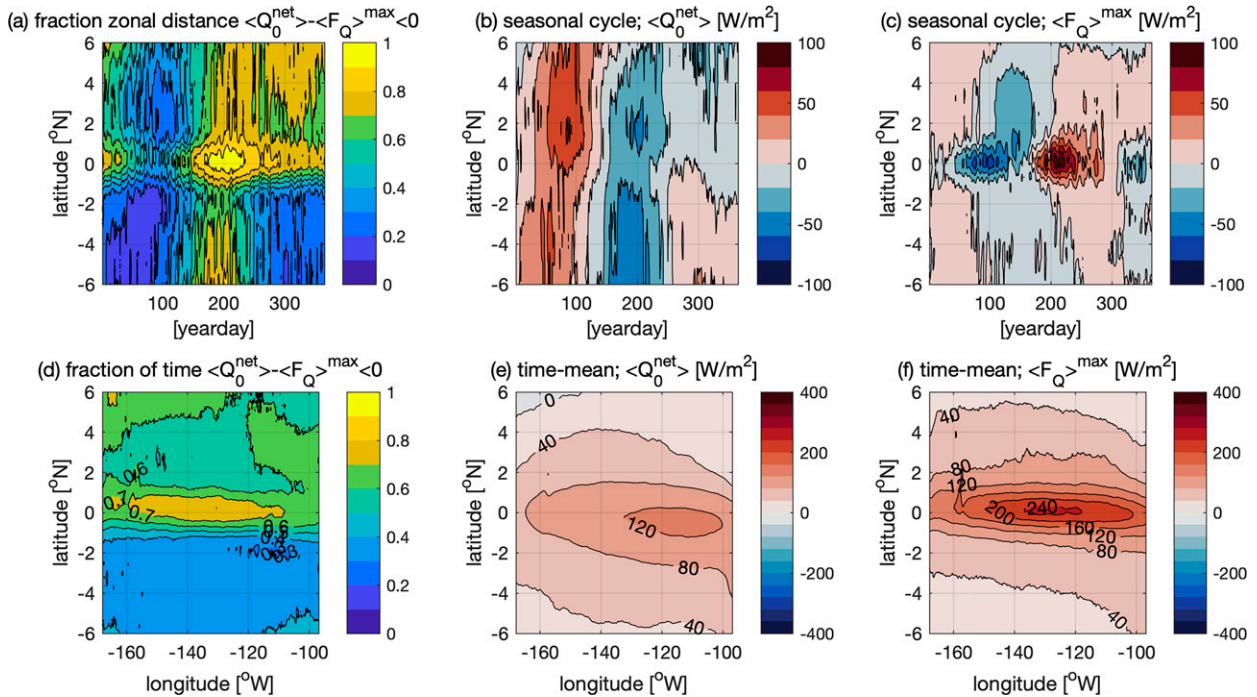


FIG. 4. (a)–(f) Climatological spatial structure and seasonal cycle of downward heat fluxes in a regional ocean model of the equatorial Pacific Ocean cold tongue forced by atmospheric reanalysis from 1999 to 2016. The net air–sea flux  $\langle Q_0^{\text{net}} \rangle$  is in (b) and (e), and the maximum flux due to ocean mixing  $\langle F_Q \rangle^{\text{max}}$  is in (c) and (f). Panels (b) and (c) are the zonal means from 95° to 170°W with the time-mean subtracted, and (e) and (f) are the time-means. In addition, we quantify the fraction of the zonal distance (a) and time (d) over which there is net cooling of the surface ocean due to air–sea exchange and ocean mixing, that is,  $\langle Q_0^{\text{net}} \rangle - \langle F_Q \rangle^{\text{max}} < 0$ . The flux due to ocean mixing  $\langle F_Q \rangle^{\text{max}}$  in (c) and (f) is defined as the maximum (over depth) of the daily mean downward turbulent heat flux, so the zonal and time means are calculated at a depth that varies in time and space that is plotted in Fig. 5.

equator (e.g., between  $\pm 2^\circ$ ) compared to the area means between 6°S and 6°N [Figs. 4e,f; see also Fig. 2 of Cherian et al. (2021) for snapshot plan views].

Closer inspection highlights several important differences in the climatological spatial structure of  $\langle F_Q \rangle^{\text{max}}$  and  $\langle Q_0^{\text{net}} \rangle$ . First,  $\langle F_Q \rangle^{\text{max}}$  is significantly stronger than  $\langle Q_0^{\text{net}} \rangle$  on average in an equatorial mixing band about  $2^\circ$  wide and centered slightly north of the equator that extends zonally through the entire domain (170°–95°W; see Fig. 4d). In this equatorial mixing band, the annual mean surface heat flux  $\langle Q_0^{\text{net}} \rangle$  reaches a peak at just over  $120 \text{ W m}^{-2}$  at about 110°W and just south of the equator, whereas the downward heat flux due to ocean mixing  $\langle F_Q \rangle^{\text{max}}$  reaches a peak of just over  $240 \text{ W m}^{-2}$  at 130°W just north of the equator (cf. Figs. 4e,f). In addition, there is net cooling  $\langle Q_0^{\text{net}} \rangle - \langle F_Q \rangle^{\text{max}} < 0$  over a greater fraction of the year and over more of the zonal distance in the equatorial mixing band, where  $\langle Q_0^{\text{net}} \rangle - \langle F_Q \rangle^{\text{max}} < 0$  between 50% and 75% of the time (Fig. 4d). In the equatorial mixing band, the depth of the peak daily mean turbulent heat flux  $z_{\text{max}}$  ranges from about 90 m at 170°W to 30 m at 95°W (Fig. 5f). In addition,  $z_{\text{max}}$  is virtually always deeper than the MLD and ranges from about 20 to 60 m below the base of the mixed layer in the equatorial mixing band (cf. Figs. 5d–f). The deep  $z_{\text{max}}$  in the equatorial mixing band is consistent with prior studies showing that mixing is particularly strong and

extends to particularly cold isotherms in this band (Holmes et al. 2019a; Deppenmeier et al. 2021). These results are all consistent with the established results that 1) ocean mixing is uniquely strong in the cold tongue near the equator and plays a leading role in the upper-ocean heat budget, 2) the turbulent heat flux peaks in the stratified ocean below the mixed layer, and 3) the intensity of ocean mixing is sensitive to the strong mean vertical shear in the horizontal velocity (e.g., Figs. 1 and 3) that arises from the eastward equatorial undercurrent at depth and westward South Equatorial Current at the surface.

At latitudes between  $2^\circ$  and  $6^\circ$ , both  $\langle Q_0^{\text{net}} \rangle$  and  $\langle F_Q \rangle^{\text{max}}$  range from about 80 to  $0 \text{ W m}^{-2}$  (Figs. 4e,f). The depth  $z_{\text{max}}$  is closer to the base of the MLD than in the equatorial mixing band and just 10–30 m deeper than the MLD on average (cf. Figs. 5e,f). There is also a notable meridional asymmetry in net cooling  $\langle Q_0^{\text{net}} \rangle - \langle F_Q \rangle^{\text{max}} < 0$ ; ocean mixing is stronger relative to the surface flux more frequently and over a significantly greater area to the north of the equator (50%–70%) than to the south (30%–40%; see Fig. 4d). This meridional asymmetry arises partly because  $\langle F_Q \rangle^{\text{max}}$  is stronger, by  $\mathcal{O}(10) \text{ W m}^{-2}$ , between about  $2^\circ$  and  $5^\circ\text{N}$  than between  $2^\circ$  and  $5^\circ\text{S}$ , but also partly because  $\langle Q_0^{\text{net}} \rangle$  is stronger by  $\mathcal{O}(10) \text{ W m}^{-2}$  between  $2^\circ$  and  $5^\circ\text{S}$  than between  $2^\circ$  and  $5^\circ\text{N}$ . The weaker downward surface heat fluxes  $\langle Q_0^{\text{net}} \rangle$  to the north are consistent with warmer SSTs to the north (through their impact on sensible, latent, and

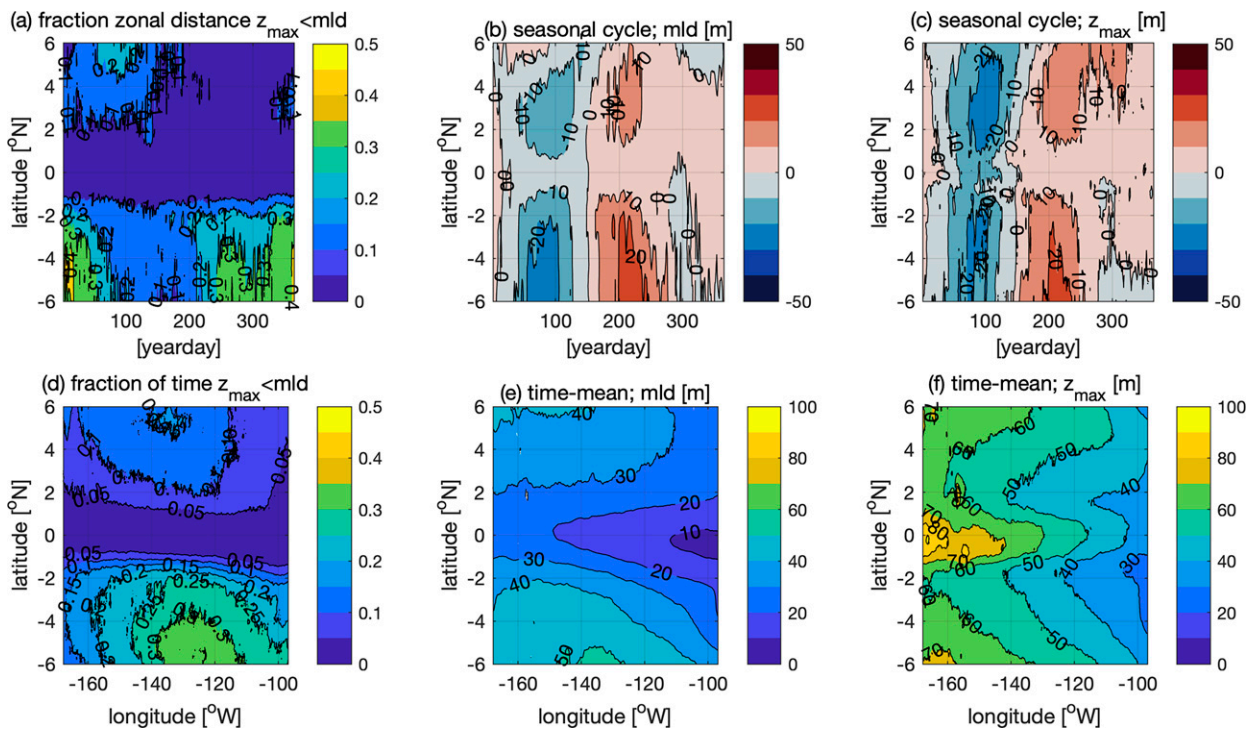


FIG. 5. Climatological comparisons between (b),(e) mixed layer depth (MLD) and (c),(f) the depth  $z_{\max}$  where the downward turbulent heat flux is maximum (i.e., the depth where  $\langle F_Q \rangle^{\max}$  plotted in Fig. 4 occurs). As in Fig. 4, (b) and (c) are the zonal mean anomalies from the time mean, and (e) and (f) are the time-means. In addition, we quantify the fraction of the (a) zonal distance and (d) time over which the MLD is deeper than  $z_{\max}$ . The MLD is defined to be the shallowest depth where water is  $0.015 \text{ kg m}^{-3}$  denser than the top 10 m in the daily mean density profile (since higher-frequency output is not available).

longwave surface heat fluxes). In addition, the asymmetry in time-mean mixing  $\langle F_Q \rangle^{\max}$  is qualitatively consistent with (but does not prove) the hypothesis that DCT and stronger ocean mixing events north of the equator arise due to stronger vertical shear in intermittent tropical instability waves and vortices that are also more energetic north of the equator as proposed by Cherian et al. (2021) (see Fig. 6b). The meridional asymmetry in mixing may also be a manifestation of a meridional asymmetry in SST in that warmer SSTs to the north may contribute to stronger upper-ocean temperature stratification that facilitates enhanced  $\langle F_Q \rangle^{\max}$ .

The model results can be validated using multiyear microstructure observations that are available from  $\chi$  pods on moorings at  $0^\circ$ ,  $140^\circ\text{W}$ , from which an average annual cycle of the turbulent heat flux between 20 and 60 m has been estimated from deployments between 2008 and 2012 (Moum et al. 2013; see also Smyth et al. 2021). Although the observed and modeled time intervals are not identical, we average the model heat fluxes over the same depth range  $\langle F_Q \rangle^{20-60}$  and compare them with the observations of Moum et al. (2013) in Fig. 7. We find that the modeled annual mean  $\langle F_Q \rangle^{20-60}$  is somewhat more than a factor of 2 larger than observed ( $150$  versus  $66 \text{ W m}^{-2}$ ). Restricting the model averaging to the observed years (2008–12) does not change this discrepancy. The maximum flux  $\langle F_Q \rangle^{\max}$  is another  $80 \text{ W m}^{-2}$  higher than  $\langle F_Q \rangle^{20-60}$ , because  $z_{\max} \approx 70 \text{ m}$  is below the 20–60-m averaging range

and the modeled fluxes depend strongly on depth (Fig. 5f). Although it is not fully understood how the time-mean surface heat flux  $\langle Q_0^{\text{net}} \rangle$  is mechanistically coupled to the time-mean subsurface flux  $\langle F_Q \rangle^{\max}$ , it is interesting in light of their high degree of spatial correlation and similar magnitudes that  $\langle Q_0^{\text{net}} \rangle$  is substantially stronger in the model than reported in Moum et al. (2013); Moum et al. (2013) report  $55 \text{ W m}^{-2}$  while the modeled mean is twice as large at  $110 \text{ W m}^{-2}$ . This may indicate that the modeled heat uptake is biased high; this would be consistent with too-strong mixing assuming incomplete compensation for the too-strong mixing by other terms in the heat budget. However, other observational estimates of  $\langle Q_0^{\text{net}} \rangle$  are higher than those reported by Moum et al. (2013). For example, Trenberth and Fasullo (2018) report an estimate of about  $90 \text{ W m}^{-2}$  for the 2000–16 period, and the model seems to be within the range of various estimates from 2001 to 2010 reported by Liang and Yu (2016) (roughly  $60$ – $120 \text{ W m}^{-2}$  at  $0^\circ$ ,  $140^\circ\text{W}$ ; see their Fig. 2). Hence, we do not conclude that the modeled time-mean surface heat flux  $\langle Q_0^{\text{net}} \rangle$  in MITgcm is biased, although it is on the higher end of available estimates.

### c. Seasonal cycle

The climatological seasonal cycle is another metric by which  $\langle F_Q \rangle^{\max}$  and  $\langle Q_0^{\text{net}} \rangle$  are similar at first glance but exhibit



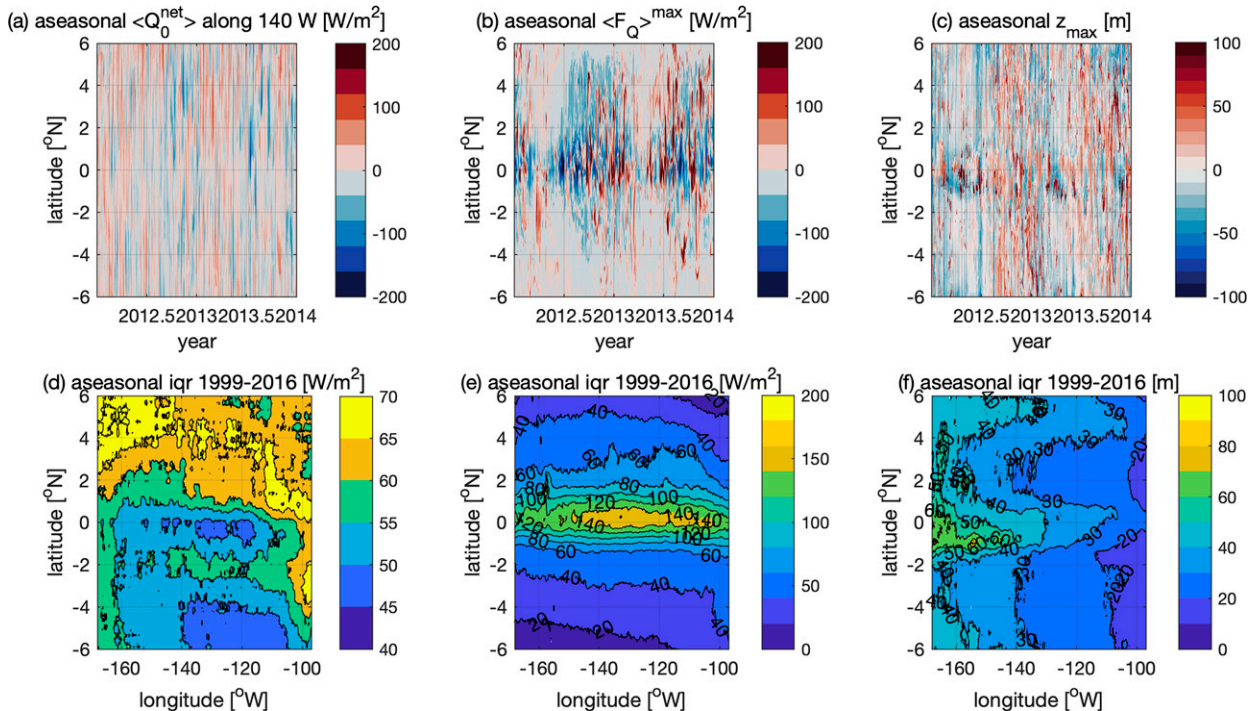


FIG. 6. The top row shows the hindcast aseasonal daily mean vertical heat fluxes during 2012 and 2013 along the 140°W meridian [(a) net surface flux  $\langle Q_0^{\text{net}} \rangle$ , (b) ocean mixing  $\langle F_Q \rangle^{\text{max}}$ , and (c) the depth where strongest mixing occurs  $z_{\text{max}}$ ]. (d)–(f) Maps that quantify the respective aseasonal interquartile ranges over all latitudes and years 1999–2016. Aseasonal variability is defined by subtracting the mean seasonal cycle (i.e., a daily annual climatology, which is averaged over 18 years and then smoothed with a 15-day moving average), from the total signal at each grid point.

notable differences on closer inspection (Figs. 4b,c). Both the seasonal cycles of  $\langle F_Q \rangle^{\text{max}}$  and  $\langle Q_0^{\text{net}} \rangle$  exhibit significant diversity. Four different varieties are present between 6°S and 6°N: one-peak-one-trough, two-peaks-one-trough, two-troughs-one-peak, and two-peaks-two-troughs, and there are variations in the timing, duration and amplitude of the peaks and troughs (peaks are red and troughs are blue in Figs. 4b,c). In addition, these spatio-temporal structures of the seasonal cycles in  $\langle F_Q \rangle^{\text{max}}$  and  $\langle Q_0^{\text{net}} \rangle$  are uncorrelated (pattern correlation  $r^2 < 0.01$  for zonal-mean seasonal anomalies, i.e., between the fields in Figs. 4b,c).

The phase and amplitude of the seasonal cycle of mixing in the equatorial mixing band is similar to observations at 0°, 140°W, even though the modeled time-mean  $\langle F_Q \rangle^{20-60}$  is about a factor of 2 higher than observed [see Fig. 7 and Moum et al. (2013)]. In this equatorial band (see Fig. 4c), the seasonal cycle of mixing  $\langle F_Q \rangle^{\text{max}}$  is not in phase with and has a larger peak-to-trough amplitude than the surface fluxes  $\langle Q_0^{\text{net}} \rangle$  (Figs. 4a–c). In particular, the peak-to-trough amplitudes are about 70 and 140  $\text{W m}^{-2}$  for  $\langle Q_0^{\text{net}} \rangle$  and  $\langle F_Q \rangle^{\text{max}}$ , respectively. It is notable that the observations reported by Moum et al. (2013) show a somewhat smaller peak-to-trough seasonal cycle in  $\langle Q_0^{\text{net}} \rangle \approx 50 \text{ W m}^{-2}$ , although the phasing is similar to the model. In particular,  $\langle Q_0^{\text{net}} \rangle$  is minimum at about yearday 190 and maximum at about yearday 80, whereas mixing reaches a minimum at about yearday 90 and a maximum at about yearday 215. There is also a secondary peak in mixing at about the new year. Hence, there is a strong seasonal cycle in  $\langle Q_0^{\text{net}} \rangle - \langle F_Q \rangle^{\text{max}}$ , which is negative (net cooling) at 0°

along more than 80% of longitudes between 170° and 95°W in the boreal summer and early autumn (Fig. 4a), when the SST cools in the equatorial mixing band (Moum et al. 2013). Conversely,  $\langle Q_0^{\text{net}} \rangle - \langle F_Q \rangle^{\text{max}} < 0$  at only about 20% of longitudes in boreal spring (Fig. 4a), when the SST warms (Moum et al. 2013). These results highlight again the importance of seasonal variations in ocean mixing for the seasonal cycle of cold tongue SST. The seasonal cycle of the MLD and the depth  $z_{\text{max}}$  are highly correlated throughout the cold tongue. In the equatorial mixing band, minima are achieved at about yearday 90 and local maxima at about yearday 210 (Figs. 5b,c;  $r^2 = 0.76$ ). But, the amplitude of the seasonal cycles are relatively modest with peak-to-trough amplitudes of only about 15 and 25 m for the MLD and  $z_{\text{max}}$ , respectively.

A qualitatively similar seasonal cycle is found off the equator in  $\langle Q_0^{\text{net}} \rangle$  (Fig. 4b), but the off-equatorial seasonal cycle in  $\langle F_Q \rangle^{\text{max}}$  (Fig. 4c) is much weaker and has a different phase relative to the equator. In addition, the amplitude of the seasonal cycle in  $\langle F_Q \rangle^{\text{max}}$  is notably asymmetric across the equator. There is a much stronger seasonal cycle to the north than the south; for example, the peak-to-trough seasonal cycle amplitude is about 30  $\text{W m}^{-2}$  at 4°N but only 10  $\text{W m}^{-2}$  at 4°S (Fig. 4c). The stronger seasonal cycle in ocean mixing to the north of the equator is qualitatively consistent with (but does not prove) the hypothesis that the seasonal cycle is due at least partially to tropical instability waves, which have greatest variance from boreal summer to winter (Cherian et al. 2021), although

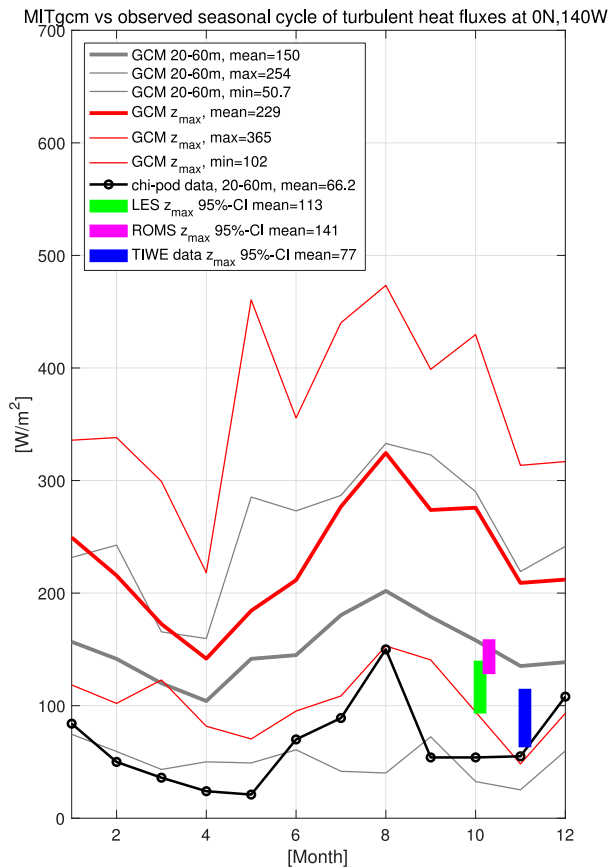


FIG. 7. Climatological annual cycle of the downward turbulent heat flux at  $0^\circ$ ,  $140^\circ\text{W}$  in the MITgcm regional ocean model, including monthly means at  $z_{\text{max}}$  ( $\langle F_Q \rangle^{\text{max}}$ , thick red) as well as monthly means from 20- to 60-m depth ( $\langle F_Q \rangle^{20-60}$ ) (thick gray). Corresponding minima and maxima of monthly ( $\langle F_Q \rangle^{20-60}$ ) (thin gray) and ( $\langle F_Q \rangle^{\text{max}}$ ) (thin red) from 1999 to 2016 are included. For comparison, the observational climatology of ( $\langle F_Q \rangle^{20-60}$ ) from  $\chi$  pods (Moum et al. 2013) is plotted in black circles. The 95% confidence intervals for the monthly mean ( $\langle F_Q \rangle^{\text{max}}$ ) from ROMS and LES (roughly October 1985) as well as the TIWE observations (roughly November 1991) are in magenta, green, and blue, respectively. Note, however, that the LES and TIWE are computed as  $(\rho_c/g\alpha)F_b = 1.37 \times 10^9 F_b \approx F_Q$  ( $\text{W m}^{-2}$ ), where  $\rho$ ,  $c_p$ , and  $\alpha$  are the reference density, specific heat, and thermal expansion coefficient of seawater, respectively,  $g$  is the acceleration due to gravity, and  $F_b$  is the downward turbulent buoyancy flux. Data from two other shorter field experiments (not shown) resulted in means of roughly  $400 \text{ W m}^{-2}$  in October/November 2008 (Moum et al. 2009) and  $100 \text{ W m}^{-2}$  in November 1984 (Gregg et al. 1985; Moum and Caldwell 1985) (see Fig. 2d of Moum et al. 2009).

precisely quantifying and even determining the sign of the rectified effect of tropical instability waves on ocean mixing is difficult (Holmes and Thomas 2015).

#### d. Aseasonal variability

Like the dissipation of turbulent kinetic energy (Crawford 1982; Moum et al. 1989; Smyth et al. 2021), the maximum

daily mean turbulent heat flux ( $F_Q$ )<sup>max</sup> is highly variable and logarithmically distributed (Fig. 8). Thus, the arithmetic averages of ( $F_Q$ )<sup>max</sup> are significantly influenced by relatively infrequent strong mixing events (in contrast to ( $Q_0^{\text{net}}$ )). It follows that the processes underpinning the aseasonal variability in general and infrequent strong mixing events in particular are significant for climatological statistics including the time mean. Hence, we conclude this section on the regional climatological statistics by quantifying the aseasonal variability in ( $F_Q$ )<sup>max</sup> and ( $Q_0^{\text{net}}$ ), both to provide climatological context for and motivate a more detailed discussion of subseasonal variability in ( $F_Q$ )<sup>max</sup> simulated in LES (for discussion of the physics of subseasonal variability in ocean models, see, e.g., Holmes and Thomas 2015, 2016; Inoue et al. 2019; Liu et al. 2019a,b, 2020; Cherian et al. 2021). When plotting (in Fig. 6) and reporting the statistics from the MITgcm results in this section, the aseasonal variability is separated from the full signal (i.e., defined) by subtracting a daily climatology, which is first averaged over 18 years and then smoothed by applying a 15-day moving average. Hence, aseasonal variability includes both interannual and intra-annual time scales.

First, it may be noted that the minimum and maximum monthly means ( $F_Q$ )<sup>max</sup> across the 18 simulated years (thin red lines in Fig. 7) span a factor of 3–8 or roughly  $50\text{--}250 \text{ W m}^{-2}$ . So, any given monthly mean is reasonably likely to differ from the corresponding monthly climatology by a factor of 2. In addition, time series of aseasonal ( $F_Q$ )<sup>max</sup> along  $140^\circ\text{W}$  in Fig. 6b reveal variability in ( $F_Q$ )<sup>max</sup> of hundreds of watts per square meter on time scales from days to months in 2012–13. A qualitative comparison of the modeled distribution of ( $F_Q$ )<sup>max</sup> at  $0^\circ$ ,  $140^\circ\text{W}$  (Fig. 8a) to the spread of observed daily mean dissipation from  $\chi$  pods in Fig. B1 of Smyth et al. (2021) suggests that there are fewer instances of weak mixing and a narrower distribution of mixing values in the model compared to observations at  $0^\circ$ ,  $140^\circ\text{W}$ . But, the different vertical averaging precludes a quantitative comparison (see Fig. 7). Aseasonal variability in mixing exhibits a spatial pattern that is similar to the mean (cf. Figs. 6e and 4f), consistent with a logarithmic distribution. In particular, the interquartile range (IQR) of aseasonal ( $F_Q$ )<sup>max</sup> variability reaches  $150 \text{ W m}^{-2}$  in the strong equatorial mixing band but drops from 60 to  $20 \text{ W m}^{-2}$  at latitudes from  $2^\circ$  to  $6^\circ$ . There is also a notable seasonal cycle to aseasonal variability, which is stronger in boreal autumn than boreal spring (Fig. 6b; cf. Fig. 4c), as well as meridional asymmetry across the equator with larger aseasonal variability to the north than to the south (Fig. 6e). Both the seasonal cycle and meridional asymmetry of aseasonal variability are consistent with tropical instability wave activity (Halpern et al. 1988; Moum et al. 2009; Cherian et al. 2021). There is also notable aseasonal variability in the depth at which maximum ocean mixing occurs  $z_{\text{max}}$  (Figs. 8e and 6c,f). The aseasonal variability in  $z_{\text{max}}$  has a similar spatial pattern as the time-mean  $z_{\text{max}}$  (cf. Figs. 5f and 6f). The IQR of aseasonal  $z_{\text{max}}$  variability is about 40 m at  $170^\circ\text{W}$  and 10 m at  $95^\circ\text{W}$ . This zonal gradient in the aseasonal IQR of  $z_{\text{max}}$  is qualitatively similar at all latitudes from  $6^\circ\text{S}$  to  $6^\circ\text{N}$ , but the IQR is elevated by 10–20 m in the equatorial mixing band relative to other latitudes (Fig. 6f).

Aseasonal variability in ( $Q_0^{\text{net}}$ ) is qualitatively different from aseasonal variability in ( $F_Q$ )<sup>max</sup> (cf. Figs. 6a,b and cf. Figs. 8a,c).

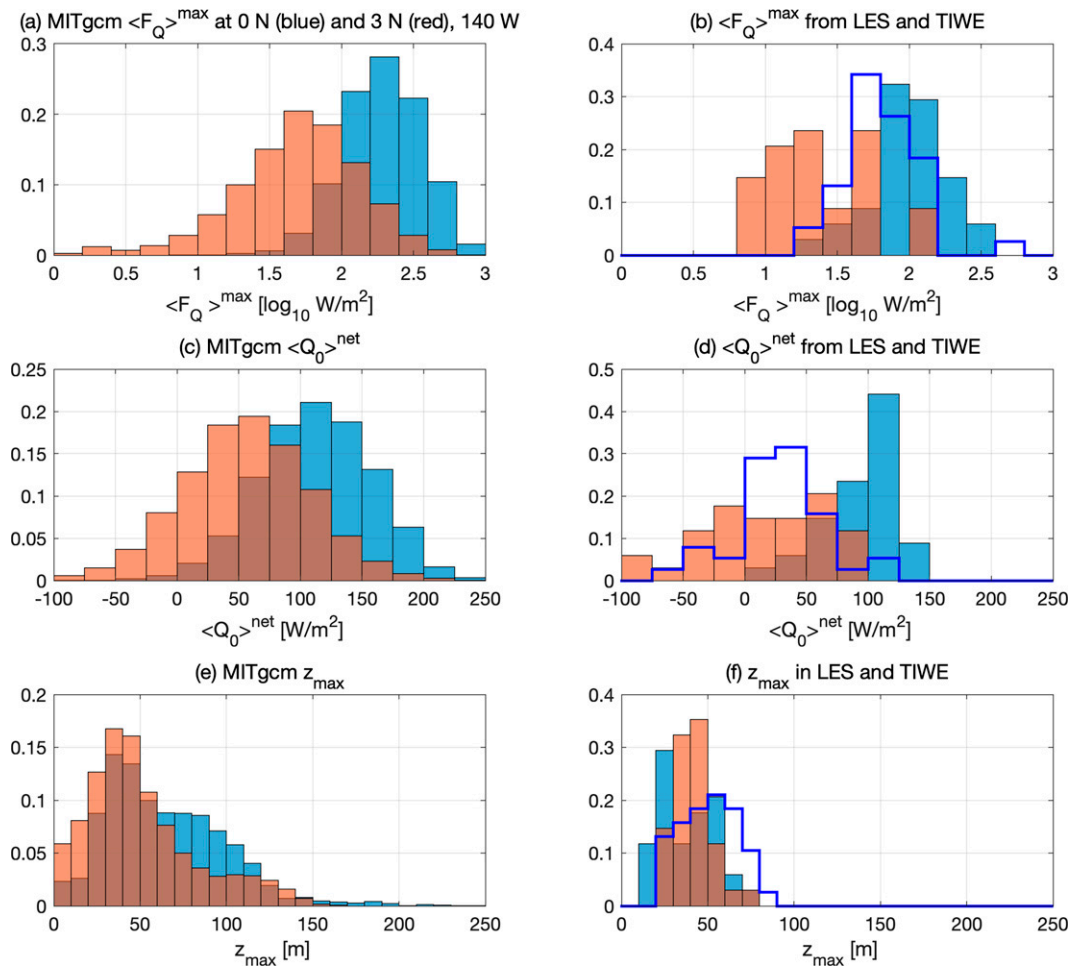


FIG. 8. (a),(b) Relative probability distributions of the maximum daily mean turbulent heat flux due to ocean mixing  $\langle F_Q \rangle^{\max}$ , (c),(d) the daily mean net surface heat flux  $\langle Q_0^{\text{net}} \rangle$ , and (e),(f) the depth  $z_{\max}$  at which  $\langle F_Q \rangle^{\max}$  occurs. Histograms are included for both  $0^\circ$ ,  $140^\circ\text{W}$  (blue) and  $3^\circ\text{N}$ ,  $140^\circ\text{W}$  (red) for (left) the 18-yr MITgcm simulation as well as (right) the 34-day LES in October 1985 (red and blue histograms) and the 38-day TIWE experiment at  $0^\circ$ ,  $140^\circ\text{W}$  in November 1991 (dark-blue edged bars). Note that the data from LES and TIWE are computed based on buoyancy fluxes, e.g.,  $(\rho_p/g\alpha)F_b = 1.37 \times 10^9 F_b \approx F_Q$ .

First,  $\langle Q_0^{\text{net}} \rangle$  is more nearly normally distributed (Fig. 8c), and the IQR varies relatively little across the cold tongue from about 45 to  $70 \text{ W m}^{-2}$  (Fig. 6d). In addition, the maximum Pearson's  $r^2$  between asseasonal anomalies in  $\langle Q_0^{\text{net}} \rangle$  and  $\langle F_Q \rangle^{\max}$  is only 0.15 (at about  $2.5^\circ\text{S}$ ,  $110^\circ\text{W}$ ) and the correlations are mostly much smaller (mean  $r^2 = 0.02$  and median  $r^2 = 0.01$ ). Hence, the asseasonal net surface heat flux  $\langle Q_0^{\text{net}} \rangle$  anomalies do not covary with the asseasonal turbulent heat flux  $\langle F_Q \rangle^{\max}$  anomalies in the model (see Fig. 3i of Smyth et al. (2021) for a qualitatively similar observational result at  $0^\circ$ ,  $140^\circ\text{W}$ ).

#### 4. Subseasonal variability on and off the equator in the LES

To build further understanding of the subseasonal variability in ocean mixing and DCT, both on and off the equator, we turn to the LES (see section 2 and the appendix for details).

First, section 4a describes how the metrics of ocean mixing (originally defined in section 3a) are applied to the LES and in observational comparisons to the Tropical Instability Wave Experiment (TIWE; Lien et al. 1995). Section 4b summarizes and contextualizes these LES via comparisons with prior results. Then, sections 4c–4g quantify the daily mean turbulent buoyancy flux  $\langle F_b \rangle$ , including the vertical extent of strong mixing (section 4c), the energetics of mixing (section 4d), and the covariability of mixing with nonturbulent variables that may facilitate mixing parameterization (sections 4e–4g).

##### a. Metrics of mixing and observational comparisons

Throughout the analysis of the LES we continue to focus on the maximum of the daily mean flux profile, but we shift our focus from the turbulent heat flux  $\langle F_Q \rangle^{\max}$  to the turbulent buoyancy flux  $\langle F_b \rangle^{\max}$  to leverage links with turbulence energetics, in which  $F_b$  appears but not  $F_Q$  (see the appendix

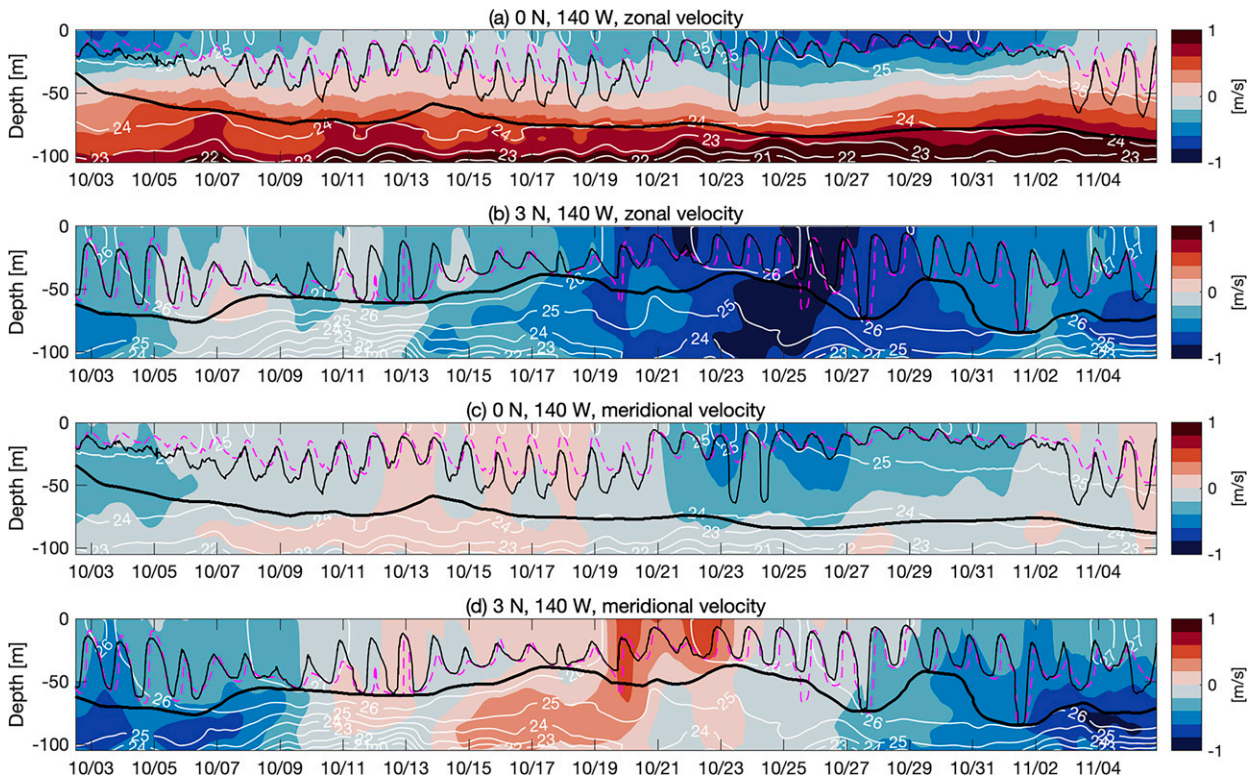


FIG. 9. Time series of zonal and meridional velocity (color), temperature (white contours; °C), mixed layer depth (MLD; dashed magenta), the depth where the bulk Richardson number  $Ri_b = 0.2$  ( $H_{Ri_b}$ ; thin black), and the base of the low-gradient Richardson number layer  $Ri_g < 0.35$  ( $H_{Ri_g}$ ; thick black) in the LES at  $0^\circ$  and  $3^\circ\text{N}$  along  $140^\circ\text{W}$ . All fields are defined from horizontally averaged profiles. The MLD is defined to be the shallowest depth where water is  $0.015 \text{ kg m}^{-3}$  denser than the top 10 m in the instantaneous but horizontally averaged density profile. All time tick marks are at 0000 UTC; local solar time at  $0^\circ$ ,  $140^\circ\text{W}$  is about 9 h behind UTC, so local solar noon is at about 2100 UTC.

for the relevant equations). However, to facilitate comparisons between the LES and the MITgcm simulations and the  $\chi$ pod observations (Fig. 7), we often report

$$\frac{\rho c_p}{g\alpha} F_b \approx F_Q, \quad (2)$$

where  $\rho$  is the reference density of seawater,  $c_p$  is the specific heat of seawater,  $g$  is the acceleration due to gravity, and  $\alpha$  is the thermal expansion coefficient of seawater. In the LES, the coefficient fraction is constant  $1.37 \times 10^9 \text{ (W m}^{-2} \text{ s}^3 \text{ m}^{-2}\text{)}$  (see the appendix for details) and we apply the same constant scaling to produce  $F_Q$  from the TIWE data in Figs. 7 and 8. At  $z_{\text{max}}$ , the relative error in approximating a constant ratio  $F_Q/F_b$  is roughly

$$\frac{N_T^2}{N^2} - 1, \quad (3)$$

assuming the turbulent vertical fluxes of temperature and buoyancy can be approximated using local flux–gradient relationships (i.e., downgradient diffusion) and have the same turbulent diffusivity such that

$$\frac{F_Q}{F_b} \approx \frac{\rho c_p \partial T / \partial z}{\partial b / \partial z} = \frac{\rho c_p N_T^2}{g\alpha N^2}, \quad (4)$$

where  $N_T^2 = g\alpha \partial T / \partial z$ . The errors from this approximation are small; the 68 days of LES estimates of  $\langle F_Q \rangle^{\text{max}}$  yields an estimate for the mean bias of +6% (−7% and +20% at  $0^\circ$  and  $3^\circ\text{N}$ , respectively) and a standard deviation of 26% (10% and 30% at  $0^\circ$  and  $3^\circ\text{N}$ , respectively).

We explicitly compare the LES results to 38 days of observations of DCT from the TIWE at  $0^\circ$ ,  $140^\circ\text{W}$  in November–December 1991 (Lien et al. 1995). The TIWE dataset is a uniquely good point of comparison in that it includes a similarly long 38 days of hourly averaged turbulence profiles based on thousands of microstructure casts (roughly 6–7 per hour) as well as relevant ocean velocity and density profiles and surface flux information derived from continuous occupation of a station at  $0^\circ$ ,  $140^\circ\text{W}$  by two ships. Although turbulent heat and buoyancy fluxes are not directly measured, they are inferred to within about a factor of 2 using the relationship  $F_b = \Gamma \epsilon$  where  $\epsilon$  is the observed dissipation rate of turbulent kinetic energy and a mixing efficiency factor is assumed to be a constant  $\Gamma = 0.2$  at depths below 20 m for simplicity (Osborn 1980; Gregg et al. 2018). The maximum of the daily mean turbulent buoyancy flux  $\langle F_b \rangle^{\text{max}}$  is calculated after first binning hourly mean  $F_b$  profiles into daily means  $\langle F_b \rangle$  at 1-m vertical resolution and then smoothing  $\langle F_b \rangle$  with a 10-m moving average. The resulting 38-day mean  $\langle F_b \rangle^{\text{max}} (\rho c_p) / (g\alpha) \approx$

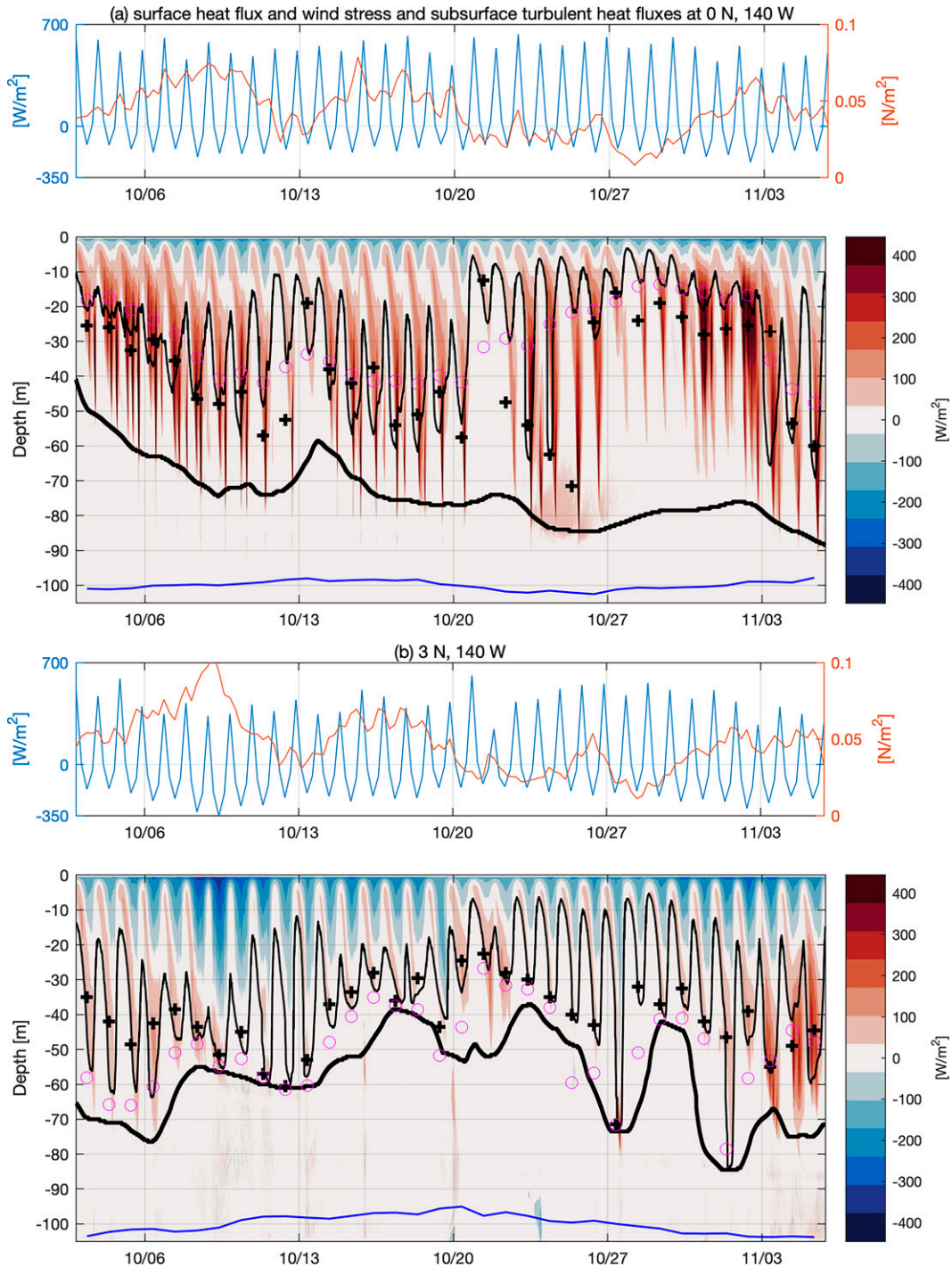


FIG. 10. Time series of the net surface heat flux  $Q_0^{\text{net}}$  (left axis; blue), the magnitude of the wind stress  $|\tau|$  (right axis; red), and the subsurface downward turbulent heat flux  $F_Q$  profiles from October to November 1985 in the LES at (a)  $0^\circ$  and (b)  $3^\circ\text{N}$  along  $140^\circ\text{W}$ . Overlaid on  $F_Q$  are the depth at which the bulk Richardson number  $\text{Ri}_b = 0.2$  ( $H_{\text{Ri}_b}$ ; thin black line), the depth of the maximum daily mean downward heat flux  $z_{\text{max}}$  (+ symbols), the daily maximum MLD (defined from the horizontally averaged LES density profiles; magenta circles), and the base of the low gradient Richardson layer  $\text{Ri}_g < 0.35$  ( $H_{\text{Ri}_g}$ ; thick black line). The daily mean meridional velocity averaged from 25- to 75-m depth is in blue; the origin is at a depth of 100 m, a 1-m spacing corresponds to  $10 \text{ cm s}^{-1}$ , and the peak-to-trough amplitudes are about  $40 \text{ cm s}^{-1}$  at  $0^\circ$  and  $90 \text{ cm s}^{-1}$  at  $3^\circ\text{N}$ . For consistency with other results in section 4, we plot  $(\rho c_p / g \alpha) F_b = 1.37 \times 10^9 F_b \approx F_Q$  ( $\text{W m}^{-2}$ ), where  $\rho$ ,  $c_p$ , and  $\alpha$  are the reference density, specific heat, and thermal expansion coefficient of seawater, respectively;  $g$  is the acceleration due to gravity; and  $F_b$  is the downward turbulent buoyancy flux. All time tick marks are at 0000 UTC, but local solar time at  $0^\circ$ ,  $140^\circ\text{W}$  is about 9 h behind UTC, so local solar noon is at about 2100 UTC. Daily mean statistics (e.g.,  $z_{\text{max}}$  indicated by + symbols) are calculated from 2100 UTC so that the averages begin and end near solar noon.

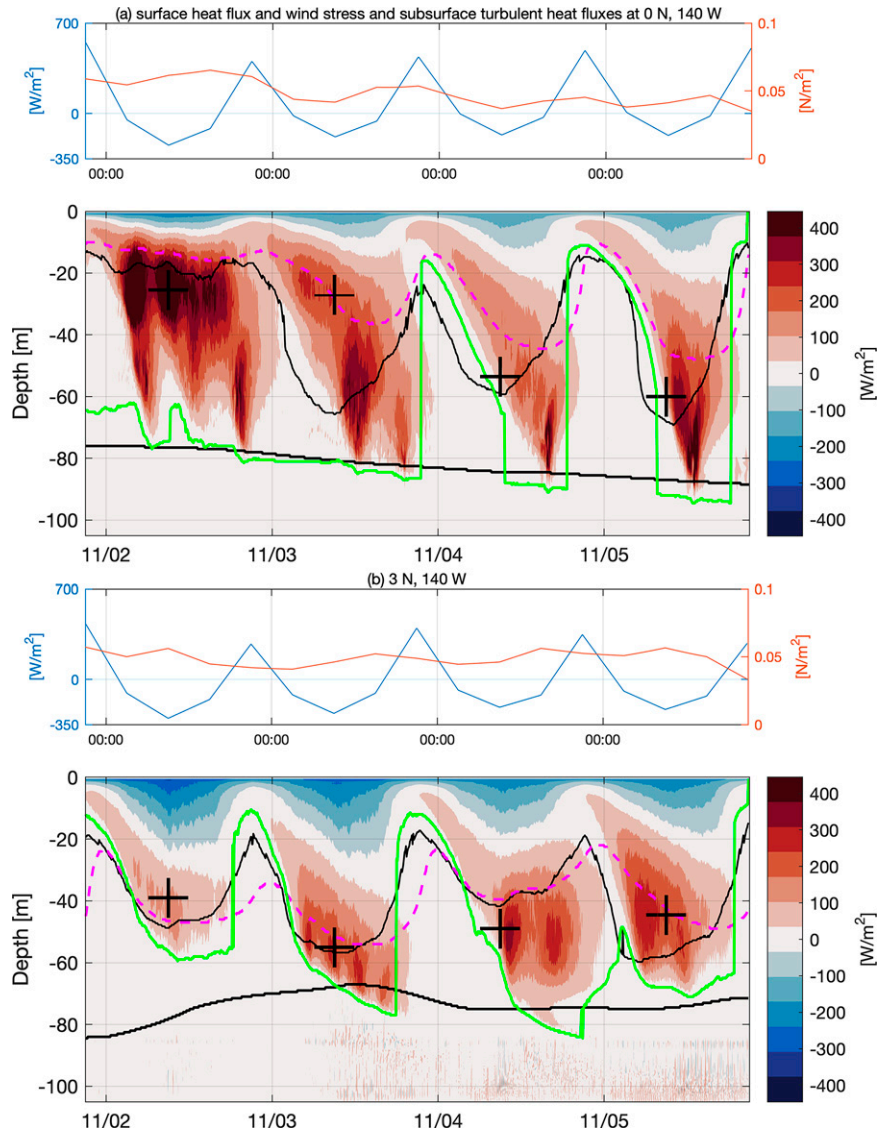


FIG. 11. As in Fig. 10, but zoomed in on a few days in November and with the addition of the MLD (dashed magenta) and the DCT penetration depth  $z_{\text{pen}}$  ( $\epsilon \geq 2 \times 10^{-8} \text{ m}^2 \text{ s}^{-3}$ ; thin green). The MLD is defined to be the shallowest depth where water is  $0.015 \text{ kg m}^{-3}$  denser than the top 10 m in the instantaneous but horizontally averaged density profile.

$\langle F_Q \rangle^{\text{max}}$  based on the TIWE data is plotted in Fig. 7 and the distribution of the daily means is shown in Fig. 8 for context. As in the analysis of the LES, we apply the assumption of constant  $\langle F_Q \rangle^{\text{max}} / \langle F_b \rangle^{\text{max}}$  to the TIWE observations (in Fig. 7). We estimate that this assumption yields larger but still modest high bias in the  $\langle F_Q \rangle^{\text{max}}$  of up to about +30%, which is smaller than the factor of 2 observational uncertainty. Hourly mean velocity and density from the ADCP and CTD, respectively, are extended to the surface by replicating the top reliable value before calculating vertical gradients in horizontal velocity and buoyancy and related derived quantities.

#### b. Summary and context

We chose to run LES at  $0^\circ$  and  $3^\circ\text{N}$  along  $140^\circ\text{W}$  in October 1985, which was characterized by neutral oceanic Niño index, so mixing is expected to be reasonably strong but not maximal both at and north of the equator (Figs. 4 and 7) (see also Warner and Moum 2019; Huguenin et al. 2020; Deppenmeier et al. 2021). Tropical instability waves are a dominant cause of subseasonal variability in currents and density in the LES and are also an important driver of aseasonal variations in mixing (e.g., Moum et al. 2009; Cherian et al. 2021). The 34-day simulations are just long enough to span one full tropical instability

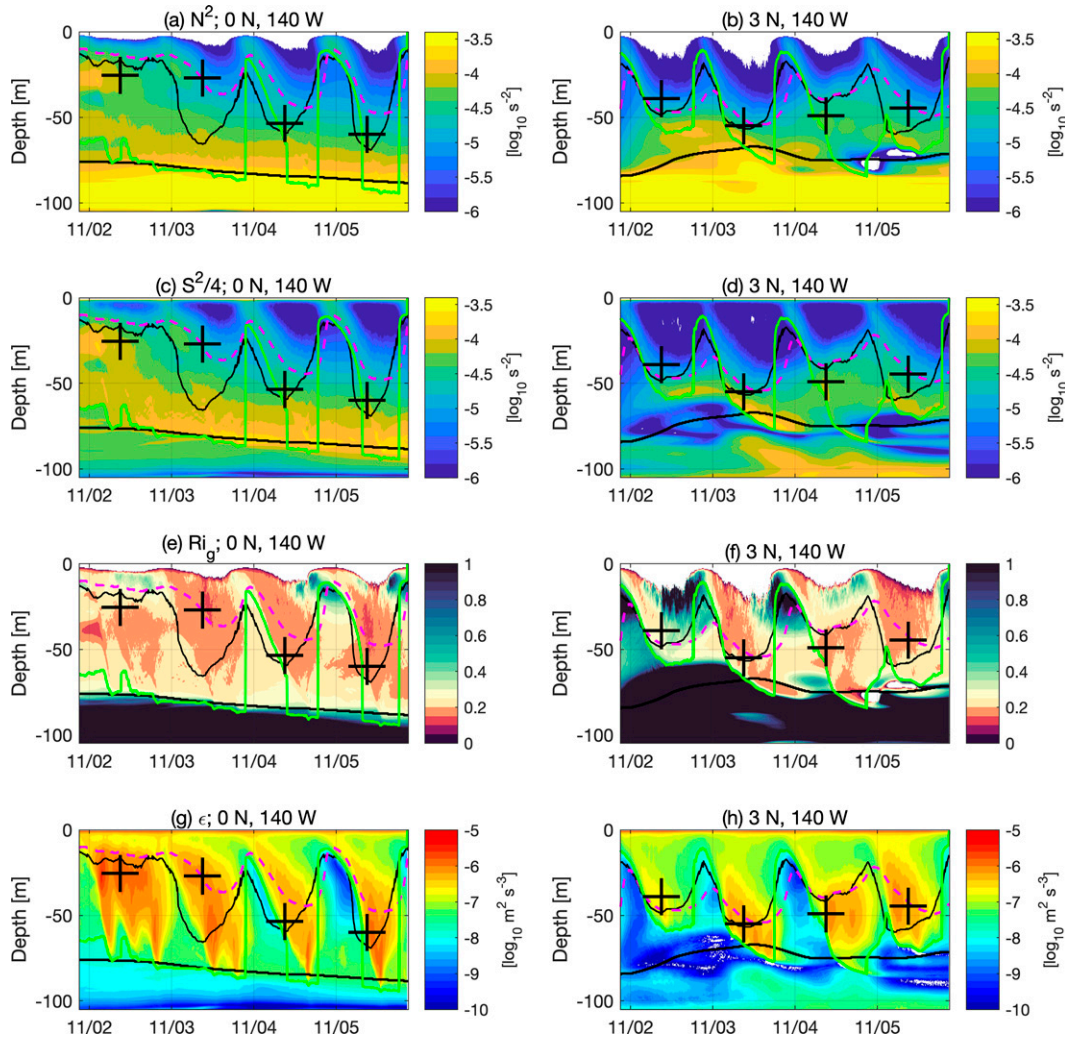


FIG. 12. As in Fig. 11, but plots show (a),(b) the vertical buoyancy gradient  $N^2$ ; (c),(d) the squared vertical shear  $S^2$ ; (e),(f)  $Ri_g = N^2/S^2$ ; and (g),(h) the rate of dissipation of kinetic energy  $\epsilon$ . It may be noted that there are a few instances of elevated dissipation  $10^{-8} < \epsilon < 10^{-7} \text{ m}^2 \text{ s}^{-3}$  below the deepest depths of DCT ( $z_{\text{pen}}$ ; green line) in (h) where  $Ri_g > 1$ . However, these instances of elevated dissipation near the bottom are dominated by dissipation of the mean-flow kinetic energy, and the turbulent fluxes and energetics depend strongly on the subgrid-scale parameterization in the LES (A6) and (A7), may be influenced by the bottom boundary, and should be interpreted with caution.

wave period, but the tropical instability wave spanned by these LES is not especially strong. The peak-to-trough amplitude of the meridional velocity averaged from 25 to 75 m is only  $45 \text{ cm s}^{-1}$  at  $0^\circ$  and  $88 \text{ cm s}^{-1}$   $3^\circ\text{N}$  (Fig. 9). For comparison, the peak-to-trough amplitude of the meridional velocity variability during the TIWE is about  $50 \text{ cm s}^{-1}$  (Plate 3 in Lien et al. 1995) and quite similar to the LES at the same site, even though tropical instability waves were weak during the TIWE due to the onset of El Niño conditions. In contrast, Moum et al. (2009) observed strong turbulent mixing in the presence of a strong tropical instability wave with peak-to-trough meridional velocity amplitude of about  $1.5 \text{ m s}^{-1}$  at  $0^\circ$ ,  $140^\circ\text{W}$  during October–November 2008 in La Niña conditions (see also Inoue et al. 2012, 2019).

We find that the mixing in the LES qualitatively reflects the seasonal, interannual and mesoscale context. The 34-day mean  $\langle F_Q \rangle^{\text{max}}$  in the LES at  $0^\circ$  (about  $110 \text{ W m}^{-2}$ ) is just above the minimum of the 18 October means simulated from 1999 to 2016 in the MITgcm. In addition, the LES parent ROMS simulation with the same KPP mixing scheme as the MITgcm also has a rather low mean  $\langle F_Q \rangle^{\text{max}} \approx 140 \text{ W m}^{-2}$  (compared to an October mean of about  $275 \text{ W m}^{-2}$  in the MITgcm), suggesting that the large-scale conditions (e.g., shear, stratification, and air–sea fluxes) in the simulated October 1985 are not exceptional but not as conducive to strong mixing as is typically the case from 1999 to 2016. However, the 34-day mean  $\langle F_Q \rangle^{\text{max}}$  is still larger than the 38-day mean  $\langle F_Q \rangle^{\text{max}}$  from the TIWE observations ( $77 \text{ W m}^{-2}$ ) and about

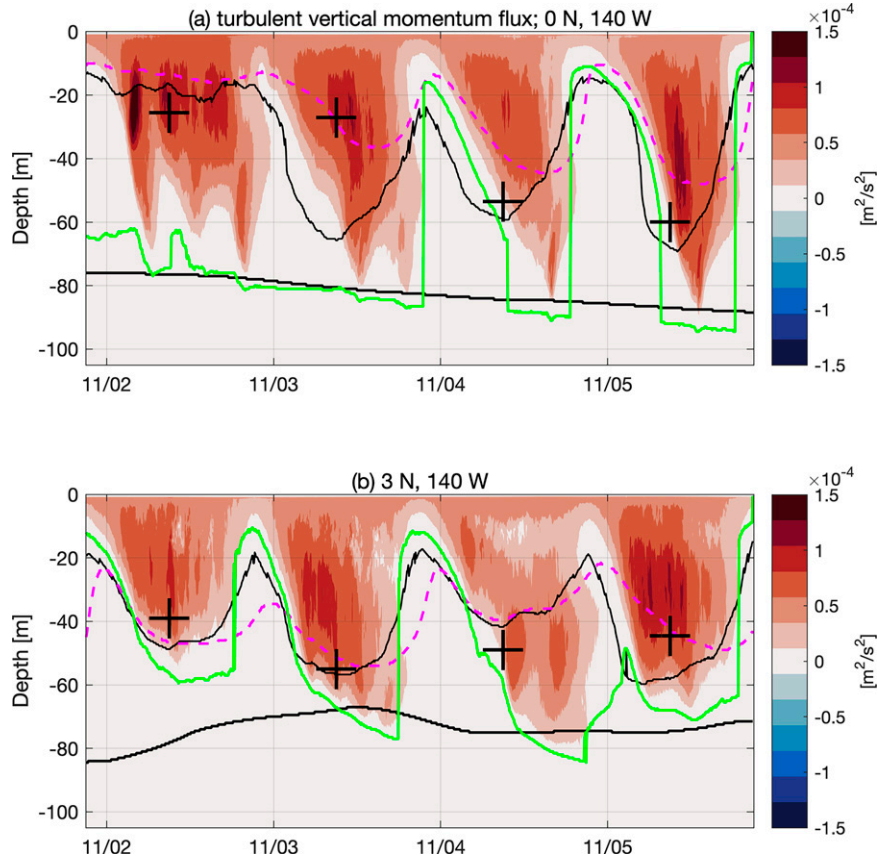


FIG. 13. As in Fig. 11, but turbulent vertical momentum fluxes projected onto the shear, i.e.,  $(\mathbf{F}_m \cdot \partial \mathbf{u}_h / \partial z) / |\partial \mathbf{u}_h / \partial z|$ .

50% above the climatological  $\langle F_Q \rangle^{20-60}$  (averaged from 20- to 60-m depth) from  $\chi$ pod observations in October. Noting that  $\langle F_Q \rangle^{\max} / \langle F_Q \rangle^{20-60} \approx 1.5-2$  in the MITgcm, these results suggest that the mixing in the LES is fairly typical for October. Consistent with this conclusion, the mixing in our LES is also stronger than that simulated in the LES of Sarkar and Pham (2019) (see also Pham et al. 2017), in which the resolved turbulent heat flux was about  $60 \text{ W m}^{-2}$  and  $\epsilon \approx 10^{-7} \text{ m}^2 \text{ s}^{-3}$  at the maximum MLD over three days in October at  $0^\circ$ ,  $140^\circ\text{W}$  (compared to  $\langle F_Q \rangle^{\max} \approx 110 \text{ W m}^{-2}$  and  $\langle \epsilon \rangle^{\max} \approx 3 \times 10^{-7} \text{ m}^2 \text{ s}^{-3}$  here). Conversely, the mixing in our LES is substantially weaker than the especially strong mixing (with time-mean  $F_Q \approx 400 \text{ W m}^{-2}$  and  $\epsilon \approx 10^{-6} \text{ m}^2 \text{ s}^{-3}$ ) observed by Moum et al. (2009) at  $0^\circ$ ,  $140^\circ\text{W}$  in the midst of a strong tropical instability wave during October–November 2008 in La Niña conditions. Finally, the time-averaged  $\langle F_Q \rangle^{\max}$  in the LES at  $3^\circ\text{N}$ ,  $140^\circ\text{W}$  is about  $30 \text{ W m}^{-2}$ , that is 1/4 to 1/3 of the magnitude in the LES at  $0^\circ$ ,  $140^\circ\text{W}$ . This ratio of  $\langle F_Q \rangle^{\max}$  at  $3^\circ\text{N}$  over  $\langle F_Q \rangle^{\max}$  at  $0^\circ$  is approximately consistent with the climatological ratio from 1999 to 2016 found in the MITgcm even though the mixing in the LES is weaker at both latitudes (Fig. 4f).

Consistent with earlier studies, we find that the diurnal cycle is the dominant mode of temporal variability in the turbulence near the surface, and the simulated diurnal cycles at  $0^\circ$ ,  $140^\circ\text{W}$

exhibit many of the previously observed and simulated features of DCT at that location (Gregg et al. 1985; Moum et al. 1989; Schudlich and Price 1992; Peters et al. 1994; Lien et al. 1995; Wang et al. 1998; Large and Gent 1999; Danabasoglu et al. 2006; Smyth et al. 2013; Pham et al. 2013, 2017; Smyth et al. 2017; Sarkar and Pham 2019; Pei et al. 2020; Cherian et al. 2021). For example,  $F_Q$  is shown in Figs. 10a and 11a and can be compared to the time series of the dissipation rate of turbulent kinetic energy  $\epsilon$  observed during the TIWE in Plate 7 of Lien et al. (1995) ( $\epsilon \approx 5F_b \approx 4F_Q \times 10^{-9} \text{ m}^2 \text{ s}^{-3}$  below the MLD; see also Fig. 12). During the daytime, shortwave radiation stratifies a shallow near-surface layer where wind-driven turbulence is confined and accelerates a near-surface current with strong vertical shear. During the afternoon and early evening, the stabilizing net surface buoyancy flux weakens and eventually becomes destabilizing. The near-surface shear and stratification descend downward toward the highly sheared and stratified but marginally unstable layer below, where  $\text{Ri}_g \approx 1/4$  (Fig. 12). At the same time, strong turbulent heat and momentum fluxes  $F_Q$  and  $\mathbf{F}_m$  as well as dissipation rates  $\epsilon$  descend downward as well (Figs. 11–13; see the appendix for definitions). During nighttime and early morning, turbulence penetrates deeply below the MLD and into the stratified thermocline (i.e., between about 30- and 90-m depth), where downward turbulent heat fluxes  $F_Q$  reach a subsurface maximum



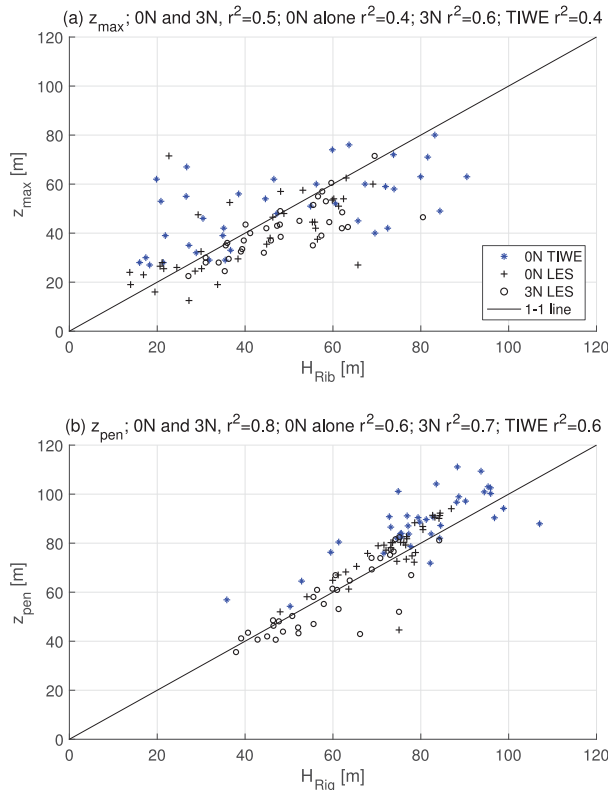


FIG. 14. (a) The depth  $z_{\max}$  of maximum daily mean turbulent heat flux is related to the depth  $H_{\text{Rib}}$  at which the bulk Richardson number is 0.2. (b) The daily maximum depth  $z_{\text{pen}}$  to which DCT penetrates ( $\epsilon > 2 \times 10^{-8} \text{ m}^2 \text{ s}^{-3}$ ) is related to the low-gradient Richardson layer depth  $H_{\text{Rig}}$  (above which  $\text{Ri}_g < 0.35$ ).

of hundreds of watts per square meter. Strong turbulent momentum fluxes extract kinetic energy from the shear to drive strong heat fluxes and dissipation rates in the thermocline (Figs. 11–13; the energetics is quantified in section 4d). The strong turbulence that is energized locally below the MLD often persists there for hours while the extent and intensity of the near-surface turbulence decline with increasing solar radiation in the morning. In addition, on many nights and mornings there are 2–4 bursts of particularly strong turbulence that cause the heat flux to be elevated by up to hundreds of watts per square meter for hours (Fig. 11a) as observed (Smyth et al. 2017).

At first glance, the diurnal cycles of turbulent heat fluxes  $F_Q$  at 3°N in Fig. 10b seem to differ qualitatively from those at 0°, consistent with the hypothesis that equatorial turbulence is enhanced relative to turbulence at higher latitudes due to DCT associated with the strong mean shear between the eastward undercurrent and the westward surface South Equatorial Current (Figs. 1a and 9a). However, DCT and strong heat and momentum fluxes do occur at 3°N in conjunction with strong vertical shear of horizontal velocity (Figs. 9b,d), most prominently on 3–5 November when the subsurface turbulence at 3°N exhibits all of the qualitative features described in the previous paragraph in reference to the DCT at 0° (Figs. 11–13). In addition, some days in early and mid-October exhibit

downward turbulent heat fluxes  $F_Q$  below the MLD, although the intensity of these subsurface heat fluxes is weaker than most days at 0° and there are no obvious nighttime turbulent bursts. These results add significant new support to the hypothesis that DCT occurs off the equator. Off-equatorial DCT has previously been hypothesized based on ocean model results with fully parameterized DCT (Pei et al. 2020; Cherian et al. 2021) but has not been previously simulated in LES or observed in microstructure. Although the diurnal cycle of DCT remains a topic of interest for future analysis of our LES, this topic has received substantial attention in prior LES studies (Wang et al. 1998; Large and Gent 1999; Pham et al. 2013, 2017; Sarkar and Pham 2019) and we leave further analysis of the diurnal cycle in these LES to future work.

The objective of this analysis of the LES is to build understanding of the subseasonal variability of the daily mean  $\langle F_Q \rangle$  on time scales from days to weeks, building on our analysis of the regional MITgcm. The distributions of  $\langle F_Q \rangle^{\max}$ ,  $z_{\max}$ , and  $\langle Q_0^{\text{net}} \rangle$  in Fig. 8 show how this variability simulated in the LES compares to the variability in the MITgcm and observed in the TIWE data and generally support the suggestion that the LES are representative of fairly typical conditions in October. As explored in more detail in the subsequent sections, a motivating hypothesis (e.g., Cherian et al. 2021; Smyth et al. 2021) is that the spatiotemporal variability in the vertical shear in the upper ocean (which is defined more precisely later, but see Figs. 9 and 12c,d) is perhaps the most important driver of the day-to-day and spatial variability in DCT and  $\langle F_Q \rangle^{\max}$  (e.g., in Figs. 8b and 10). This vertical shear is strong on average above the equatorial undercurrent along the equator, but the shear is also highly variable and intermittently strong throughout the cold tongue (e.g., as shown in Fig. 9) due to a variety of interacting equatorial waves and instabilities (Moum et al. 2009; Inoue et al. 2012; Jing et al. 2014; Tanaka et al. 2015; Holmes and Thomas 2015, 2016; Inoue et al. 2019; Liu et al. 2019b,a; Pei et al. 2020; Liu et al. 2020; Cherian et al. 2021). Hence, strong DCT and  $\langle F_Q \rangle^{\max}$  vary in time and space and occur intermittently throughout the cold tongue (and at 3°N specifically) when the shear is strong. Over the next few sections, we explore the hypothesis that shear covaries with  $\langle F_Q \rangle^{\max}$  on and off the equator and more generally seek to identify covariates that provide information about  $\langle F_Q \rangle^{\max}$  without direct simulations or observations of turbulence.

### c. Shear, stratification, Richardson numbers, and the vertical extent of strong turbulence

Previous studies have identified the gradient Richardson number of the horizontally averaged profile  $\text{Ri}_g$  [defined in (1)] as an important indicator of the occurrence of DCT and strong ocean mixing in the equatorial Pacific (Pacanowski and Philander 1981; Peters et al. 1988; Large et al. 1994; Smyth and Moum 2013). Consistent with these previous studies, we find that Richardson numbers provide some useful information about the spatiotemporal structure and in particular the vertical extent of strong mixing in the LES and the TIWE observations. Below, we show that two Richardson numbers, both of which are based on the horizontally averaged velocity

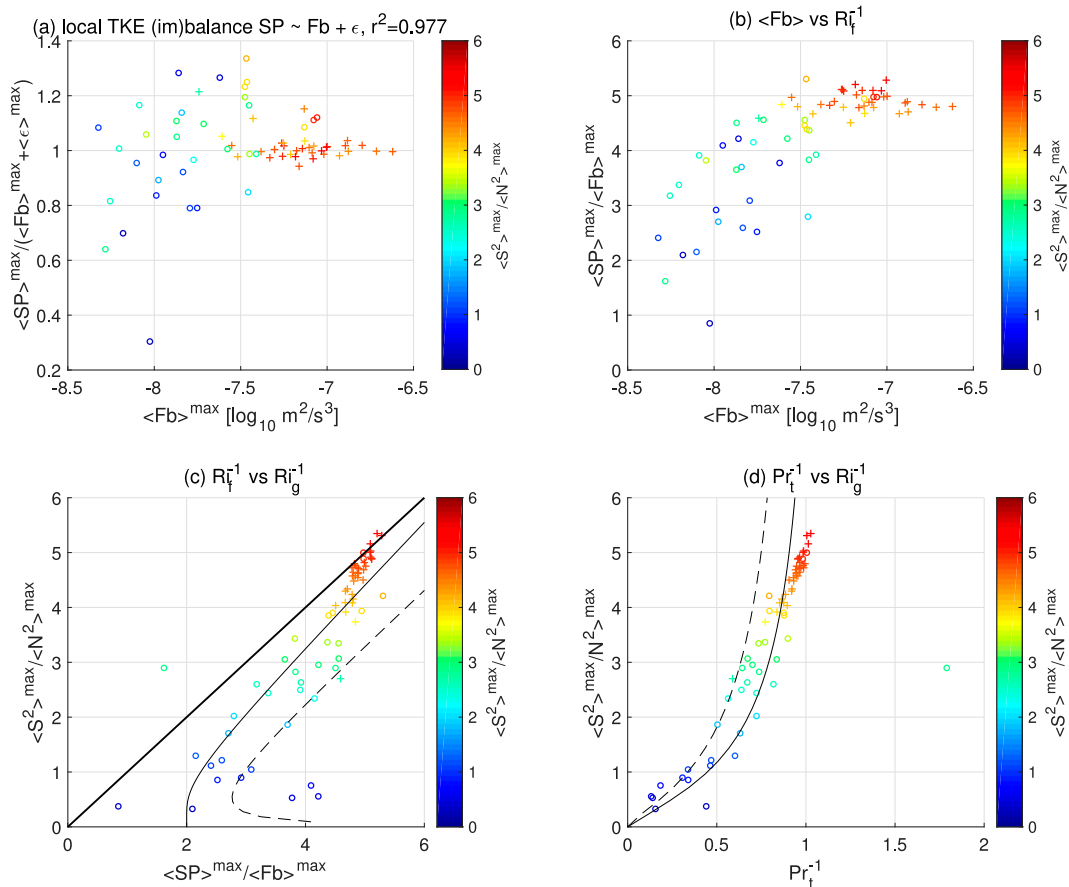


FIG. 15. Relationships between various terms in the daily mean turbulent kinetic energy budget at the depth  $z_{\max}$  where the downward turbulent buoyancy flux is maximum ( $\langle SP \rangle_{\max} + \langle T \rangle_{\max} \approx \langle F_b \rangle_{\max} + \langle \epsilon \rangle_{\max}$ ; see the appendix for details). The depths  $z_{\max}$  are plotted as + symbols in Fig. 10. Buoyancy flux  $\langle F_b \rangle_{\max}$  is plotted against (a) shear production over buoyancy flux plus dissipation  $\langle SP \rangle_{\max} / (\langle F_b \rangle_{\max} + \langle \epsilon \rangle_{\max})$  and (b) shear production over buoyancy flux (i.e., the inverse flux Richardson number  $Ri_f^{-1} = \langle SP \rangle_{\max} / \langle F_b \rangle_{\max}$ ). The inverse gradient Richardson number of the horizontally averaged profile  $Ri_g^{-1} = \langle S^2 \rangle_{\max} / \langle N^2 \rangle_{\max}$  is shown in color on all four panels and on the y axes against (c)  $Ri_f^{-1}$  and (d)  $Pr_t^{-1} = Ri_f / Ri_g$  (the inverse turbulent Prandtl number  $Pr_t^{-1}$  is the ratio of the turbulent diffusivity of buoyancy over the turbulent viscosity of momentum). The thick black line in (c) is the 1–1 line, the thin solid line is a fit to LES of a coastal boundary layer under a hurricane by Watkins and Whitt (2020), and the thin dashed line is a fit to atmospheric boundary layer observations by Anderson (2009), which parameterizes the subgrid-scale  $Pr_t^{-1}$  in the LES. The two days with most anomalously low  $Ri_f^{-1}$  [in (b) and (c):  $Ri_f^{-1} = 0.9$  and  $1.6$ ] and high  $Pr_t^{-1}$  [in (d):  $Pr_t^{-1} = 0.4$  and  $1.8$ ] also have the largest relative nonlocal sources of turbulent kinetic energy  $\langle T \rangle_{\max} / (\langle F_b \rangle_{\max} + \langle \epsilon \rangle_{\max}) \approx 1 - \langle SP \rangle_{\max} / (\langle F_b \rangle_{\max} + \langle \epsilon \rangle_{\max})$  [i.e., the points with lowest values in (a); 0.3 and 0.6]. Plus (+) symbols are from LES at  $0^\circ$  and circles (o) from  $3^\circ\text{N}$ .

and density profiles, can be used to model the depth  $z_{\max}$  where daily mean turbulent vertical heat fluxes  $\langle F_Q \rangle$  are maximum as well as the daily maximum depth  $z_{\text{pen}}$  to which strong turbulence penetrates. We define  $z_{\text{pen}}$  based on a constant threshold in the dissipation rate of turbulent kinetic energy  $\epsilon$ . It is reasonably straightforward to identify a depth  $z_{\text{pen}}$  from inspection of time–depth series of  $\epsilon$  or  $F_Q$  profiles (as in the midlatitudes, see Brainerd and Gregg 1995). After brief trial and error, we identify the shallowest depth where  $\epsilon < 2 \times 10^{-8} \text{ m}^2 \text{ s}^{-3}$  to be a useful threshold applicable to both of the LES (Figs. 11–13) and the TIWE observations. For reference, this  $\epsilon$  threshold corresponds to a turbulent heat flux of roughly  $7 \text{ W m}^{-2}$ , which is an order of magnitude smaller

than typical  $\langle F_Q \rangle_{\max}$  and about two orders of magnitude smaller than peak nighttime heat fluxes  $F_Q$  during turbulent bursts.

The depth  $z_{\max}$  varies from about 10 to 70 m at  $0^\circ$  and from 20 to 60 m at  $3^\circ\text{N}$  over time scales ranging from days to weeks (black plus symbols in Fig. 10; see also Fig. 8f). The occurrence of  $z_{\max}$  deeper than the nighttime MLD is hypothesized to be an indicator of DCT and strong heat fluxes. Consistent with this suggestion, the nighttime maximum MLD is shallower than  $z_{\max}$  at  $0^\circ$  on 29 of 34 days and 9 m shallower on average, but the nighttime MLD is deeper than  $z_{\max}$  at  $3^\circ\text{N}$  on 32 of 34 days and 9 m deeper on average. Qualitatively, we interpret these results as an indication that DCT occurs about

85% of the time at 0°N and about 5% of the time at 3°N, but there is not a one-to-one correspondence between DCT and  $z_{\max}$  deeper than MLD as demonstrated on 3–4 November at 0°, 140°W in Fig. 11. Although the nighttime maximum MLD is somewhat correlated with the depth  $z_{\max}$ , the relationship is in fact fairly scattered and the nighttime MLD can only explain about 30% of the variance in  $z_{\max}$  across both LES. On the other hand, about half of the simulated variance in the depth  $z_{\max}$  can be explained by  $H_{\text{Rib}}$  ( $r^2 = 0.5$ ), the depth at which the mean-profile bulk Richardson number  $\text{Ri}_b = 0.2$ . Here,

$$\text{Ri}_b = \frac{\Delta b H_{\text{Rib}}}{\Delta u^2 + v_t^2}, \tag{5}$$

where  $\Delta b$  and  $\Delta u$  are the bulk buoyancy and velocity differences between the depth  $H_{\text{Rib}}$  and the top  $0.1H_{\text{Rib}}$ ,  $v_t$  is a turbulent velocity scale that depends on the surface forcing as in Large et al. (1994), and the depth  $H_{\text{Rib}}$  is identified iteratively using the default parameters of Large et al. (1994) in an implementation of KPP by Smyth et al. (2002) (Fig. 14a). The inclusion of  $v_t$  in  $\text{Ri}_b$  systematically deepens  $H_{\text{Rib}}$  by 6 m on average, but has marginal and probably insignificant benefit on the best linear model or correlation with  $z_{\max}$  (increasing  $r^2$  by 15%). The specific threshold  $\text{Ri}_b = 0.2$  was chosen via trial and error. Larger and smaller thresholds for  $\text{Ri}_b$  were not as useful for identifying  $z_{\max}$ , but there may be room for future refinement of the model for  $z_{\max}$ , because half of the variance in  $z_{\max}$  is not explained by  $H_{\text{Rib}}$ .

The deepest depth to which DCT penetrates each day  $z_{\text{pen}}$  also varies significantly from about 40 to 90 m at 0° and from about 35 to 85 m at 3°N (Fig. 10). And again, the Richardson number—in this case the local gradient Richardson number  $\text{Ri}_g$  of the horizontally averaged profiles—provides useful information about  $z_{\text{pen}}$  each day. In particular, we define  $H_{\text{Rig}}$  as the base of the deep-cycle layer, which is defined by a low-gradient Richardson number  $\text{Ri}_g < 0.35$ . In practical applications (e.g., to the TIWE data),  $\text{Ri}_g$  is noisy and the definition of  $H_{\text{Rig}}$  requires some additional logic and filtering. In particular, the deep-cycle layer is defined by applying a rectangular filter of about 35 h and 35-m depth to a logical field that equals one where  $\text{Ri}_g < 0.35$  and the depth is below the daily maximum  $H_{\text{Rib}}$ . The second threshold based on  $H_{\text{Rib}}$  is necessary because  $\text{Ri}_g$  sometimes rises to high values within the weakly stratified turbulent boundary layer above  $H_{\text{Rib}}$ , particularly at 3°N and even fairly deep within  $H_{\text{Rib}}$  during nighttime (Figs. 12e,f). With regard to  $\text{Ri}_g$ , a threshold  $\text{Ri}_g = 0.25$  has a theoretical basis that makes it appealing (Miles 1961; Howard 1961; Holt et al. 1992; Rohr et al. 1988), and  $\text{Ri}_g = 0.25$  has been used previously for identifying the base of the deep-cycle layer in observations at 0°, 140°W (Lien et al. 1995; Smyth et al. 2021). However, we found via trial and error that a somewhat larger threshold  $\text{Ri}_g = 0.35$  is more useful across the LES at 0° and 3°N as well as the TIWE observations. Our approach is also supported by the LES of Pham et al. (2017), in which simulated turbulent bursts penetrate below the layer defined by a threshold  $\text{Ri}_g = 0.25$  in DCT as in our LES. A linear regression on  $H_{\text{Rig}}$ ,  $-6 + 1.1H_{\text{Rig}}$  has slope near one,

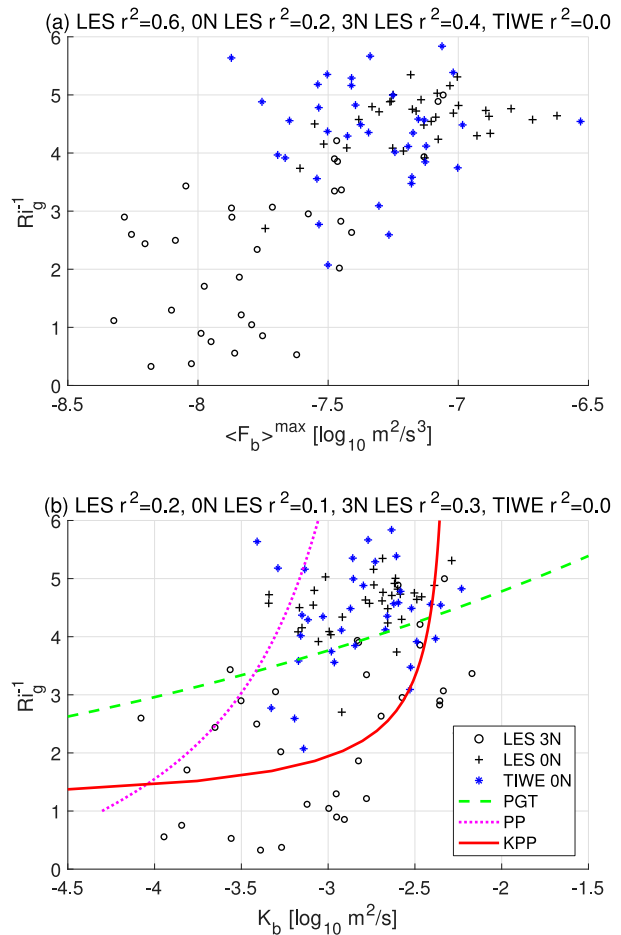


FIG. 16. Relationship between  $\text{Ri}_g^{-1} = \langle S^2 \rangle^{\max} / \langle N^2 \rangle^{\max}$  and (a)  $\langle F_b \rangle^{\max}$  and (b)  $K_b = \langle F_b \rangle^{\max} / \langle N^2 \rangle^{\max}$  at  $z_{\max}$  (i.e., at the depths indicated by the + symbols in Fig. 10). Averaging diffusivity directly in (b) yields quantitatively different results but qualitatively the same conclusion that  $K_b$  is at best weakly related to  $\text{Ri}_g$ . Overlaid in (b) are parameterizations of turbulent diffusivity as a function of Richardson number from Pacanowski and Philander (1981) (PP) Peters et al. (1988) (PGT), and Large and Gent (1999) (KPP).

intercept near zero, and explains 80% of the variance in the daily maximum  $z_{\text{pen}}$  (see Fig. 14b).

Finally, it may be noted that these relationships between  $z_{\max}$ ,  $H_{\text{Rib}}$ ,  $z_{\text{pen}}$ , and  $H_{\text{Rig}}$  are useful beyond the LES. For example, the TIWE observations reveal similar variability and relationships between  $z_{\max}$ ,  $H_{\text{Rib}}$ ,  $z_{\text{pen}}$ , and  $H_{\text{Rig}}$  as the LES at 0° (cf. blue stars and black + symbols in Figs. 14a,b). And,  $H_{\text{Rig}}$  is also a useful lower boundary for the deep-cycle layer in the MITgcm regional model with DCT parameterized by KPP (section 3), but the threshold has to be increased to  $\text{Ri}_g = 0.5$  (Cherian et al. 2021).

d. (Non)local energetics of  $\langle F_b \rangle^{\max}$

To begin to understand why the intensity of  $\langle F_b \rangle^{\max}$  (and by extension  $\langle F_Q \rangle^{\max}$ ) varies in time and space, it is useful to consider these variations in the context of the daily mean turbulent

kinetic energy budget under the premise that some of the variability in  $\langle F_b \rangle^{\max}$  is related to variations in the kinetic energy available to drive turbulent mixing (see the [appendix](#) for details). In this kinetic energy budget, the tendency or rate of change of turbulent kinetic energy is driven by vertical transport  $\langle T \rangle^{\max}$ , shear production  $\langle \text{SP} \rangle^{\max} = \langle \mathbf{F}_m \cdot \partial \mathbf{u}_f / \partial z \rangle^{\max}$ , dissipation  $\langle \epsilon \rangle^{\max}$ , and buoyancy flux  $\langle F_b \rangle^{\max}$  (Figs. 15a,b). Integrated over a full day, the budget is dominated by a net source due to shear production and net sinks due to buoyancy flux and dissipation at  $z_{\max}$ . That is, all other terms (tendency and vertical transport) are subdominant in all but one day and contribute less than 20% of the energy for dissipation and buoyancy flux  $\langle \epsilon \rangle^{\max} + \langle F_b \rangle^{\max}$  when mixing is strong (roughly  $\langle F_b \rangle^{\max} > 10^{-7.5} \text{ m}^2 \text{ s}^{-3}$ ; see Fig. 15a). Hence, the shear production of turbulent kinetic energy at  $z_{\max}$   $\langle \text{SP} \rangle^{\max}$  is highly correlated with  $\langle \epsilon \rangle^{\max} + \langle F_b \rangle^{\max}$  ( $r^2 = 0.98$ ; Fig. 15a). In addition, when mixing is strong,  $\langle F_b \rangle^{\max}$  is in approximately constant proportion to  $\langle \text{SP} \rangle^{\max}$  (about 0.2) and to  $\langle \epsilon \rangle^{\max}$  (about 0.25) (Figs. 15a,b). When the buoyancy flux is weaker  $\langle F_b \rangle^{\max} < 10^{-7.5} \text{ m}^2 \text{ s}^{-3}$ , the ratio  $\text{Ri}_f^{-1} = \langle \text{SP} \rangle^{\max} / \langle F_b \rangle^{\max}$  declines from 5 to 2 as  $\text{Ri}_g^{-1} = \langle S^2 \rangle^{\max} / \langle N^2 \rangle^{\max}$  decreases from 5 to 0.5 and  $\langle F_b \rangle^{\max}$  weakens to  $10^{-8.5} \text{ m}^2 \text{ s}^{-3}$  (Figs. 15b,c). Here,  $\text{Ri}_f$  is the flux Richardson number (e.g., [Osborn 1980](#); [Venayagamoorthy and Koseff 2016](#)). In addition, the relationship between  $\text{Ri}_f^{-1}$  and  $\text{Ri}_g^{-1}$  is associated with a relationship between  $\text{Ri}_g^{-1}$  and the turbulent Prandtl number  $\text{Pr}_t^{-1} = \text{Ri}_f / \text{Ri}_g$ , which quantifies how the turbulent diffusivity of buoyancy declines relative to the turbulent viscosity as  $\text{Ri}_g^{-1}$  decreases (Fig. 15d). Finally, it is notable that the turbulent kinetic energy budget contains significant nonlocal (transport) contributions at low  $\langle F_b \rangle^{\max} < 10^{-7.5} \text{ m}^2 \text{ s}^{-3}$ . In particular, transport  $\langle T \rangle^{\max} \approx \langle F_b \rangle^{\max} + \langle \epsilon \rangle^{\max} - \langle \text{SP} \rangle^{\max}$  becomes a more significant and scattered contributor to the dissipation and buoyancy flux, as  $\langle T \rangle^{\max} / (\langle F_b \rangle^{\max} + \langle \epsilon \rangle^{\max})$  reaches values of 40% and takes both signs (Fig. 15a).

In summary, when mixing is strong ( $\langle F_b \rangle^{\max} > 10^{-7.5} \text{ m}^2 \text{ s}^{-3}$ ), the energetics are dominantly local to the depth  $z_{\max}$  with shear production balanced by dissipation plus buoyancy flux and nearly constant  $\text{Ri}_f \approx 0.2$  and  $\text{Ri}_g \approx 0.25$  both on and off the equator. However, the energetics of  $\langle F_b \rangle^{\max}$  in general (including weaker values) are more complex: the energetics are approximately local on average, but nonlocal (transport) contributes 10%–40% to the energetics on many days and takes both signs. In addition,  $\text{Ri}_f$  systematically varies with  $\text{Ri}_g$ , both of which take values substantially higher than the canonical values ( $\text{Ri}_f \approx 0.2$  and  $\text{Ri}_g \approx 0.25$ ) on most days at  $3^\circ\text{N}$ . At  $0^\circ$ , the canonical DCT and local dynamics are the norm, but at  $3^\circ\text{N}$  the canonical DCT and local dynamics are the exception rather than the norm. The simulated energetic relationships encapsulated in relationships between  $\text{Ri}_f$ ,  $\text{Pr}_t$ , and  $\text{Ri}_g$  (Figs. 15c,d) are qualitatively consistent with observations in the atmospheric boundary layer ([Anderson 2009](#)), a previous LES of ocean turbulence under a hurricane in the coastal midlatitudes reported by [Watkins and Whitt \(2020\)](#), and direct numerical simulations ([Venayagamoorthy and Koseff 2016](#)). However, it still remains somewhat uncertain whether the relationships modeled here in the LES are in any sense universal, especially given the significance of nonlocal (transport) dynamics at weak  $\langle F_b \rangle^{\max}$ .

### e. Scaling $\langle F_b \rangle^{\max}$ based on the horizontally averaged velocity and buoyancy profiles

Building on the result that  $\langle F_b \rangle^{\max}$  varies in concert with other metrics of the turbulence energetics such as the shear production and dissipation rate, this section demonstrates how the intensity of  $\langle F_b \rangle^{\max}$  (and by extension  $\langle F_Q \rangle^{\max}$ ) covaries with readily measured or simulated non-turbulent variables such as horizontally averaged velocity and buoyancy profiles as well as the surface momentum and buoyancy fluxes. In a second step, we evaluate scaled predictions of  $\langle F_b \rangle^{\max}$  derived from the LES results by applying the scaling to the independent TIWE observations.

We begin by quantifying the relationship between the mean profile  $\text{Ri}_g$  and the intensity of mixing at  $z_{\max}$  motivated by popular existing parameterizations of the local intensity of turbulent diffusion as a function of  $\text{Ri}_g$  ([Pacanowski and Philander 1981](#); [Peters et al. 1988](#); [Large et al. 1994](#)). We find that the simulated inverse Richardson number  $\text{Ri}_g^{-1}$  at  $z_{\max}$  can explain most of the simulated variability in  $\langle F_b \rangle^{\max}$  across the LES at both  $0^\circ$  and  $3^\circ\text{N}$  [Fig. 16a;  $r^2 = 0.6$  for the regression  $\log_{10}(\langle F_b \rangle^{\max}) \sim \langle S^2 \rangle^{\max} / \langle N^2 \rangle^{\max}$ ]. On the other hand,  $\text{Ri}_g^{-1}$  on its own does not explain the temporal variability in  $\langle F_b \rangle^{\max}$  very well at  $0^\circ$  in either the LES ( $r^2 = 0.2$ ) or the TIWE observations ( $r^2 = 0.0$ ). These results are consistent with the hypothesis that  $\text{Ri}_g$  is a useful predictor of the intensity of mixing across a range of  $\text{Ri}_g$  that includes marginal instability ( $1 \geq \text{Ri}_g \geq 0.25$ , as at  $3^\circ\text{N}$ ) but a poor predictor of the intensity of mixing when marginal instability is either persistent ( $\text{Ri}_g \approx 0.25$ , as at  $0^\circ\text{N}$ ) or marginal instability never occurs and  $\text{Ri}_g > 1$  is always very large (for background on marginal instability, see [Thorpe and Liu 2009](#); [Smyth and Moum 2013](#); [Smyth 2020](#)). For better comparison with previous studies, we also show that variations in the effective turbulent diffusivity of buoyancy at  $z_{\max}$  ( $K_b = \langle F_b \rangle^{\max} / \langle N^2 \rangle^{\max}$ ) are more weakly correlated with  $\text{Ri}_g^{-1}$  [ $r^2 = 0.2$  for  $\log_{10}(K_b) \sim \langle S^2 \rangle^{\max} / \langle N^2 \rangle^{\max}$  in LES;  $r^2 = 0.0$  in TIWE] and thus not well explained by  $\text{Ri}_g^{-1}$  (Fig. 16b) or  $\text{Ri}_g$ -based parameterizations ([Pacanowski and Philander 1981](#); [Peters et al. 1988](#); [Large et al. 1994](#)). However, it may be noted that the underlying variables in the regressions for  $K_b$  and  $\langle F_b \rangle^{\max}$  are actually the same,  $\langle S^2 \rangle^{\max}$ ,  $\langle N^2 \rangle^{\max}$ , and  $\langle F_b \rangle^{\max}$ , which suggests that the relatively poor correlation between  $\log_{10}(K_b)$  and  $\text{Ri}_g^{-1}$  may be improved by simply reformulating the predictor function of  $\langle S^2 \rangle^{\max}$  and  $\langle N^2 \rangle^{\max}$ . Indeed, a general two-variable linear regression of  $\log_{10} K_b$  on  $\log_{10} \langle S^2 \rangle^{\max}$  and  $\log_{10} \langle N^2 \rangle^{\max}$  yields an  $r^2 = 0.6$  for  $\log_{10}(K_b) \sim \log_{10}[\langle S^2 \rangle^{\max} (\langle N^2 \rangle^{\max})^{-3/2}]$ . In summary, although the LES yield results that are loosely consistent with previous studies (e.g., Fig. 16b), there is significant room to improve parameterizations of ocean mixing in the cold tongue. That is,  $\text{Ri}_g$  is useful but certainly not sufficient to explain all of the spatio-temporal variability in  $\langle \epsilon \rangle^{\max}$  or  $\langle F_b \rangle^{\max}$  in the eastern equatorial Pacific ([Moum et al. 1989](#); [Zaron and Moum 2009](#)). Other variables and combinations of variables likely contain valuable information about  $\langle F_b \rangle^{\max}$  in DCT and in general across the cold tongue.

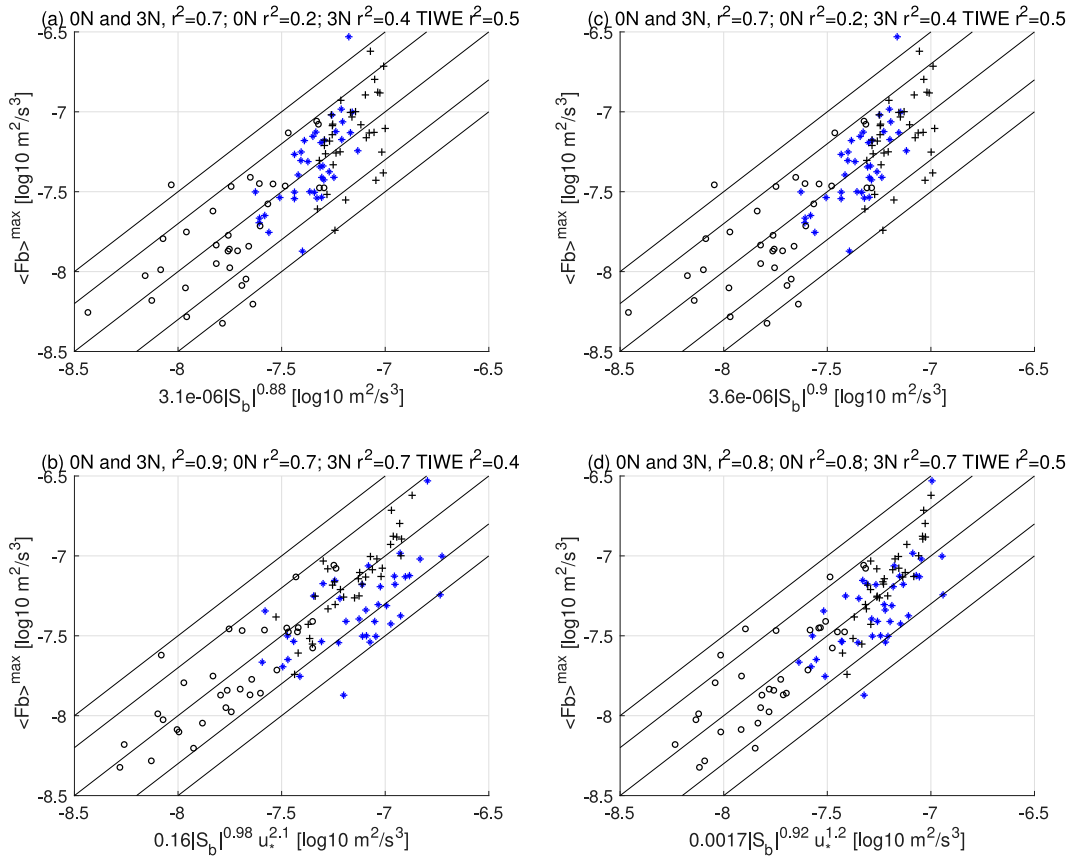


FIG. 17. Maximum daily mean turbulent buoyancy flux  $\langle F_b \rangle^{\max}$  scales with (a),(c) oceanic bulk vertical shear  $S_b$  and (b),(d) even more closely with a product of  $S_b$  and the magnitude of the surface wind stress  $|\tau|=u_*^2\rho$ . The scalings are obtained via linear regression on the LES output in (a) and (b), which includes 34 days at 3°N (black open circles) and 34 days at 0°N (black +), or on the 68 days of LES output plus 38 days of TIWE data (blue asterisks) in (c) and (d). Hence, the TIWE observations serve as an independent validation of the regressions in (a) and (b) and constrain the regressions in (c) and (d). The predictors include  $S_b$ , which is derived from a linear fit to the mean velocity from  $H_{\text{Rig}}$  to 5-m depth (thick black lines in Fig. 4), and the friction velocity  $u_* = \sqrt{|\tau|/\rho}$ . All variables are log-transformed and Pearson's  $r$  in the panel titles is calculated in log space. The various diagonal black lines indicate where the data are along the 1–1 line, within a factor of 2, and within a factor of 3. With 95% confidence intervals, the scalings are as follows:  $(2\text{--}6) \times 10^{-6} |S_b|^{(0.7\text{--}1.0)}$  in (a),  $(1\text{--}200) \times 10^{-2} |S_b|^{(0.9\text{--}1.1)} u_*^{(1.6\text{--}2.5)}$  in (b),  $(2\text{--}6) \times 10^{-6} |S_b|^{(0.8\text{--}1.0)}$  in (c), and  $(0.03\text{--}1.3) \times 10^{-2} |S_b|^{(0.8\text{--}1.0)} u_*^{(0.9\text{--}1.6)}$  in (d).

In an attempt to refine our understanding of the mean-profile properties that drive temporal variations in  $\langle F_Q \rangle^{\max} \sim \langle F_b \rangle^{\max}$ , we conduct a more general multivariable linear regression analysis with the aim of identifying an optimal power law product (e.g., a product of the generic form  $c x^a y^b z^d \dots$ , with variables  $x, y, z, \dots$  and constants  $a, b, c, d, \dots$  to be determined) to model the maximum buoyancy flux  $\langle F_b \rangle^{\max}$  as a function of horizontally averaged and readily measured (and modeled) properties, including surface fluxes and the horizontally averaged profiles of velocity and density but without a priori knowledge of the depth  $z_{\text{max}}$  at which  $\langle F_b \rangle^{\max}$  occurs. Although a formulation as a power law may seem arbitrary, this choice is motivated by two factors. First, many familiar mixing models are expressed as a product of terms (e.g., a diffusivity times a gradient, or a mixing efficiency times a momentum flux times a shear; e.g., Fig. 16b) and are therefore power laws. In addition,  $\langle F_b \rangle^{\max}$  is thought to be

logarithmically distributed (see section 3d and Fig. 8), and power laws are readily amenable to linear regression after applying a log transform.

Numerous variables were considered in the regressions, but we only highlight two low-complexity models that we identified. First, the most useful variable that we identified for modeling the combined LES output from 0° to 3°N is the vertical shear  $S_b$ . In particular, if  $S_b$  is a bulk shear defined by a least squares linear fit to the daily mean and horizontally averaged velocity profile from  $H_{\text{Rig}}$  to 5-m depth, then we find that  $S_b$  alone can explain about 70% of the daily variance in  $\langle F_b \rangle^{\max}$  from both the LES at 0° and 3°N (Fig. 17a;  $\langle F_b \rangle^{\max} \approx 3.1 \times 10^{-6} |S_b|^{0.88}$ ;  $r^2 = 0.7$  in log<sub>10</sub> space ignoring the TIWE data). In an encouraging result, independent validation of the  $S_b$  scaling of  $\langle F_b \rangle^{\max}$  on the TIWE data is quite good ( $r^2 = 0.5$  with little mean bias) and even better than the LES at 0°N

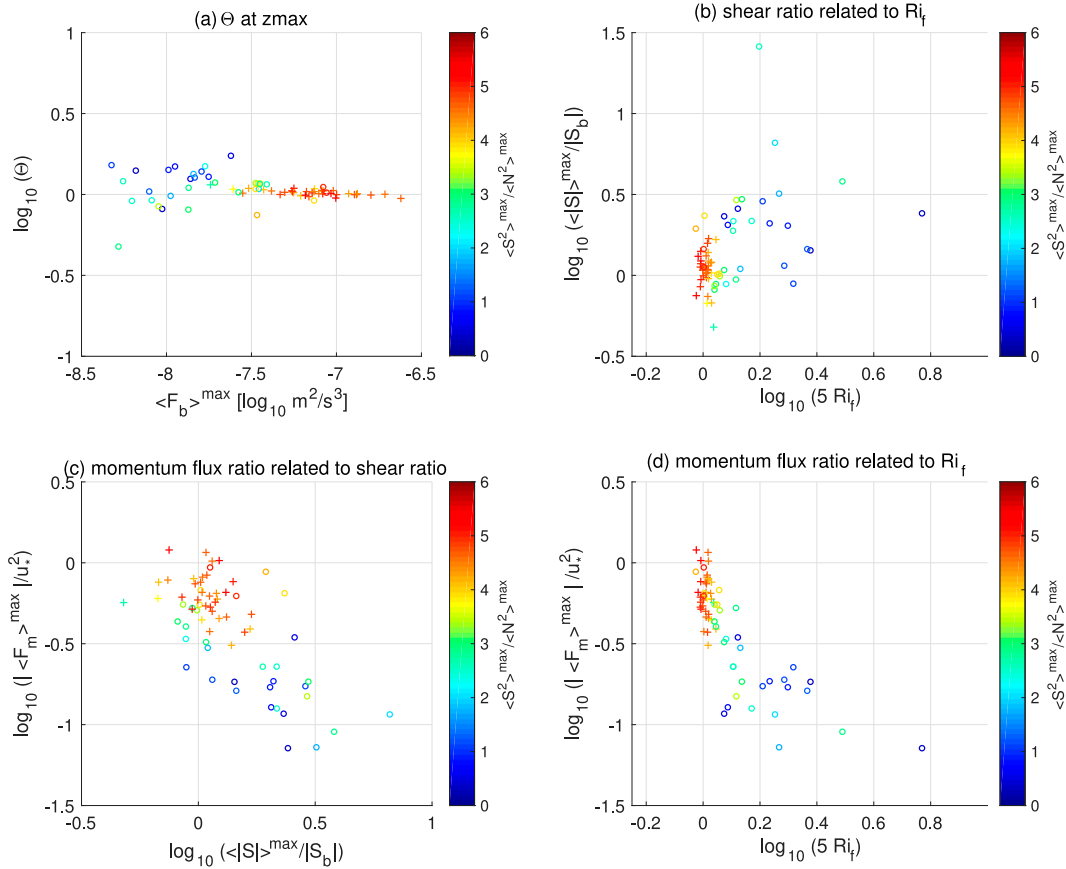


FIG. 18. Various ratios of terms in Eq. (6) showing how the local energetics of the buoyancy flux at  $z_{\max}$  (Fig. 15) relate to the bulk scalings derived via regression (Fig. 17). Circles ( $\circ$ ) are from the LES at  $3^\circ\text{N}$ , and pluses ( $+$ ) are from the LES at  $0^\circ$ ; the color indicates  $\text{Ri}_g^{-1} = \langle S^2 \rangle_{\max} / \langle N^2 \rangle_{\max}$ .

alone ( $r^2 = 0.2$ ). In addition, including the TIWE data in the regression in Fig. 17c has little impact on the optimal linear model, which seems fairly robust with relatively narrow confidence intervals on the parameters (cf. Figs. 17a,c). However, the model fit to the LES  $\langle F_b \rangle_{\max}$  can be improved substantially by adding the surface friction velocity due to the wind stress  $u_* = \sqrt{|\boldsymbol{\tau}|/\rho}$  as a variable ( $\boldsymbol{\tau}$  is the wind stress vector). The optimal linear model based on these two variables  $\langle F_b \rangle_{\max} \approx 0.16|S_b|^{0.98}u_*^{2.05}$  explains about 90% of the LES variance and 70% at  $0^\circ$  or  $3^\circ\text{N}$  alone (Fig. 17b). In independent validation on the TIWE data, the two-variable model explains only 40% of the TIWE variance and also has a slight mean bias (Fig. 17b). Including the TIWE observations in the two-variable regression in Fig. 17d leads to a fairly substantial change in the optimal two-variable model  $0.0017|S_b|^{0.92}u_*^{1.2}$  and somewhat reduces the correlation at  $3^\circ\text{N}$  in the LES but reduces the mean bias in the TIWE data and slightly improves the corresponding correlation (cf. Figs. 17b,d). These results suggest that although wind stress certainly provides useful information about  $\langle F_b \rangle_{\max}$ , the available data (including 108 days spanned by the LES and TIWE) is only marginally sufficient to provide a robust linear model based on both  $S_b$  and  $u_*$ .

For reference, the 95% confidence intervals for various optimal power laws stated in the previous paragraph and obtained via regression are given in the caption of Fig. 17. Consistent with the above discussion, only the power on  $S_b$  is tightly constrained to be within 0.7 and 1.1. There is substantial joint uncertainty in the power on  $u_*$  (which may range from 0.9 to 2.5) and the magnitude of the constant coefficient (which may range from  $3 \times 10^{-4}$  to 2). The coefficient, which in general has units, is smaller if the power on  $u_*$  is lower, and conversely the coefficient is larger if the power on  $u_*$  is larger. Assuming a fixed relationship  $\langle F_b \rangle_{\max} \sim u_*^2 S_b$  and regressing  $\langle F_b \rangle_{\max}$  on  $u_*^2 S_b$  (the exponents of which yield an appealingly unitless coefficient) yields 95% confidence intervals on the slope of 0.15–0.19, an intercept indistinguishable from zero, and  $r^2 = 0.82$ . Applying  $\log_{10}$  to both sides before regressing puts more weight on accuracy at weaker  $\langle F_b \rangle_{\max}$  and yields confidence intervals on the intercept of  $[-1.63, -0.33]$ , which corresponds to a coefficient ranging from 0.02 to 0.47 in the power law. Either way, it seems that  $\langle F_b \rangle_{\max} \approx 0.2u_*^2 S_b$  is a plausible model with roughly a factor of 3 uncertainty. Although many other variables were considered, we found at best marginal improvements in the correlations (e.g., when

adding a measure of stratification and/or the net surface buoyancy flux to create multivariate linear regressions) and many lower correlations if shear and/or wind stress is omitted or the definition of the shear is changed. Hence, we do not report any further results of our statistical modeling.

*f. Discussion of the empirical power law scaling of  $\langle F_b \rangle^{\max}$  in light of prior results*

In the context of DCT on the equator, it is neither surprising nor novel that shear and wind stress are correlated with the intensity of mixing. Several previous studies have identified such relationships using observations and theory (Moum and Caldwell 1985; Pham et al. 2017; Smyth et al. 2017, 2021). In addition, we reanalyzed the results from the LES of Wang et al. (1998) (see also Large and Gent 1999), nominally at  $0^\circ$ ,  $140^\circ\text{W}$ , and found that those results are consistent with the  $\langle F_b \rangle^{\max} \sim 0.2u_*^2 S_b$  scaling identified empirically here to the degree that it is reasonable to make claims of consistency, which is only within a factor of 3. However, the application of such a relation beyond  $0^\circ$ ,  $140^\circ\text{W}$  and in situations without DCT as well as the precise formulation of the statistical models proposed in section 4e and Fig. 17 are new and somewhat unintuitive in light of the energetics of  $\langle F_b \rangle^{\max}$ , which indicate dominantly local dynamics remote from the surface forcing. Hence, we find it useful to see how the empirical scalings in section 4e relate to the turbulent energetics discussed in section 4d. In addition, we briefly discuss how the scalings relate to a theory previously developed by Smyth et al. (2017) to model DCT at  $0^\circ$ ,  $140^\circ\text{W}$  and compare the results from LES with analogous results derived from the KPP scheme (Large et al. 1994) in the parent ocean model ROMS.

To reveal how the energetics at  $z_{\max}$  (e.g., Fig. 15) relates to the scaling derived via linear regression and shown in Fig. 17b, we write

$$\frac{\langle F_b \rangle^{\max}}{0.2u_*^2 |S_b|} = \frac{\text{Ri}_f \Theta \langle \mathbf{F}_m \rangle^{\max} | \langle S \rangle^{\max} |}{0.2 u_*^2 |S_b|}, \quad (6)$$

and quantify how the local turbulent momentum flux  $\langle \mathbf{F}_m \rangle^{\max}$  and vertical shear  $\langle S \rangle^{\max}$  at  $z_{\max}$  relate to the bulk shear  $S_b$  and friction velocity squared  $u_*^2$  in the scaling. Here,  $\text{Ri}_f = \langle F_b \rangle^{\max} / \langle \text{SP} \rangle^{\max}$  is the flux Richardson number at  $z_{\max}$ ,  $\langle \text{SP} \rangle = \langle \mathbf{F}_m \cdot \partial \mathbf{u}_h / \partial z \rangle$  is the daily mean shear production, and  $\Theta = \langle \mathbf{F}_m \cdot \partial \mathbf{u}_h / \partial z \rangle^{\max} / (|\langle \mathbf{F}_m \rangle^{\max}| |\langle \partial \mathbf{u}_h / \partial z \rangle^{\max}|)$  is a dimensionless measure of the combined effects of misalignment and subdaily correlations between shear and momentum flux on shear production at  $z_{\max}$ . Various ratios of terms in this expression are plotted in Fig. 18. We interpret these results in two parts, focusing first on instances of strong mixing and DCT and then on instances of weaker mixing.

First, we recall that strong mixing (roughly  $\langle F_b \rangle^{\max} > 10^{-7.5} \text{ m}^2 \text{ s}^{-3}$ ) tends to be in a state of marginal instability with fairly uniform  $\text{Ri}_g^{-1} \approx 4$  (Fig. 15), i.e., only the yellow, orange, and red colored points are associated with strong mixing in Fig. 18. For these points, the ratios on the right side of (6) are fairly simple:  $\Theta \approx 1$  (Fig. 18a),  $\text{Ri}_f \approx 0.2$  (Figs. 18b,d),  $|\langle S \rangle^{\max}| / |S_b| \approx 1$  (Figs. 18b,c), and  $|\langle \mathbf{F}_m \rangle^{\max}| / u_*^2$  ranges from about 0.3 to 1.1 (Figs. 18c,d). That is, our empirical  $0.2u_*^2 |S_b|$  scaling derived via regression

can reasonably be interpreted as a proxy for local dynamics at  $z_{\max}$  with 0.2 a proxy for  $\text{Ri}_f$  at  $z_{\max}$ ,  $u_*^2$  a proxy for the momentum flux at  $z_{\max}$ , and  $|S_b|$  a proxy for the shear at  $z_{\max}$ .

In the presence of strong mixing and DCT at  $0^\circ$ ,  $140^\circ\text{W}$  ( $\langle F_b \rangle^{\max} > 10^{-7.5} \text{ m}^2 \text{ s}^{-3}$ ), the empirical  $0.2u_*^2 |S_b|$  scaling from the LES is also consistent with the theory of Smyth et al. (2017), which yields  $F_b \approx 0.2\epsilon$  where  $\epsilon \approx u_*^2 |S_b|$  in steady state. To briefly summarize Smyth et al. (2017), the theory explicitly models the shear and turbulent kinetic energy in the deep-cycle layer, which is defined to be a layer of thickness  $H$  with homogeneous shear  $S_b$  and turbulent kinetic energy  $k$  from the base of the mixed layer to the top of the undercurrent core. The shear  $S_b$  evolves due to changes in the surface mixed layer velocity, which in turn evolves due to any convergence between the downward momentum flux at the surface [ $u_*^2 = F_m(0)$ ] and the MLD [ $F_m(h)$  where  $h$  is the MLD]. The momentum flux is assumed to be dominated by the zonal component, which is about 3 times stronger than the meridional component at the surface in our LES at  $0^\circ$ ,  $140^\circ\text{W}$ . The turbulent kinetic energy  $k$  evolves in the theory due to shear production and dissipation plus buoyancy flux in the shear layer. That is,

$$\frac{\partial S_b}{\partial t} = \frac{1}{Hh} [u_*^2 - F_m(h)], \quad (7)$$

$$\frac{\partial k}{\partial t} = F_m S_b - \epsilon - F_b, \quad (8)$$

following their Eqs. (3.2) and (3.3). Closure of turbulent fluxes in terms of turbulent kinetic energy is discussed in Smyth et al. (2017). But, the expressions (7) and (8) suggest that if the shear  $S_b$  and turbulent kinetic energy  $k$  are in a steady state then  $F_m(h)/u_*^2 \approx 1$ , as in the strong DCT simulated by LES (Fig. 18). In addition,  $\epsilon + F_b \approx u_*^2 S_b$ . With the additional assumption that  $F_b/\text{SP} \approx 0.2$ , then  $F_b \approx 0.2u_*^2 S_b$ .

That is, the theory of Smyth et al. (2017) suggests essentially the same mathematical form as the empirical linear model derived from the LES, although the definition of  $S_b$  differs. In their theory,  $S_b$  is interpreted as an average over the deep cycle layer, from  $H_{\text{Rig}}$  to the daily maximum MLD, whereas in our empirical model  $S_b$  is fit to the velocity profile from  $H_{\text{Rig}}$  to 5-m depth. However, the different definitions of  $S_b$  turn out to have only a small impact on the prediction of  $\langle F_b \rangle^{\max}$  at  $0^\circ$  because the two definitions of  $S_b$  turn out to be highly correlated and similar in magnitude; both are also good proxies for the shear at  $z_{\max}$ . Hence,  $r^2$  is only reduced from 0.8 to 0.7 if  $S_b$  is calculated only in the deep cycle layer, i.e., from  $H_{\text{Rig}}$  to the deepest MLD during a given day rather than to 5 m if the data are restricted to the LES at  $0^\circ$ . This property of the velocity profile may contribute to the success of our empirical scaling in predicting  $\langle F_b \rangle^{\max}$  in the TIWE observations, in which we had to extrapolate the velocity profiles to the surface to define  $S_b$ , as well as the relative success of Smyth et al. (2021) in modeling  $\epsilon$  from  $\chi$  pods at  $0^\circ$  defining  $S_b$  as an average over the deep cycle layer.

So, why are we introducing a new definition of  $S_b$ ? The answer is that the new definition turns out to be crucial off

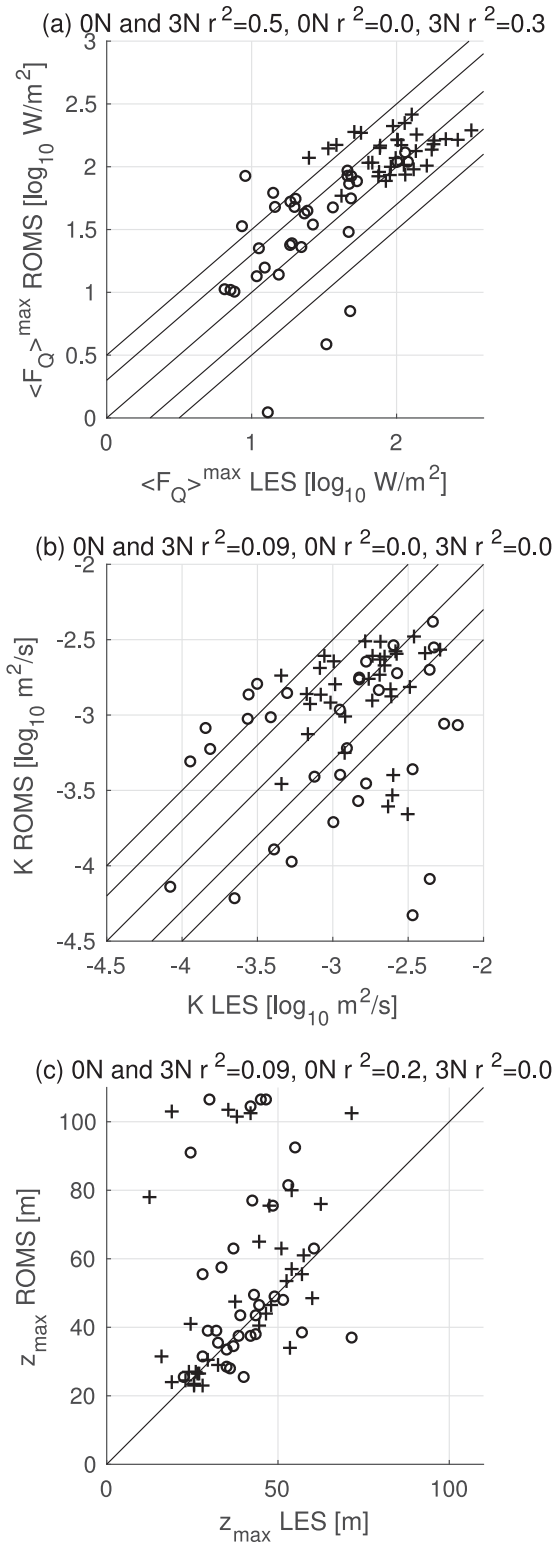


FIG. 19. Comparisons between the LES and ROMS (KPP) at the LES locations (+ at 0° and ○ at 3°N along 140°W): (a) the maximum turbulent heat flux  $\langle F_Q \rangle^{\max}$ , (b) the turbulent diffusivity of heat  $K$  at  $z_{\max}$ , and (c) the depth  $z_{\max}$  at which  $\langle F_Q \rangle^{\max}$  occurs. Note, however, that

the equator and in instances of weaker mixing ( $\langle F_b \rangle^{\max} < 10^{-7.5} \text{ m}^2 \text{ s}^{-3}$ ), as discussed in the next paragraph. However, there are also some practical advantages and disadvantages to the new definition. First, it is more difficult to observe ocean currents above 25 m, and hence more difficult to calculate our  $S_b$  with observations, although ADCPs on modern autonomous platforms (Shcherbina et al. 2019; Gentemann et al. 2020) and moored ADCPs (Masich et al. 2021) can sample to 10-m depth or less and current meters can be deployed at shallower depths on moorings to mitigate issues particular to upward looking ADCPs on moorings. On the other hand, it is advantageous to define  $S_b$  as we do for application in ocean model parameterizations, since it does not depend on the extra diagnosis and definition of the daily maximum MLD and our approach works even when the deep cycle layer has zero thickness.

However, the main motivation for the new definition of  $S_b$  is that it substantially improves the predictions of  $\langle F_b \rangle^{\max}$  off the equator at 3°N and when mixing is weak (roughly,  $\langle F_b \rangle^{\max} < 10^{-7.5} \text{ m}^2 \text{ s}^{-3}$ ). The reasons for this improvement are highlighted via the terms in (6): the LES results in Fig. 18 show that  $|\langle F_m \rangle^{\max}|/u_s^2$  and  $|\langle S \rangle^{\max}|/|S_b|$  deviate systematically from 1 and  $\langle F_b \rangle^{\max}/\langle SP \rangle^{\max}$  deviates systematically from 0.2 in many instances of weaker mixing at 3°N. In conjunction with these deviations,  $Ri_g^{-1} < 4$  deviates toward stability (i.e., points are colored blue to yellow in Fig. 18; see also Fig. 15). The deviation of  $|\langle S \rangle^{\max}|/|S_b|$  is indicative of a divergence between our bulk shear  $S_b$  and the shear in the deep cycle layer (used in the theory of Smyth et al. 2017), which has zero thickness on 3 out of 34 days at 3°N. A practical consequence of this divergence in  $|\langle S \rangle^{\max}|/|S_b|$  is that replacing  $S_b$  with the shear in the deep cycle layer in the linear model  $u_s^2 S_b$  leads to a reduction in the correlation from  $r^2 = 0.7$  to  $r^2 = 0.4$  when the data are from only the LES at 3°N. Specifically, these deviations indicate that the shear is more concentrated at the base of the mixed layer, the wind contributes more to accelerating the mixed layer than below, and the shear at the base of the mixed layer is weaker than necessary for marginal instability. All of these features are consistent with a transition to a midlatitude inertial regime when the shear, wind stress, and hence turbulent heat fluxes are sufficiently weak (e.g., Pollard and Millard 1970). In this regime, strong turbulent heat fluxes like those in strong equatorial DCT only occur intermittently under the right conditions, such as when the shear and wind are sufficiently strong and well aligned and the system is near a state of marginal instability (e.g., Pollard et al. 1972; Burchard and Rippeth 2009; Brannigan et al. 2013; Watkins and Whitt 2020). Yet, the scaling  $F_b \approx 0.2u_s^2 S_b$  in combination still approximately holds when mixing is weaker  $10^{-8.5} < \langle F_b \rangle^{\max} < 10^{-7.5} \text{ m}^2 \text{ s}^{-3}$  at 3°N. In addition, it is interesting to note that a reanalysis of the LES of Watkins and Whitt

←

the LES results are derived from the buoyancy dynamics whereas the ROMS results are derived from the temperature dynamics. That is, the LES results are  $(\rho c_p / g \alpha) F_b = 1.37 \times 10^9 \langle F_b \rangle \approx \langle F_Q \rangle$  ( $\text{W m}^{-2}$ ) in (a) and  $K = \langle F_b \rangle^{\max} / \langle N^2 \rangle^{\max}$  in (b), and  $z_{\max}$  is calculated from  $\langle F_b \rangle$  profiles.



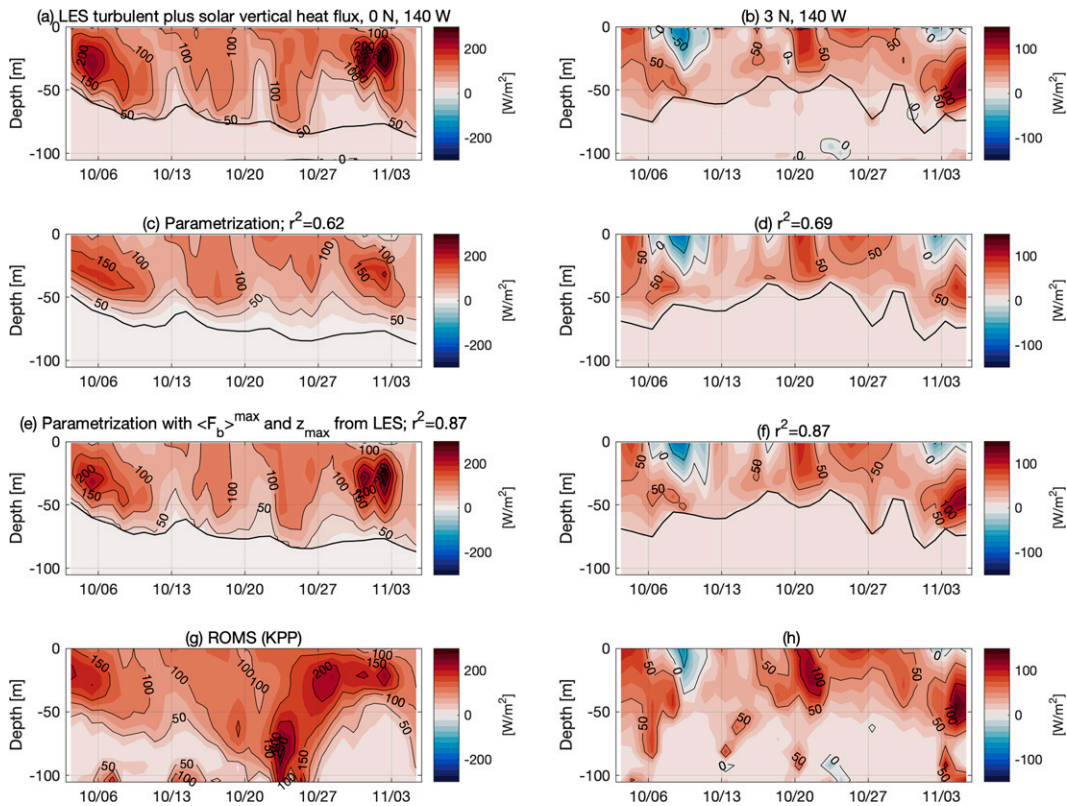


FIG. 20. Daily averaged net vertical heat flux  $\langle Q \rangle$  (including turbulent  $F_Q$  as in Fig. 10 plus penetrative radiative  $P_Q$  components) at (left)  $0^\circ$ ,  $140^\circ\text{W}$  and (right)  $3^\circ\text{N}$ ,  $140^\circ\text{W}$  (a),(b) as simulated by the LES and (c),(d) as parameterized based on horizontally averaged velocity and density profiles and net surface buoyancy and momentum fluxes. (e),(f) For reference, the piecewise linear flux profiles with  $\langle Q \rangle(z = 0)$  and  $\langle Q \rangle(z = z_{\max})$  from LES are shown. (g),(h) In addition, the vertical heat fluxes (penetrating shortwave plus turbulent) from the parent ROMS model are shown. Note the different color bar ranges in the left and right columns. For consistency with earlier results, (a) and (f) plot  $(\rho c_p / g \alpha) \langle B \rangle \approx \langle Q \rangle$ , where  $\langle B \rangle$  is the daily averaged vertical buoyancy flux, including the parts due to turbulence and penetrative shortwave radiation.

(2020) showed that  $F_b^{\max} \approx 0.2u_*^2 S_b$  within a factor of 3 in hurricane-driven entrainment in the coastal midlatitude ocean, from  $F_b^{\max} = 10^{-8}$  to  $10^{-5} \text{ m}^2 \text{ s}^{-3}$  without time averaging (only horizontal averaging). Analysis of the covariability of the ratios in (6) in Fig. 18 shows that the empirical  $F_b \approx 0.2u_*^2 S_b$  scaling continues to perform reasonably well for  $\langle F_b \rangle^{\max} < 10^{-7.5} \text{ m}^2 \text{ s}^{-3}$  at  $3^\circ\text{N}$  because the changes in the ratios  $\langle F_m \rangle^{\max} / u_*^2$ ,  $\langle |S| \rangle^{\max} / S_b$ , and  $R_{if}$  compensate for each other (Fig. 18). Thus, as the turbulence weakens such that  $\langle F_b \rangle^{\max} < 10^{-7.5} \text{ m}^2 \text{ s}^{-3}$ , it is more difficult to interpret the empirical scalings from section 4e as proxies for local dynamics at  $z_{\max}$  or using the theory for homogeneous DCT of Smyth et al. (2017). That is, the empirical scaling  $F_b \approx 0.2u_*^2 S_b$  can be explained by theory for DCT at  $0^\circ$ ,  $140^\circ\text{W}$  (Smyth et al. 2017), but the theory cannot explain the applicability of the scaling at  $3^\circ\text{N}$ ,  $140^\circ\text{W}$  in the LES.

A question that arises at this point is how the results from LES and the parameterization for  $\langle F_b \rangle^{\max}$  (and by extension  $\langle F_Q \rangle^{\max}$ ) compare with existing mixing parameterizations that are designed to be applicable both on and off the equator (unlike the theory of Smyth et al. 2017), such as the KPP

scheme (building on Figs. 7, 8, and 16b). Properly addressing this question is beyond the scope of this paper and a subject of interest for future work, but a comparison between the simulations of  $\rho c_p / (g \alpha) \langle F_b \rangle^{\max} \approx \langle F_Q \rangle^{\max}$  in the LES and  $\langle F_Q \rangle^{\max}$  in ROMS (KPP) highlights substantial differences despite the similar large-scale oceanic and atmospheric forcing. However, minor differences in these large-scale forcings mean that the comparisons should be treated as qualitative rather than quantitative (see section 4a and the appendix for further details). In any case, we find that the maximum of the daily averaged turbulent heat flux  $\langle F_Q \rangle^{\max}$  ranges over a similar set of values from about 10 to  $300 \text{ W m}^{-2}$  and the daily variability in the LES and ROMS is correlated in space and time at both  $0^\circ$  and  $3^\circ\text{N}$  ( $r^2 = 0.5$ ; see Fig. 19a). However, most of the correlation comes from  $3^\circ\text{N}$ , where  $r^2 = 0.3$ . There is no temporal correlation in  $\langle F_Q \rangle^{\max}$  between the LES and ROMS at  $0^\circ$ . The turbulent diffusivity at  $z_{\max}$  is more scattered than the heat flux with a marginally significant correlation across space and time, and no temporal correlation at either latitude individually (Fig. 19b). Similarly, the depth  $z_{\max}$  is similar in the LES and ROMS on many days, but there are numerous

outliers with much deeper  $z_{\max}$  in ROMS, such that the spatiotemporal correlation between ROMS and the LES is marginal to insignificant (Fig. 19c). These results support earlier indications that the mixing produced by KPP and the LES differ. Yet, these large day-to-day differences in the flux and diffusivity shown in Figs. 19a,b tend to take both signs and add up to fairly subtle impacts on the time-mean temperature and horizontal velocity tendencies due to vertical mixing (see Fig. A1) and therefore the mean velocity and temperature profiles over 34 days, as discussed in section 2b.

### g. Parameterization of $\langle F_b \rangle$ profiles

Finally, it is desirable to incorporate the information gleaned about  $\langle F_b \rangle^{\max}$  from the LES into parameterizations of flux profiles for application in ocean models or in estimating turbulent fluxes from observations without turbulence data. Although it is beyond the scope of this paper to incorporate the scaling for  $\langle F_b \rangle^{\max}$  into a complete mixing parameterization, we conclude the paper and motivate future work toward refined mixing parameterizations by presenting the results of a preliminary effort to parameterize the daily mean buoyancy flux profiles  $\langle F_b \rangle$  simulated in the LES based on  $\langle F_b \rangle^{\max}$ . It is important to emphasize that this effort involves a nonexhaustive exploration of a wide range of possible choices and thus is likely suboptimal. Nevertheless, we find that the results are valuable motivation and guidance for future work and thus worth presenting.

More precisely, the objective of this section is to model the daily averaged net buoyancy flux profile  $\langle B \rangle(z)$  from the surface  $z = 0$  to the base of the low-Richardson layer  $z = H_{\text{Rig}}$ , below which turbulent mixing is typically much weaker since  $H_{\text{Rig}}$  is highly correlated with  $z_{\text{pen}}$  (Fig. 14). That is, we seek to model

$$\langle B \rangle = \langle P_b \rangle + \langle F_b \rangle, \quad (9)$$

the sum of the daily averaged penetrative and turbulent buoyancy fluxes. We model  $\langle B \rangle$  rather than  $\langle F_b \rangle$  because  $\langle B \rangle$  profiles do not exhibit the exponential structure characteristic of  $\langle P_b \rangle$ , whereas  $\langle F_b \rangle$  profiles do (cf. Figs. 10a,b and 20a,b). Thus, we interpret  $\langle B \rangle$  as the residual turbulent flux, after subtracting the part of  $\langle F_b \rangle$  that is equal and opposite to the penetrating solar radiative flux  $\langle P_b \rangle$  (see the appendix for details on  $P_b$ ).

Rather than parameterize  $\langle B \rangle$  at each depth based on the local properties (as in several previous studies, e.g., Pacanowski and Philander 1981; Peters et al. 1988; Zaron and Moum 2009), the entire  $\langle B \rangle$  profile on a given day, from the surface to the base of the low- $R_{\text{ig}}$  layer  $z = H_{\text{Rig}}$ , is modeled from a shape function and three bulk parameters: the net air-sea fluxes of buoyancy  $\langle B(z=0) \rangle$  and momentum  $\langle |\tau|/\rho \rangle$  and the bulk vertical shear of horizontal currents  $S_b$  from  $H_{\text{Rig}}$  to 5-m depth. We take this bulk parameterization approach because we find that knowing  $\langle B \rangle$  at just  $z = 0$  and  $z = z_{\max}$  is sufficient to explain about 90% of the simulated variance in  $\langle B \rangle$  at all depths above  $H_{\text{Rig}}$  in the LES at both  $0^\circ$  and  $3^\circ\text{N}$ . In particular, we find that a linear combination

$$\langle B \rangle(z) = w_1(z)\langle B \rangle(z=0) + w_2(z)\langle B \rangle(z=z_{\max}) \quad (10)$$

explains about 90% of the variance in  $\langle B \rangle$  for all depths above  $H_{\text{Rig}}$  (cf. Figs. 20a,b,e,f), where

$$\langle B \rangle(z=0) = \frac{g\alpha}{\rho c_p} \langle Q_0 \rangle^{\text{net}} - g\beta \langle \text{VSF}_0^{\text{net}} \rangle, \quad (11)$$

$$\langle B \rangle(z=z_{\max}) = \langle F_b \rangle(z=z_{\max}) + \langle P_b \rangle(z=z_{\max}), \quad (12)$$

and  $Q_0^{\text{net}}$  and  $\text{VSF}_0^{\text{net}}$  are given net surface heat and virtual salt fluxes across the air-sea interface and  $\langle P_b \rangle$  is a given penetrative buoyancy flux profile associated with shortwave radiation (see the appendix for details). The depth-dependent weights  $w_1$  and  $w_2$  in (10) are piecewise linear functions of depth, that is,

$$w_1 = \frac{z_{\max} - z}{z_{\max}} \quad \text{for } z \leq z_{\max}, \quad (13)$$

$$w_1 = 0 \quad \text{for } z > z_{\max}, \quad (14)$$

$$w_2 = 1 - w_1 \quad \text{for } z \leq z_{\max}, \quad (15)$$

$$w_2 = \frac{H_{\text{Rig}} - z}{H_{\text{Rig}} - z_{\max}} \quad \text{for } H_{\text{Rig}} > z > z_{\max}, \quad (16)$$

where  $z$ ,  $z_{\max}$ , and  $H_{\text{Rig}}$  are all positive depths by definition in the expressions above. It may be noted that our approach results in piecewise constant heat flux convergence with one value below  $z_{\max}$  (with sign of  $\langle F_Q \rangle^{\max}$ ) and another above  $z_{\max}$  (with sign of  $\langle Q_0^{\text{net}} \rangle - \langle F_Q \rangle^{\max}$ ).

Having chosen to represent the vertical structure of  $\langle B \rangle$  as a piecewise linear function that depends on  $\langle B \rangle$  at just the surface and  $z_{\max}$  and taking the surface flux as given, the stated objective of this section is reduced to specifying  $\langle F_Q \rangle^{\max}$  and  $z_{\max}$ . To recapitulate previous sections, we use linear regression to model  $z_{\max}$ ,

$$z_{\max} \approx 0.6H_{\text{Rib}} + 14, \quad (17)$$

since we found that  $H_{\text{Rib}}$  could explain about half of the variance in  $z_{\max}$  (Fig. 14a). In addition, we use the scaling developed and discussed in sections 4e-4f (specifically, the one plotted in Fig. 17b) to model

$$\langle F_b \rangle^{\max} \approx 0.16u_*^{2.05} S_b^{0.98}. \quad (18)$$

With these parameterized representations of  $\langle F_Q \rangle^{\max}$  and  $z_{\max}$  in (10), we find that this linear combination explains 75% of the variance in simulated  $\langle B \rangle$  above  $H_{\text{Rig}}$  across both LES (cf. Figs. 20a-d;  $r^2 = 0.6$  and  $r^2 = 0.7$  at  $0^\circ$  and  $3^\circ\text{N}$ , respectively).

To put the flux profiles from the LES and the parameterization (10) in context, compare the results to those from the KPP output in parent regional ocean model (ROMS) at the LES locations (Fig. 20). Consistent with earlier results, there are qualitative differences between the flux profiles in the LES and ROMS (KPP). Perhaps most notably, strong mixing extends to deeper depths in ROMS (KPP), consistent with many instances of deeper  $z_{\max}$  (Fig. 19c). The ROMS

(KPP) solution also seems to have a more distinct modulation of mixing on the time scale of the tropical instability wave than in the LES. However, given the previously identified differences, including the absence of correlation between the LES and KPP in the depth  $z_{\max}$  or the turbulent diffusivity at  $z_{\max}$  in Fig. 19, it is perhaps remarkable how similar the KPP and LES solutions are (see also Fig. A1). In any case, the results of our preliminary effort to parameterize flux profiles suggest that future work is both justified and needed to incorporate information about  $\langle F_Q \rangle^{\max}$  into a more general mixing parameterization that handles momentum and tracer fluxes as well as an explicit diurnal cycle.

## 5. Conclusions

This manuscript synthesizes results from submesoscale-permitting regional ocean models and large-eddy simulations of turbulence embedded in a regional model to build understanding of deep-cycle turbulence and upper-ocean mixing more generally in the equatorial Pacific Ocean cold tongue at and beyond  $0^\circ$ ,  $140^\circ\text{W}$ .

First, a submesoscale-permitting regional hindcast simulation of the period 1999–2016 in the MITgcm is used to quantify the climatological mean, seasonal cycle, and aseasonal variability of ocean mixing as measured by the maximum over depth of the daily mean turbulent vertical heat flux  $\langle F_Q \rangle^{\max}$ . We found that there is a good spatial correlation ( $r^2 = 0.7$ ) between  $\langle F_Q \rangle^{\max}$  and the time-mean net ocean surface heat flux  $\langle Q_0^{\text{net}} \rangle$ . Although both  $\langle F_Q \rangle^{\max}$  and  $\langle Q_0^{\text{net}} \rangle$  are stronger in the cold tongue relative to other areas, there is a prominent equatorial mixing band within about  $1^\circ$ – $2^\circ$  of the equator where the time-mean, seasonal-cycle amplitude, and aseasonal variability are much larger in  $\langle F_Q \rangle^{\max}$  than  $\langle Q_0^{\text{net}} \rangle$ . Aseasonal anomalies in  $\langle F_Q \rangle^{\max}$  (i.e., all deviations from the climatological seasonal cycle) are uncorrelated with aseasonal anomalies in  $\langle Q_0^{\text{net}} \rangle$ , which suggests that the surface heat flux exerts little control on the aseasonal variability of ocean mixing in the cold tongue. In addition,  $\langle F_Q \rangle^{\max}$  is logarithmically distributed and exhibits rare but intense mixing events as far as  $5^\circ$  from the equator driven by mesoscale oceanic variability. Thus, strong mixing and DCT are not limited to the equatorial mixing band above the undercurrent, and aseasonal variability in general and infrequent strong mixing events in particular have substantial impacts on the climatologies of mixing across the cold tongue. As a result, the spatial patterns of aseasonal variance and time-mean  $\langle F_Q \rangle^{\max}$  are very similar. However, it is not clear if the parameterized mechanisms that control mixing in the regional model are realistic. Comparisons between modeled and measured turbulence at  $0^\circ$ ,  $140^\circ\text{W}$  suggest that the mixing has a realistic seasonal cycle in the regional model but the time-mean turbulent heat fluxes may be too strong and there may be too few instances of weak mixing at this location.

State-of-the-art large-eddy simulations embedded in a regional model simulate the outer scales of turbulence  $\mathcal{O}(1)$  m as it evolves over 34 days in response to changing atmospheric and oceanic forcing at both  $0^\circ$ ,  $140^\circ\text{W}$  and  $3^\circ\text{N}$ ,  $140^\circ\text{W}$  in October. The time-averaged LES results are consistent with the

spatial pattern of mixing simulated in the regional model. In particular, mixing is elevated below the surface both on and off the equator, but the time-mean  $\langle F_Q \rangle^{\max}$  in the LES is about 3–4 times stronger at  $0^\circ$  ( $110 \text{ W m}^{-2}$ ) than at  $3^\circ\text{N}$  ( $30 \text{ W m}^{-2}$ ) along  $140^\circ\text{W}$ . However, mixing in the LES is about a factor of 2 weaker than on average in all Octobers from 1999 to 2016 in the MITgcm. More direct comparisons between the mixing in the LES and its parent regional model ROMS, in which mixing occurs under essentially the same day-to-day oceanic and atmospheric conditions as in the LES but via the KPP scheme (Large et al. 1994) as in the MITgcm, also suggest that parameterized mixing in the regional model is stronger and more deeply penetrating than in the LES, but the time-mean  $\langle F_Q \rangle^{\max}$  is only 20% lower in the LES. Individually, these LES results may not be sufficient to conclude that the KPP mixing scheme yields too-strong mixing in the regional models, but taken with similar conclusions derived from comparisons to  $\chi$ pod microstructure observations, it seems likely that the time-mean mixing in the cold tongue is too strong in the regional models and the mixing scheme needs to be modified.

The LES results also provide important insight into the aseasonal variability of mixing and its covariates on time scales from days to a month and thus facilitate the identification and evaluation of empirical scalings for ocean mixing that might be applicable across a range of different atmospheric and oceanic conditions throughout the Pacific Ocean cold tongue and possibly beyond. A highlight is the finding that a relatively simple two-variable linear model approximately proportional to  $u_*^2 S_b$  can explain about 90% of this daily variance in  $\langle F_Q \rangle^{\max}$  across both LES locations, where  $u_*$  is the surface friction velocity,  $S_b$  is the bulk vertical shear of the ocean currents averaged from 5-m depth to  $H_{\text{Rig}}$ , below which  $\text{Ri}_g > 0.35$ . In an independent validation, this scaling explains 40% of the observed variance in the TIWE observations of Lien et al. (1995), which exhibit a similar distribution of  $\langle F_Q \rangle^{\max}$  as the LES at  $0^\circ$ ,  $140^\circ\text{W}$  with mean bias that is smaller than the measurement uncertainty of a factor of 2. Even more encouraging is that the empirical scaling can be interpreted with prior theory by Smyth et al. (2017) at  $0^\circ$ ,  $140^\circ\text{W}$ . However, while the scaling is successful off the equator at  $3^\circ\text{N}$ ,  $140^\circ\text{W}$ , its applicability beyond  $0^\circ$ ,  $140^\circ\text{W}$  cannot be interpreted with the theory of Smyth et al. (2017), nor has it been validated with observations. Nevertheless, the finding that LES simulates strong DCT at  $3^\circ\text{N}$ ,  $140^\circ\text{W}$  away from the undercurrent adds significant new evidence in support of these hypotheses that strong DCT, marginal instability, and intense mixing can occur both with and without the undercurrent, as long as the vertical shear of upper-ocean currents and (to a lesser degree) the wind stress are sufficiently strong (building on Pei et al. 2020; Cherian et al. 2021). However, future observational process studies are needed to refine and likely modify these hypotheses and scalings of ocean mixing throughout the cold tongue and particularly off the equator. In addition, these results are both a motivation and a promising foundation for needed refinement of the parameterizations of equatorial mixing in ocean models.

*Acknowledgments.* This work was funded by National Oceanic and Atmospheric Administration Contract

NA18OAR4310408 from the Climate Program Office. We would like to acknowledge high-performance computing support from Cheyenne (doi:10.5065/D6RX99HX) provided by NCAR's Computational and Information Systems Laboratory, sponsored by the National Science Foundation. We acknowledge the TAO mooring infrastructure and all of the people who sustain it. TAO observational data were made available by the GTMBA Project Office of NOAA/PMEL (<https://www.pmel.noaa.gov/tao/drupal/disdel/>). We acknowledge and thank Dr. Michael Gregg for his leadership in the collection of the TIWE microstructure data, which greatly enhanced this work. And, we more broadly acknowledge and thank the TIWE team that contributed to the success of the data collection at sea (see also Lien et al. 1995). Also, we acknowledge the many contributors to the  $\chi$ pod deployments that made the observational comparison in Fig. 7 possible (see also Moum et al. 2013). We acknowledge and thank Dr. John Taylor, the principal developer of the LES, as well as all of the contributors to and developers of the DIABLO LES, MITgcm, ROMS, and CESM. This material is based upon work supported by the National Center for Atmospheric Research (NCAR), which is a major facility sponsored by the NSF under Cooperative Agreement 1852977. DBW also acknowledges support from NASA's research and analysis (physical oceanography) and the NSF physical oceanography programs. RMH acknowledges support from the Australian Research Council through award DE21010004. Finally, we acknowledge many constructive comments from two anonymous reviewers.

*Data availability statement.* Data and software necessary to reproduce the figures are published and links are as follows: LES data: <https://doi.org/10.6084/m9.figshare.14786109>; MITgcm data: <https://doi.org/10.6084/m9.figshare.14787420>; ROMS data: <https://doi.org/10.6084/m9.figshare.17009660>; ROMS and LES code bases and configuration files: <https://doi.org/10.5281/zenodo.5716181>; analysis and visualization software: <https://doi.org/10.5281/zenodo.5932697>.

## APPENDIX

### Large-Eddy Simulation Methods

The LES (Taylor 2008; Whitt and Taylor 2017; Watkins and Whitt 2020) solves a filtered version of the Navier–Stokes equations under the Boussinesq approximation on a traditional  $f$  plane along with evolution equations for temperature and salinity,

$$\frac{D\mathbf{u}}{Dt} + \mathbf{f} \times \mathbf{u} = -\frac{1}{\rho} \nabla p + \mathbf{b} + \nabla \cdot (\nu_{\text{sgs}} \nabla \mathbf{u}) + \mathcal{F}_{\mathbf{u}} + \mathcal{R}_{\mathbf{u}} + \mathcal{D}_{\mathbf{u}}, \quad (\text{A1})$$

$$\nabla \cdot \mathbf{u} = 0, \quad (\text{A2})$$

$$\frac{DT}{Dt} = \nabla \cdot (\kappa_{\text{sgs}} \nabla T) + I + \mathcal{F}_T + \mathcal{R}_T + \mathcal{D}_T, \quad (\text{A3})$$

$$\frac{DS}{Dt} = \nabla \cdot (\kappa_{\text{sgs}} \nabla S) + \mathcal{F}_S + \mathcal{R}_S + \mathcal{D}_S, \quad (\text{A4})$$

$$b = -g[1 - \alpha(T - T_0) + \beta(S - S_0)], \quad (\text{A5})$$

where  $\mathbf{f} = (0, 0, f)$ ,  $f = 14.6 \times 10^{-5} \sin(\text{latitude}) \text{ s}^{-1}$  is the traditional Coriolis frequency, the buoyancy force is  $\mathbf{b} = (0, 0, b)$ , the density of the seawater is  $-\rho b/g$ , where the constant reference density of seawater  $\rho = 1023.5 \text{ kg m}^{-3}$ ,  $g = 9.81 \text{ m s}^{-2}$ , and the density and buoyancy vary linearly with temperature  $T$  and salinity  $S$ ;  $\alpha = 2.96 \times 10^{-4} \text{ }^\circ\text{C}^{-1}$ ,  $T_0 = 25.0^\circ\text{C}$ ,  $\beta = 7.38 \times 10^{-4} \text{ psu}^{-1}$ , and  $S_0 = 35.25 \text{ psu}$ . The equations are solved in a horizontally periodic domain that is 108 m deep and  $306 \text{ m} \times 306 \text{ m}$  square and discretized on a mesh with  $216 \times 360 \times 360$  points with a resolution of 0.5 m vertically  $\times$  0.85 m horizontally.

The vertical profiles of temperature, salinity, and horizontal momentum are initialized in the LES at 0600 UTC 2 October 1985 by interpolating the output of a hindcast from the Regional Ocean Modeling System (ROMS) (Shchepetkin and McWilliams 2005; Haidvogel et al. 2008), which simulates the period August 1984–February 1986 in a regional ocean domain spanning  $95^\circ$ – $170^\circ\text{W}$  and  $12^\circ\text{S}$ – $12^\circ\text{N}$  at  $1/20^\circ$  (5.5 km) horizontal resolution on 50 terrain-following sigma levels (spaced about every 8 m in the top 100 m) as in Holmes and Thomas (2015). The interpolation procedure involves first averaging the 6-h averaged ROMS output horizontally over a  $3 \times 3$  array of grid cells (about 16.5 km square) around the LES location and then interpolating vertically to the LES grid using cubic splines. The ROMS hindcast was used as the parent model instead of the MITgcm hindcast described above mainly because it was available with all relevant outputs before the MITgcm run was completed. In ROMS, the initial conditions and daily ocean side boundary conditions are from the global meso-scale-resolving ocean/sea ice hindcast used by Deppenmeier et al. (2021). Neither model has tides. In both of these regional and global ocean models, the surface fluxes are calculated using the JRA55-do atmospheric reanalysis (Tsujino et al. 2018) and the same bulk flux algorithms (Large and Yeager 2004, 2009; see also Small et al. 2015; Whitt et al. 2019). In particular, the ROMS hindcast is forced by a diurnal cycle of shortwave radiation (3-hourly) and vertical mixing is parameterized with the KPP scheme of Large et al. (1994) with the same parameters as in the Parallel Ocean Program used by Deppenmeier et al. (2021) (as in Whitt et al. 2019). The resulting diurnal cycles of upper-ocean turbulence look qualitatively similar to those reported in Cherian et al. (2021) and simulated in MITgcm with the same mixing parameterization, surface forcing, and horizontal grid resolution.

The subgrid-scale viscosity in the LES  $\nu_{\text{sgs}} = \nu_0 + \nu_t$  includes small and constant “molecular” viscosity  $\nu_0 =$

$10^{-6} \text{ m}^2 \text{ s}^{-1}$ . The much larger and variable turbulent viscosity is modeled after [Kaltenbach et al. \(1994\)](#), that is,

$$\nu_t = C_s^2 \Delta^2 (2S'_{ij}S'_{ji})^{1/2} \quad (\text{A6})$$

where the Smagorinski coefficient  $C_s = 0.13$ , the grid scale  $\Delta = (2\delta x \delta y \delta z)^{1/3}$  (where  $\delta x$ ,  $\delta y$ , and  $\delta z$  are grid spacings in the  $x$ ,  $y$  and  $z$  dimensions), and the resolved deformation tensor is  $\delta_{ij} = 1/2[(\partial u_i/\partial x_j) + (\partial u_j/\partial x_i)]$  and  $i, j = 1, 2, 3$  correspond to  $x, y, z$  dimensions and summation over repeated indices is implied and the horizontally averaged shear is subtracted from the deformation tensor  $S_{ij}$  in  $S'_{ij}$ . The diffusivity  $\kappa_{\text{sgs}} = \kappa_0 + \nu_t/\text{Pr}_t$ , where the turbulent Prandtl number is as in [Whitt and Taylor \(2017\)](#) based on [Anderson \(2009\)](#),

$$\text{Pr}_t = \left(1 + \frac{\text{Ri}_{\text{GS}}}{0.94}\right)^{1.5}, \quad (\text{A7})$$

and the gridscale gradient Richardson number is

$$\text{Ri}_{\text{GS}} = \frac{\delta b \delta z}{\delta u^2 + \delta v^2}, \quad (\text{A8})$$

where  $\delta b$ ,  $\delta z$ ,  $\delta u$ , and  $\delta v$  are the vertical differences in buoyancy, depth, and horizontal velocity between two adjacent grid cells.

At the top surface  $z = 0$ , the horizontally uniform vertical fluxes are specified via time-evolving gradient boundary conditions:

$$\frac{\partial \mathbf{u}_h}{\partial z} = \frac{\boldsymbol{\tau}}{\rho \nu_{\text{SGS}}}, \quad (\text{A9})$$

$$\frac{\partial T}{\partial z} = \frac{Q_0^{\text{net}} - P_Q(0)}{\rho c_p \kappa_{\text{SGS}}}, \quad (\text{A10})$$

$$\frac{\partial S}{\partial z} = \frac{\text{VSF}_0^{\text{net}}}{\kappa_{\text{SGS}}}, \quad (\text{A11})$$

where  $\nu_{\text{sgs}} = \nu_0$ ,  $\kappa_{\text{sgs}} = \kappa_0$  are constant,  $c_p = 4000 \text{ J kg}^{-1} \text{ }^\circ\text{C}^{-1}$  is the specific heat of the seawater, and the net virtual salt flux  $\text{VSF}_0^{\text{net}}$ , the net surface heat flux  $Q_0^{\text{net}}$ , the net surface shortwave heat flux  $P_Q(0)$ , and the surface wind stress  $\boldsymbol{\tau}$  are linearly interpolated from the 6-hourly averaged ROMS fluxes, averaged over a 16.5 km square around the LES location, and shown in [Fig. 10](#). Thus, the fluxes do not depend on the LES state. There is a diurnal cycle of shortwave solar radiation  $P_Q(0)$ , which penetrates and warms the interior of the LES during daytime as described below. The top is rigid, so the vertical velocity  $w = 0$  at  $z = 0$  (see [Fig. 10](#)). The LES domain bottom is rigid,  $w = 0$ , with  $u = 0.865$  and  $0.465 \text{ m s}^{-1}$  at  $0^\circ$  and  $3^\circ\text{N}$ , respectively,  $v = 0 \text{ m s}^{-1}$ ,  $T = 22.3^\circ\text{C}$ , and  $S = 35.28$  psu are held constant. Although a variable bottom boundary to match the parent model solution would be preferred, the constant bottom boundary is thought to have little impact on the results in this study, because we set  $\nu_{\text{sgs}} = \nu_0 = 10^{-6} \text{ m}^2 \text{ s}^{-1}$  at the interface between the bottom boundary velocity and

the first interior point. Thus, the horizontally averaged velocity and temperature profiles evolve to remain approximately consistent with ROMS and are as shown in [Fig. 9](#), and the resulting artificially strong vertical gradients at the domain bottom do not result in strong vertical fluxes of momentum, temperature, and salinity that significantly modify the interior evolution. Yet, extra caution should be exercised when interpreting the turbulent statistics near the bottom of the LES domain (e.g., [Fig. 12h](#)).

Interior warming due to solar radiation is represented as the convergence of a two-component exponential:

$$I(t, z) = \frac{I_0(t)}{\rho c_p} \frac{\partial}{\partial z} [a_I e^{-z/\xi_{I1}} + (1 - a_I) e^{-z/\xi_{I2}}], \quad (\text{A12})$$

where  $a_I = 0.58$ ,  $\xi_{I1} = 2.0 \text{ m}$ ,  $\xi_{I2} = 23 \text{ m}$  and net incoming shortwave radiation  $I_0$  ( $\text{W m}^{-2}$ ) has a diurnal cycle and is linearly interpolated from 6-h-average ROMS output. We call the total penetrative heat flux from solar radiation

$$P_Q(t, z) = I_0(t) [a_I e^{-z/\xi_{I1}} + (1 - a_I) e^{-z/\xi_{I2}}], \quad (\text{A13})$$

and the analogous penetrative buoyancy flux is  $P_b = P_Q \alpha / (\rho c_p)$ . The chosen profile  $P_Q(z)$  is a modified Jerlov type I profile ([Paulson and Simpson 1977](#)), such that the first  $e$ -folding scale is increased from 0.35 to 2.0 m in an ad hoc attempt to compensate for missing near-surface mixing due to surface gravity waves as in [Watkins and Whitt \(2020\)](#).

There are three new terms on the right side of the equations that are new implementations specific for this study and discussed briefly in the main methods section of the manuscript. These terms, large-scale tendencies  $\mathcal{F}$ , restoring  $\mathcal{R}$ , and damping  $\mathcal{D}$ , are included to make the solution more realistic given the limited domain size. First,  $\mathcal{F}(t, z)$  includes horizontally uniform (in the LES) large-scale tendencies, that is,

$$\mathcal{F}_u(z, t) = -\mathbf{u}_{\text{ROMS}} \cdot \nabla \mathbf{u}_{\text{ROMS}} - \frac{1}{\rho} \frac{\partial p_{\text{ROMS}}}{\partial x} + D_{u_{\text{ROMS}}}, \quad (\text{A14})$$

$$\mathcal{F}_v(z, t) = -\mathbf{u}_{\text{ROMS}} \cdot \nabla \mathbf{v}_{\text{ROMS}} - \frac{1}{\rho} \frac{\partial p_{\text{ROMS}}}{\partial y} + D_{v_{\text{ROMS}}}, \quad (\text{A15})$$

$$\mathcal{F}_w(z, t) = 0, \quad (\text{A16})$$

$$\mathcal{F}_T(z, t) = -\mathbf{u}_{\text{ROMS}} \cdot \nabla T_{\text{ROMS}} + D_{T_{\text{ROMS}}}, \quad (\text{A17})$$

$$\mathcal{F}_S(z, t) = 0, \quad (\text{A18})$$

where  $D$  represents the explicit lateral mixing from ROMS. The restoring  $\mathcal{R}$  operates throughout the entire depth of the LES domain but operates only on the horizontal average:

$$\mathcal{R}_u(z, t) = -(\bar{u} - u_{\text{ROMS}})/t_r, \quad (\text{A19})$$

$$\mathcal{R}_v(z, t) = -(\bar{v} - v_{\text{ROMS}})/t_r, \quad (\text{A20})$$

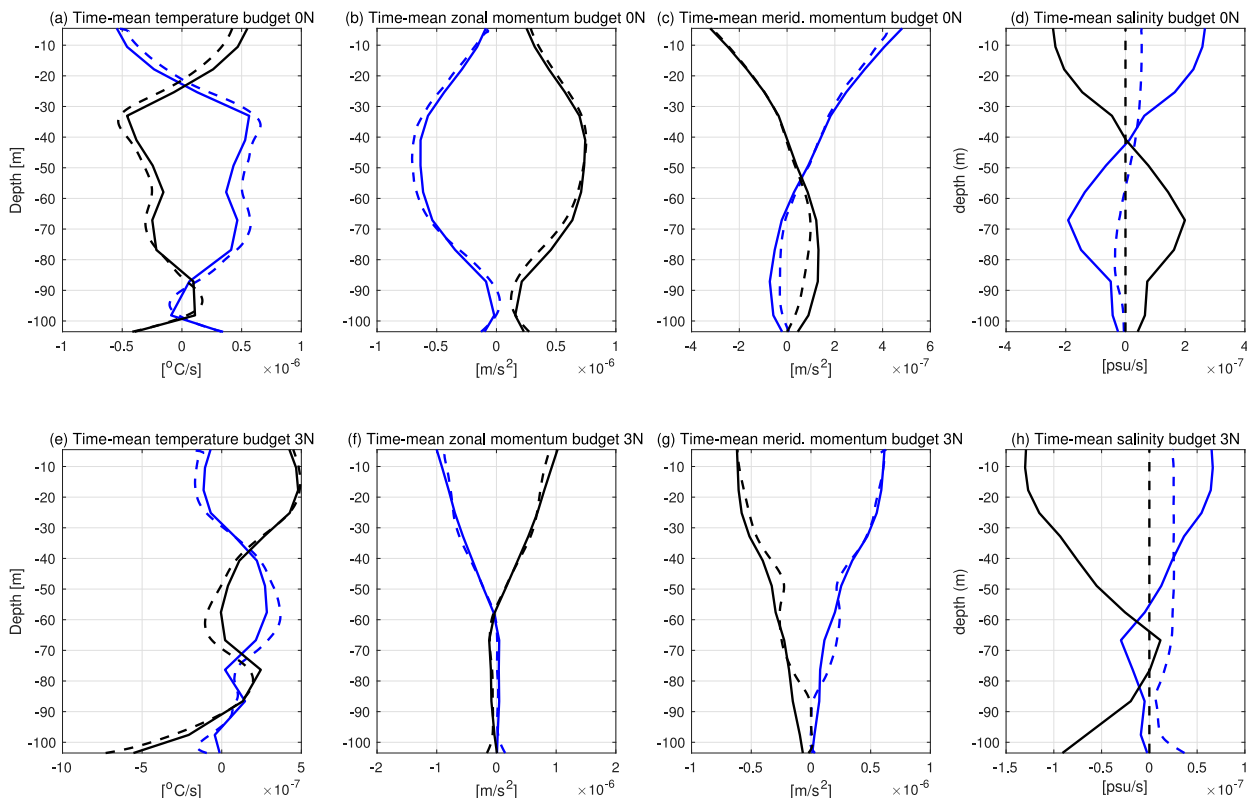


FIG. A1. Time means of various terms in the horizontally averaged tracer and momentum budgets from ROMS (solid lines) and LES (dashed lines) at (top)  $0^\circ$ ,  $140^\circ\text{W}$  and (bottom)  $3^\circ\text{N}$ ,  $140^\circ\text{W}$ . The blue lines represent the time-mean convergence of vertical transport of (a),(e) temperature, (b),(f) zonal momentum, and (c),(g) meridional momentum and (d),(h) salinity due to turbulence (and solar radiation in the case of temperature). The black lines represent all other tendencies of horizontally averaged momentum and tracers as diagnosed from ROMS, i.e.,  $\mathcal{F}$  (plus Coriolis in the case of momentum), and as diagnosed in LES, i.e.,  $\mathcal{F} + \mathcal{R}$  (plus Coriolis in the case of momentum). See the [appendix](#) for the budget formulas.

$$\mathcal{R}_w(z,t) = 0, \quad (\text{A21})$$

$$\mathcal{R}_T(z,t) = -(\overline{T} - T_{\text{ROMS}})/t_r, \quad (\text{A22})$$

$$\mathcal{R}_S(z,t) = 0, \quad (\text{A23})$$

where the overbar denotes the lateral average and the restoring time scale  $t_r = 11.6$  days ( $10^6$  s). In general,  $\mathcal{F} \gg \mathcal{R}$  because  $t_r$  is so long.

Since the LES only simulates a small domain, the tendencies associated with larger scales, namely,  $\mathcal{F}$ , which includes three-dimensional advection, horizontal mixing, and the pressure gradient force but excludes the Coriolis force and vertical mixing because they are simulated in LES, are obtained from the 6-hourly averaged budget diagnostic output of ROMS and are independent of the LES state. These large-scale tendencies are first averaged over a  $3 \times 3$  array of ROMS grid cells (about a  $16.5$  km square) centered on the LES locations, then interpolated using cubic splines from the ROMS sigma levels (about every  $8$  m) to the LES vertical levels, and finally linearly interpolated in time and added as a tendency to the horizontally averaged components of the LES momentum and tracer

equations as the LES runs (as expressed in equations above). The analogous large-scale interior salinity tendencies are set to zero in the LES for simplicity. Although the omission of interior salinity tendencies may complicate the interpretation, temperature is highly correlated with buoyancy (initial  $r^2 = 0.99$  at both  $0^\circ$  and  $3^\circ\text{N}$ ,  $140^\circ\text{W}$ ) and has a threefold stronger influence on buoyancy than salinity in the region. Specifically, the initial bulk  $108$ -m buoyancy differences are  $0.0029$   $\text{m s}^{-2}$  (for a  $0.4$  psu salinity difference) and  $0.0080$   $\text{m s}^{-2}$  (for a  $2.74^\circ\text{C}$  temperature difference) at  $0^\circ$ ,  $140^\circ\text{W}$ . Thus, the results are expected to be qualitatively unaffected by the omission of interior salinity tendencies, but future simulations are required to precisely quantify the turbulent response to salinity advection.

Finally, the fluctuations below  $84$ -m depth are slowly damped toward zero:

$$\mathcal{D}_u(z,t) = -\sigma(u - \bar{u})/t_r, \quad (\text{A24})$$

$$\mathcal{D}_v(z,t) = -\sigma(v - \bar{v})/t_r, \quad (\text{A25})$$

$$\mathcal{D}_w(z,t) = -\sigma w/t_r, \quad (\text{A26})$$

$$\mathcal{D}_T(z,t) = -\sigma(T - \bar{T})/t_r, \quad (\text{A27})$$

$$\mathcal{D}_S(z,t) = -\sigma(S - \bar{S})/t_r, \quad (\text{A28})$$

where

$$\sigma(z) = \left( \frac{z + H - L_s}{L_s} \right)^2 \quad \text{for } z < (L_s - H) \quad \text{and} \quad (\text{A29})$$

$$\sigma(z) = 0 \quad \text{for } z \geq (L_s - H), \quad (\text{A30})$$

where  $z$  is the depth from 0 to  $-H$ ,  $H = 108$  m is the domain height,  $L_s = 24$  m is the thickness of the damping layer. It is notable that the time scale  $t_r$  is very long; it is about 66 days at 94 m, 17 days at 104 m, and 12 days at the bottom 108 m. These time scales are much longer than the time scale of the relevant stratified shear instabilities or internal waves (Smyth et al. 2011; Moum et al. 2011) and thus the damping has a negligible influence on shear instabilities, internal waves, and turbulence at essentially all depths (the damping is of the order  $10^{-12}$ – $10^{-10}$   $\text{m}^2 \text{s}^{-3}$ ), and the DCT never gets within 15 m of the bottom in any case. Despite the slow damping rate and shallow domain bottom, the bottom 20 m remains strongly stratified with internal wave fluctuations that are weak compared to DCT. Short tests with a deeper 144-m domain suggested that the shallow domain bottom does not qualitatively impact the results. The stability analysis of Smyth et al. (2011) also suggests that the shallow domain depth is unlikely to impact the results since all of the shear instabilities they identify occur at depths shallower than 100 m and have a thickness of 20–40 m.

This manuscript focuses on the horizontally averaged dynamics in the LES,

$$\frac{\partial \bar{\mathbf{u}}_h}{\partial t} = -\mathbf{f} \times \bar{\mathbf{u}}_h + \frac{\partial}{\partial z} \left( \overline{\nu_{\text{sgs}} \frac{\partial \mathbf{u}_h}{\partial z} - \mathbf{w} \mathbf{u}_h} \right) + \mathcal{F}_u + \mathcal{R}_u, \quad (\text{A31})$$

$$\frac{\partial \bar{T}}{\partial t} = \frac{\partial}{\partial z} \left( \overline{\kappa_{\text{sgs}} \frac{\partial T}{\partial z} - wT} \right) + I + \mathcal{F}_T + \mathcal{R}_T, \quad (\text{A32})$$

$$\frac{\partial \bar{S}}{\partial t} = \frac{\partial}{\partial z} \left( \overline{\kappa_{\text{sgs}} \frac{\partial S}{\partial z} - wS} \right), \quad (\text{A33})$$

$$\bar{b} = -g[1 - \alpha(\bar{T} - T_0) + \beta(\bar{S} - S_0)]. \quad (\text{A34})$$

The right-hand-side terms in these budgets are averaged over the duration of the LES simulations and plotted in Fig. A1 and compared with output from ROMS [the subscript  $h$  indicates horizontal, e.g., the horizontal velocity vector  $(u, v, 0)$ ]. We define

$$\mathbf{F}_m = \left( \overline{\nu_{\text{sgs}} \frac{\partial \mathbf{u}_h}{\partial z} - \mathbf{w} \mathbf{u}_h} \right), \quad \text{and} \quad (\text{A35})$$

$$F_b = \left( \overline{\kappa_{\text{sgs}} \frac{\partial b}{\partial z} - wb} \right) = g(\alpha F_T - \beta F_S), \quad (\text{A36})$$

where  $F_T$  and  $F_S$  have the same functional form as  $F_b$  but operate on temperature (A32) and salinity (A33). The

kinetic and potential energy equations for the horizontally averaged state are then given by

$$\frac{\partial |\bar{\mathbf{u}}_h|^2/2}{\partial t} = \frac{\partial}{\partial z} (\bar{\mathbf{u}}_h \cdot \mathbf{F}_m) - \mathbf{F}_m \cdot \frac{\partial \bar{\mathbf{u}}_h}{\partial z} + \bar{\mathbf{u}}_h \cdot \mathcal{F}_u + \bar{\mathbf{u}}_h \cdot \mathcal{R}_u, \quad (\text{A37})$$

$$\frac{\partial \bar{b}z}{\partial t} = \frac{\partial}{\partial z} (zF_b) - F_b + z\mathcal{F}_b + z\mathcal{R}_b, \quad (\text{A38})$$

and  $\mathcal{F}_b = g(\alpha \mathcal{F}_T - \beta \mathcal{F}_S)$  and similarly for  $\mathcal{R}_b$ . On the right hand side, the first terms represent vertical redistribution or transport in the interior and sources and sinks at the surface boundary (e.g., wind work on the mean flow). The third and fourth terms are interior sources and sinks related to the larger-scale dynamics inherited from ROMS (e.g., advection, pressure work, etc.). The second term is the sink of mean kinetic energy to turbulence usually referred to as shear production  $-\mathbf{F}_m \cdot \partial \bar{\mathbf{u}}_h / \partial z$  and the source of potential energy due to turbulent vertical mixing or buoyancy flux  $-F_b$ .

The governing equation for the horizontally averaged turbulent kinetic energy (i.e., for  $k = |\mathbf{u}'|^2/2$ , where  $\mathbf{u}' = \mathbf{u} - \bar{\mathbf{u}}$ ) is given by

$$\frac{\partial k}{\partial t} + \frac{\partial}{\partial z} \left( \overline{w\bar{p}}/\rho + \overline{wk} - \nu_{\text{SGS}} \frac{\partial k}{\partial z} - \overline{\mathbf{u}' \nu_{\text{SGS}} \frac{\partial \bar{\mathbf{u}}}{\partial z}} \right) = -\overline{w\mathbf{u}'_h} \cdot \frac{\partial \bar{\mathbf{u}}_h}{\partial z} + \overline{wb} - \epsilon + \overline{\mathbf{u}' \cdot \mathcal{D}_u} \quad (\text{A39})$$

where the dissipation of turbulent kinetic energy is  $\bar{\epsilon} = \nu_{\text{SGS}} S'_{ij} S'_{ji} + \nu_{\text{SGS}} \partial \mathbf{u}'_h / \partial z \cdot \partial \bar{\mathbf{u}}_h / \partial z$ . In the limit that  $\nu_t \rightarrow 0$ , the shear production and buoyancy flux terms in the turbulent kinetic energy equation and the mean kinetic energy/potential energy equations become effectively identical. However, because the LES is a filtered approximation of high-Reynolds number flow with finite  $\nu_t \approx \nu_0$ , a finite amount of mean-profile buoyancy flux, shear production and total dissipation occur via the subgrid scales without passing through  $k$ . Hence, we plot the total dissipation  $\nu_{\text{SGS}} S'_{ij} S'_{ji}$ , shear production  $\mathbf{F}_m \cdot \partial \bar{\mathbf{u}}_h / \partial z$ , and buoyancy flux  $F_b$  throughout the manuscript and define the deviations from this balance to be transport and transience, i.e.,

$$T = \mathbf{F}_m \cdot \frac{\partial \bar{\mathbf{u}}_h}{\partial z} - F_b - \epsilon, \quad (\text{A40})$$

where  $\epsilon$  is total dissipation. Consistent with the discussion in Osborn (1980), the left hand side is generally small when averaged horizontally and over a full day at  $z_{\text{max}}$  in the LES. For reference, the subgrid-scale parts of  $F_b$  and  $F_m$  are small relative to the resolved parts where  $F_b$  and  $\epsilon$  are strong and  $\text{Ri}_g$  is low, e.g., above  $H_{\text{Rig}}$  or shallower than about 75-m depth on average. The subgrid-scale fluxes become relatively large deeper in the thermocline, where  $\text{Ri}_g > 1$  is relatively high and  $F_b$  and  $\epsilon$  are relatively weak, e.g., below  $H_{\text{Rig}}$  or below 75 m on average; results from these depths should be interpreted more cautiously.

## REFERENCES

- Adcroft, A., C. Hill, J.-M. Campin, J. Marshall, and P. Heimbach, 2004: Overview of the formulation and numerics of the MIT GCM. *Proc. ECMWF Seminar Series on Numerical Methods, Recent Developments in Numerical Methods for Atmosphere and Ocean Modelling*, Reading, United Kingdom, ECMWF, 139–149, <https://www.ecmwf.int/en/elibrary/7642-overview-formulation-and-numerics-mit-gcm>.
- Anderson, P. S., 2009: Measurement of Prandtl number as a function of Richardson number avoiding self-correlation. *Bound.-Layer Meteor.*, **131**, 345–362, <https://doi.org/10.1007/s10546-009-9376-4>.
- Brainerd, K. E., and M. C. Gregg, 1995: Surface mixed and mixing layer depths. *Deep-Sea Res. I*, **42**, 1521–1543, [https://doi.org/10.1016/0967-0637\(95\)00068-H](https://doi.org/10.1016/0967-0637(95)00068-H).
- Brannigan, L., Y.-D. Lenn, T. P. Rippeth, E. McDonagh, T. K. Chereskin, and J. Sprintall, 2013: Shear at the base of the oceanic mixed layer generated by wind shear alignment. *J. Phys. Oceanogr.*, **43**, 1798–1810, <https://doi.org/10.1175/JPO-D-12-0104.1>.
- Burchard, H., and T. P. Rippeth, 2009: Generation of bulk shear spikes in shallow stratified tidal seas. *J. Phys. Oceanogr.*, **39**, 969–985, <https://doi.org/10.1175/2008JPO4074.1>.
- Cherian, D., D. Whitt, R. Holmes, R.-C. Lien, S. Bachman, and W. Large, 2021: Off-equatorial deep-cycle turbulence forced by tropical instability waves in the equatorial Pacific. *J. Phys. Oceanogr.*, **51**, 1575–1593, <https://doi.org/10.1175/JPO-D-20-0229.1>.
- Crawford, W. R., 1982: Pacific equatorial turbulence. *J. Phys. Oceanogr.*, **12**, 1137–1149, [https://doi.org/10.1175/1520-0485\(1982\)012<1137:PET>2.0.CO;2](https://doi.org/10.1175/1520-0485(1982)012<1137:PET>2.0.CO;2).
- Danabasoglu, G., W. G. Large, J. J. Tribbia, P. R. Gent, B. P. Briegleb, and J. C. McWilliams, 2006: Diurnal coupling in the tropical oceans of CCSM3. *J. Climate*, **19**, 2347–2365, <https://doi.org/10.1175/JCLI3739.1>.
- Deppenmeier, A.-L., F. O. Bryan, W. Kessler, and L. Thompson, 2021: Modulation of cross-isothermal velocities with ENSO in the tropical Pacific cold tongue. *J. Phys. Oceanogr.*, **51**, 1559–1574, <https://doi.org/10.1175/JPO-D-20-0217.1>.
- Gentemann, C., and Coauthors, 2020: Saildrone: Adaptively sampling the marine environment. *Bull. Amer. Meteor. Soc.*, **101**, E744–E762, <https://doi.org/10.1175/BAMS-D-19-0015.1>.
- Gregg, M. C., H. Peters, J. Wesson, N. Oakey, and T. Shay, 1985: Intensive measurements of turbulence and shear in the equatorial undercurrent. *Nature*, **318**, 140–144, <https://doi.org/10.1038/318140a0>.
- , T. B. Sanford, and D. P. Winkel, 2003: Reduced mixing from the breaking of internal waves in equatorial waters. *Nature*, **422**, 513–515, <https://doi.org/10.1038/nature01507>.
- , E. A. D'Asaro, J. J. Riley, and E. Kunze, 2018: Mixing efficiency in the ocean. *Annu. Rev. Mar. Sci.*, **10**, 443–473, <https://doi.org/10.1146/annurev-marine-121916-063643>.
- Haidvogel, D., and Coauthors, 2008: Ocean forecasting in terrain-following coordinates: Formulation and skill assessment of the regional ocean modeling system. *J. Comput. Phys.*, **227**, 3595–3624, <https://doi.org/10.1016/j.jcp.2007.06.016>.
- Halpern, D., R. A. Knox, and D. S. Luther, 1988: Observations of 20-day period meridional current oscillations in the upper ocean along the Pacific equator. *J. Phys. Oceanogr.*, **18**, 1514–1534, [https://doi.org/10.1175/1520-0485\(1988\)018<1514:OODPMC>2.0.CO;2](https://doi.org/10.1175/1520-0485(1988)018<1514:OODPMC>2.0.CO;2).
- Holmes, R. M., and L. Thomas, 2015: The modulation of equatorial turbulence by tropical instability waves in a regional ocean model. *J. Phys. Oceanogr.*, **45**, 1155–1173, <https://doi.org/10.1175/JPO-D-14-0209.1>.
- , and —, 2016: Modulation of tropical instability wave intensity by equatorial Kelvin waves. *J. Phys. Oceanogr.*, **46**, 2623–2643, <https://doi.org/10.1175/JPO-D-16-0064.1>.
- , J. D. Zika, and M. H. England, 2019a: Diathermal heat transport in a global ocean model. *J. Phys. Oceanogr.*, **49**, 141–161, <https://doi.org/10.1175/JPO-D-18-0098.1>.
- , —, R. Ferrari, A. F. Thompson, E. R. Newsom, and M. H. England, 2019b: Atlantic Ocean heat transport enabled by Indo-Pacific heat uptake and mixing. *Geophys. Res. Lett.*, **46**, 13 939–13 949, <https://doi.org/10.1029/2019GL085160>.
- Holt, S. E., J. R. Koseff, and J. H. Ferziger, 1992: A numerical study of the evolution and structure of homogeneous stably stratified sheared turbulence. *J. Fluid Mech.*, **237**, 499–539, <https://doi.org/10.1017/S0022112092003513>.
- Howard, L. N., 1961: Note on a paper of John W. Miles. *J. Fluid Mech.*, **10**, 509–512, <https://doi.org/10.1017/S0022112061000317>.
- Huguenin, M. F., R. M. Holmes, and M. H. England, 2020: Key role of diabatic processes in regulating warm water volume variability over ENSO events. *J. Climate*, **33**, 9945–9964, <https://doi.org/10.1175/JCLI-D-20-0198.1>.
- Inoue, R., R.-C. Lien, and J. Moum, 2012: Modulation of equatorial turbulence by a tropical instability wave. *J. Geophys. Res.*, **117**, C10009, <https://doi.org/10.1029/2011JC007767>.
- , —, J. N. Moum, R. C. Perez, and M. C. Gregg, 2019: Variations of equatorial shear, stratification, and turbulence within a tropical instability wave cycle. *J. Geophys. Res. Oceans*, **124**, 1858–1875, <https://doi.org/10.1029/2018JC014480>.
- Jia, Y., K. J. Richards, and H. Annamalai, 2021: The impact of vertical resolution in reducing biases in sea surface temperature in a tropical Pacific Ocean model. *Ocean Modell.*, **157**, 101722, <https://doi.org/10.1016/j.ocemod.2020.101722>.
- Jing, Z., L. Wu, D. Wu, and B. Qiu, 2014: Enhanced 2-h–8-day oscillations associated with tropical instability waves. *J. Phys. Oceanogr.*, **44**, 1908–1918, <https://doi.org/10.1175/JPO-D-13-0189.1>.
- Johnson, G. C., B. M. Sloyan, W. S. Kessler, and K. E. McTaggart, 2002: Direct measurements of upper ocean currents and water properties across the tropical Pacific during the 1990s. *Prog. Oceanogr.*, **52**, 31–61, [https://doi.org/10.1016/S0079-6611\(02\)00021-6](https://doi.org/10.1016/S0079-6611(02)00021-6).
- Kaltenbach, H.-J., T. Gerz, and U. Schumann, 1994: Large-eddy simulation of homogeneous turbulence and diffusion in stably stratified shear flow. *J. Fluid Mech.*, **280**, 1–40, <https://doi.org/10.1017/S0022112094002831>.
- Large, W. G., and P. R. Gent, 1999: Validation of vertical mixing in an equatorial ocean model using large eddy simulations and observations. *J. Phys. Oceanogr.*, **29**, 449–464, [https://doi.org/10.1175/1520-0485\(1999\)029<0449:VOVMIA>2.0.CO;2](https://doi.org/10.1175/1520-0485(1999)029<0449:VOVMIA>2.0.CO;2).
- , and S. G. Yeager, 2004: Diurnal to decadal global forcing for ocean and sea-ice models: The data sets and flux climatologies. NCAR/TN-460+STR, 105 pp., <https://doi.org/10.5065/D6KK98Q6>.
- , and S. Yeager, 2009: The global climatology of an interannually varying air–sea flux data set. *Climate Dyn.*, **33**, 341–364, <https://doi.org/10.1007/s00382-008-0441-3>.
- , J. C. McWilliams, and S. C. Doney, 1994: Oceanic vertical mixing: A review and a model with a nonlocal boundary layer parameterization. *Rev. Geophys.*, **32**, 363–403, <https://doi.org/10.1029/94RG01872>.



- Li, G., and S.-P. Xie, 2014: Tropical biases in CMIP5 multimodel ensemble: The excessive equatorial Pacific cold tongue and double ITCZ problems. *J. Climate*, **27**, 1765–1780, <https://doi.org/10.1175/JCLI-D-13-00337.1>.
- , Y. Du, H. Xu, and B. Ren, 2015: An intermodel approach to identify the source of excessive equatorial Pacific cold tongue in CMIP5 models and uncertainty in observational datasets. *J. Climate*, **28**, 7630–7640, <https://doi.org/10.1175/JCLI-D-15-0168.1>.
- Liang, X., and L. Yu, 2016: Variations of the global net air–sea heat flux during the “hiatus” period (2001–10). *J. Climate*, **29**, 3647–3660, <https://doi.org/10.1175/JCLI-D-15-0626.1>.
- Lien, R.-C., D. R. Caldwell, M. Gregg, and J. N. Moum, 1995: Turbulence variability at the equator in the central Pacific at the beginning of the 1991–1993 El Niño. *J. Geophys. Res.*, **100**, 6881–6898, <https://doi.org/10.1029/94JC03312>.
- , M. J. McPhaden, and M. C. Gregg, 1996: High-frequency internal waves at 0°, 140°W and their possible relationship to deep-cycle turbulence. *J. Phys. Oceanogr.*, **26**, 581–600, [https://doi.org/10.1175/1520-0485\(1996\)026<0581:HFIWAA>2.0.CO;2](https://doi.org/10.1175/1520-0485(1996)026<0581:HFIWAA>2.0.CO;2).
- , E. A. D’Asaro, and C. E. Menkes, 2008: Modulation of equatorial turbulence by tropical instability waves. *Geophys. Res. Lett.*, **35**, L24607, <https://doi.org/10.1029/2008GL035860>.
- Liu, C., L. Fang, A. Köhl, Z. Liu, W. D. Smyth, and F. Wang, 2019a: The subsurface mode tropical instability waves in the equatorial Pacific Ocean and their impacts on shear and mixing. *Geophys. Res. Lett.*, **46**, 12270–12278, <https://doi.org/10.1029/2019GL085123>.
- , X. Wang, A. Köhl, F. Wang, and Z. Liu, 2019b: The northeast-southwest oscillating equatorial mode of the tropical instability wave and its impact on equatorial mixing. *Geophys. Res. Lett.*, **46**, 218–225, <https://doi.org/10.1029/2018GL080226>.
- , —, Z. Liu, A. Köhl, W. D. Smyth, and F. Wang, 2020: On the formation of a subsurface weakly sheared laminar layer and an upper thermocline strongly sheared turbulent layer in the eastern equatorial Pacific: Interplays of multiple-time-scale equatorial waves. *J. Phys. Oceanogr.*, **50**, 2907–2930, <https://doi.org/10.1175/JPO-D-19-0245.1>.
- Marchesiello, P., X. Capet, C. Menkes, and S. C. Kennan, 2011: Submesoscale dynamics in tropical instability waves. *Ocean Modell.*, **39**, 31–46, <https://doi.org/10.1016/j.ocemod.2011.04.011>.
- Marshall, J., A. Adcroft, C. Hill, L. Perelman, and C. Heisey, 1997: A finite-volume, incompressible Navier Stokes model for studies of the ocean on parallel computers. *J. Geophys. Res.*, **102**, 5753–5766, <https://doi.org/10.1029/96JC02775>.
- Masich, J., W. S. Kessler, M. F. Cronin, and K. R. Grissom, 2021: Diurnal cycles of near-surface currents across the tropical Pacific. *J. Geophys. Res. Oceans*, **126**, e2020JC016982, <https://doi.org/10.1029/2020JC016982>.
- McPhaden, M. J., and Coauthors, 2010: The Global Tropical Moored Buoy Array. *Proc. OceanObs*, **9**, 668–682, <https://doi.org/10.5270/OceanObs09.cwp.61>.
- Meehl, G., P. Gent, J. Arblaster, B. Otto-Bliesner, E. Brady, and A. Craig, 2001: Factors that affect the amplitude of El Niño in global coupled climate models. *Climate Dyn.*, **17**, 515–526, <https://doi.org/10.1007/PL00007929>.
- Miles, J. W., 1961: On the stability of heterogeneous shear flows. *J. Fluid Mech.*, **10**, 496–508, <https://doi.org/10.1017/S0022112061000305>.
- Moum, J. N., and D. Caldwell, 1985: Local influences on shear-flow turbulence in the equatorial ocean. *Science*, **230**, 315–316, <https://doi.org/10.1126/science.230.4723.315>.
- , D. R. Caldwell, and C. A. Paulson, 1989: Mixing in the equatorial surface layer and thermocline. *J. Geophys. Res.*, **94**, 2005–2022, <https://doi.org/10.1029/JC094iC02p02005>.
- , R.-C. Lien, A. Perlin, J. Nash, M. Gregg, and P. Wiles, 2009: Sea surface cooling at the equator by subsurface mixing in tropical instability waves. *Nat. Geosci.*, **2**, 761–765, <https://doi.org/10.1038/ngeo657>.
- , J. Nash, and W. Smyth, 2011: Narrowband oscillations in the upper equatorial ocean. Part I: Interpretation as shear instabilities. *J. Phys. Oceanogr.*, **41**, 397–411, <https://doi.org/10.1175/2010JPO4450.1>.
- , A. Perlin, J. D. Nash, and M. J. McPhaden, 2013: Seasonal sea surface cooling in the equatorial Pacific cold tongue controlled by ocean mixing. *Nature*, **500**, 64–67, <https://doi.org/10.1038/nature12363>.
- Newsom, E. R., and A. F. Thompson, 2018: Reassessing the role of the Indo-Pacific in the ocean’s global overturning circulation. *Geophys. Res. Lett.*, **45**, 12–422, <https://doi.org/10.1029/2018GL080350>.
- Osborn, T., 1980: Estimates of the local rate of vertical diffusion from dissipation measurements. *J. Phys. Oceanogr.*, **10**, 83–89, [https://doi.org/10.1175/1520-0485\(1980\)010<0083:EOTLRO>2.0.CO;2](https://doi.org/10.1175/1520-0485(1980)010<0083:EOTLRO>2.0.CO;2).
- Pacanowski, R., and S. Philander, 1981: Parameterization of vertical mixing in numerical models of tropical oceans. *J. Phys. Oceanogr.*, **11**, 1443–1451, [https://doi.org/10.1175/1520-0485\(1981\)011<1443:POVMIN>2.0.CO;2](https://doi.org/10.1175/1520-0485(1981)011<1443:POVMIN>2.0.CO;2).
- Paulson, C. A., and J. J. Simpson, 1977: Irradiance measurements in the upper ocean. *J. Phys. Oceanogr.*, **7**, 952–956, [https://doi.org/10.1175/1520-0485\(1977\)007<0952:IMITUO>2.0.CO;2](https://doi.org/10.1175/1520-0485(1977)007<0952:IMITUO>2.0.CO;2).
- Pei, S., T. Shinoda, W. Wang, and R.-C. Lien, 2020: Simulation of deep cycle turbulence by a global ocean general circulation model. *Geophys. Res. Lett.*, **47**, e2020GL088384, <https://doi.org/10.1029/2020GL088384>.
- Peters, H., M. Gregg, and J. Toole, 1988: On the parameterization of equatorial turbulence. *J. Geophys. Res.*, **93**, 1199–1218, <https://doi.org/10.1029/JC093iC02p01199>.
- , M. C. Gregg, and T. B. Sanford, 1994: The diurnal cycle of the upper equatorial ocean: Turbulence, fine-scale shear, and mean shear. *J. Geophys. Res.*, **99**, 7707–7723, <https://doi.org/10.1029/93JC03506>.
- Pham, H. T., S. Sarkar, and K. B. Winters, 2013: Large-eddy simulation of deep-cycle turbulence in an equatorial undercurrent model. *J. Phys. Oceanogr.*, **43**, 2490–2502, <https://doi.org/10.1175/JPO-D-13-016.1>.
- , W. D. Smyth, S. Sarkar, and J. N. Moum, 2017: Seasonality of deep cycle turbulence in the eastern equatorial Pacific. *J. Phys. Oceanogr.*, **47**, 2189–2209, <https://doi.org/10.1175/JPO-D-17-0008.1>.
- Pollard, R. T., and R. C. Millard, 1970: Comparison between observed and simulated wind-generated inertial oscillations. *Deep-Sea Res.*, **17**, 813–821, [https://doi.org/10.1016/0011-7471\(70\)90043-4](https://doi.org/10.1016/0011-7471(70)90043-4).
- , P. B. Rhines, and R. Thompson, 1972: The deepening of the wind-mixed layer. *Geophys. Astrophys. Fluid Dyn.*, **4**, 381–404, <https://doi.org/10.1080/03091927208236105>.
- Qiao, L., and R. H. Weisberg, 1997: The zonal momentum balance of the equatorial undercurrent in the central Pacific. *J. Phys. Oceanogr.*, **27**, 1094–1119, [https://doi.org/10.1175/1520-0485\(1997\)027<1094:TZMBOT>2.0.CO;2](https://doi.org/10.1175/1520-0485(1997)027<1094:TZMBOT>2.0.CO;2).

- Ray, S., A. T. Wittenberg, S. M. Griffies, and F. Zeng, 2018: Understanding the equatorial Pacific cold tongue time-mean heat budget. Part I: Diagnostic framework. *J. Climate*, **31**, 9965–9985, <https://doi.org/10.1175/JCLI-D-18-0152.1>.
- Richards, K. J., S.-P. Xie, and T. Miyama, 2009: Vertical mixing in the ocean and its impact on the coupled ocean–atmosphere system in the eastern tropical Pacific. *J. Climate*, **22**, 3703–3719, <https://doi.org/10.1175/2009JCLI2702.1>.
- Rohr, J., E. Itsweire, K. Helland, and C. Van Atta, 1988: Growth and decay of turbulence in a stably stratified shear flow. *J. Fluid Mech.*, **195**, 77–111, <https://doi.org/10.1017/S0022112088002332>.
- Sarkar, S., and H. T. Pham, 2019: Turbulence and thermal structure in the upper ocean: Turbulence-resolving simulations. *Flow Turbul. Combust.*, **103**, 985–1009, <https://doi.org/10.1007/s10494-019-00065-5>.
- Schudlich, R. R., and J. F. Price, 1992: Diurnal cycles of current, temperature, and turbulent dissipation in a model of the equatorial upper ocean. *J. Geophys. Res.*, **97**, 5409–5422, <https://doi.org/10.1029/91JC01918>.
- Shchepetkin, A. F., and J. C. McWilliams, 2005: The Regional Ocean Modeling System (ROMS): A split-explicit, free-surface, topography-following coordinate oceanic model. *Ocean Modell.*, **9**, 347–404, <https://doi.org/10.1016/j.ocemod.2004.08.002>.
- Shcherbina, A. Y., E. A. D’Asaro, and R. R. Harcourt, 2019: Rain and sun create slippery layers in eastern Pacific fresh pool. *Oceanography*, **32**, 98–107, <https://doi.org/10.5670/oceanog.2019.217>.
- Skyllingstad, E. D., and D. W. Denbo, 1994: The role of internal gravity waves in the equatorial current system. *J. Phys. Oceanogr.*, **24**, 2093–2110, [https://doi.org/10.1175/1520-0485\(1994\)024<2093:TROIGW>2.0.CO;2](https://doi.org/10.1175/1520-0485(1994)024<2093:TROIGW>2.0.CO;2).
- Small, R. J., and Coauthors, 2014: A new synoptic scale resolving global climate simulation using the Community Earth System Model. *J. Adv. Model. Earth Syst.*, **6**, 1065–1094, <https://doi.org/10.1002/2014MS000363>.
- , E. Curchitser, K. Hedstrom, B. Kauffman, and W. G. Large, 2015: The Benguela upwelling system: Quantifying the sensitivity to resolution and coastal wind representation in a global climate model. *J. Climate*, **28**, 9409–9432, <https://doi.org/10.1175/JCLI-D-15-0192.1>.
- Smyth, W. D., 2020: Marginal instability and the efficiency of ocean mixing. *J. Phys. Oceanogr.*, **50**, 2141–2150, <https://doi.org/10.1175/JPO-D-20-0083.1>.
- , and J. Moum, 2013: Marginal instability and deep cycle turbulence in the eastern equatorial Pacific Ocean. *Geophys. Res. Lett.*, **40**, 6181–6185, <https://doi.org/10.1002/2013GL058403>.
- , E. D. Skillingstad, G. B. Crawford, and H. Wijesekera, 2002: Nonlocal fluxes and Stokes drift effects in the k-profile parameterization. *Ocean Dyn.*, **52**, 104–115, <https://doi.org/10.1007/s10236-002-0012-9>.
- , J. Moum, and J. Nash, 2011: Narrowband oscillations in the upper equatorial ocean. Part II: Properties of shear instabilities. *J. Phys. Oceanogr.*, **41**, 412–428, <https://doi.org/10.1175/2010JPO4451.1>.
- , —, L. Li, and S. Thorpe, 2013: Diurnal shear instability, the descent of the surface shear layer, and the deep cycle of equatorial turbulence. *J. Phys. Oceanogr.*, **43**, 2432–2455, <https://doi.org/10.1175/JPO-D-13-089.1>.
- , H. Pham, J. Moum, and S. Sarkar, 2017: Pulsating turbulence in a marginally unstable stratified shear flow. *J. Fluid Mech.*, **822**, 327–341, <https://doi.org/10.1017/jfm.2017.283>.
- , S. Warner, J. Moum, H. Pham, and S. Sarkar, 2021: What controls the deep cycle? Proxies for equatorial turbulence. *J. Phys. Oceanogr.*, **51**, 2291–2302, <https://doi.org/10.1175/JPO-D-20-0236.1>.
- Tanaka, Y., T. Hibiya, and H. Sasaki, 2015: Downward lee wave radiation from tropical instability waves in the central equatorial Pacific Ocean: A possible energy pathway to turbulent mixing. *J. Geophys. Res. Oceans*, **120**, 7137–7149, <https://doi.org/10.1002/2015JC011017>.
- Taylor, J. R., 2008: Numerical simulations of the stratified oceanic bottom boundary layer. Ph.D. dissertation, University of California, San Diego, 230 pp.
- Thorpe, S., and Z. Liu, 2009: Marginal instability? *J. Phys. Oceanogr.*, **39**, 2373–2381, <https://doi.org/10.1175/2009JPO4153.1>.
- Trenberth, K. E., and J. T. Fasullo, 2018: Applications of an updated atmospheric energetics formulation. *J. Climate*, **31**, 6263–6279, <https://doi.org/10.1175/JCLI-D-17-0838.1>.
- Tsujino, H., and Coauthors, 2018: JRA-55 based surface dataset for driving ocean–sea-ice models (JRA55-do). *Ocean Modell.*, **130**, 79–139, <https://doi.org/10.1016/j.ocemod.2018.07.002>.
- Venayagamoorthy, S. K., and J. R. Koseff, 2016: On the flux Richardson number in stably stratified turbulence. *J. Fluid Mech.*, **798**, R1, <https://doi.org/10.1017/jfm.2016.340>.
- Wang, D., and P. Müller, 2002: Effects of equatorial undercurrent shear on upper-ocean mixing and internal waves. *J. Phys. Oceanogr.*, **32**, 1041–1057, [https://doi.org/10.1175/1520-0485\(2002\)032<1041:EOEUSO>2.0.CO;2](https://doi.org/10.1175/1520-0485(2002)032<1041:EOEUSO>2.0.CO;2).
- , W. G. Large, and J. C. McWilliams, 1996: Large-eddy simulation of the equatorial ocean boundary layer: Diurnal cycling, eddy viscosity, and horizontal rotation. *J. Geophys. Res.*, **101**, 3649–3662, <https://doi.org/10.1029/95JC03441>.
- , J. C. McWilliams, and W. G. Large, 1998: Large-eddy simulation of the diurnal cycle of deep equatorial turbulence. *J. Phys. Oceanogr.*, **28**, 129–148, [https://doi.org/10.1175/1520-0485\(1998\)028<0129:LESOTD>2.0.CO;2](https://doi.org/10.1175/1520-0485(1998)028<0129:LESOTD>2.0.CO;2).
- Wang, W., and M. J. McPhaden, 1999: The surface-layer heat balance in the equatorial Pacific Ocean. Part I: Mean seasonal cycle. *J. Phys. Oceanogr.*, **29**, 1812–1831, [https://doi.org/10.1175/1520-0485\(1999\)029<1812:TSLHBI>2.0.CO;2](https://doi.org/10.1175/1520-0485(1999)029<1812:TSLHBI>2.0.CO;2).
- Warner, S. J., and J. N. Moum, 2019: Feedback of mixing to ENSO phase change. *Geophys. Res. Lett.*, **46**, 13 920–13 927, <https://doi.org/10.1029/2019GL085415>.
- Watkins, C., and D. B. Whitt, 2020: Large-aspect-ratio structures in simulated ocean surface boundary layer turbulence under a hurricane. *J. Phys. Oceanogr.*, **50**, 3561–3584, <https://doi.org/10.1175/JPO-D-20-0134.1>.
- Whitt, D. B., and J. R. Taylor, 2017: Energetic submesoscales maintain strong mixed layer stratification during an autumn storm. *J. Phys. Oceanogr.*, **47**, 2419–2427, <https://doi.org/10.1175/JPO-D-17-0130.1>.
- , S. Nicholson, and M. Carranza, 2019: Global impacts of sub-seasonal (<60 day) wind variability on ocean surface stress, buoyancy flux, and mixed layer depth. *J. Geophys. Res. Oceans*, **124**, 8798–8831, <https://doi.org/10.1029/2019JC015166>.
- Zaron, E. D., and J. N. Moum, 2009: A new look at Richardson number mixing schemes for equatorial ocean modeling. *J. Phys. Oceanogr.*, **39**, 2652–2664, <https://doi.org/10.1175/2009JPO4133.1>.
- Zhu, Y., and R.-H. Zhang, 2019: A modified vertical mixing parameterization for its improved ocean and coupled simulations in the tropical Pacific. *J. Phys. Oceanogr.*, **49**, 21–37, <https://doi.org/10.1175/JPO-D-18-0100.1>.